INSTITUTO TECNOLÓGICO Y DE ESTUDIOS SUPERIORES DE MONTERREY

CAMPUS MONTERREY

DIVISIÓN DE INGENIERÍA Y ARQUITECTURA

PROGRAMA DE GRADUADOS EN INGENIERÍA

"STUDIES ON CIS THIN FILMS DEPOSITED BY R. F. SPUTTERING AND CdS NANOPARTICLES DEPOSITED BY MICROWAVE ASSISTED CBD FOR PHOTOVOLTAIC APLICATIONS"

TESIS

PRESENTADA COMO REQUISITO PARCIAL PARA OBTENER EL GRADO ACADÉMICO DE:

DOCTORADO EN CIENCIAS DE INGENIERÍA

POR:

RODRIGO CUÉ SAMPEDRO SOBERANIS

MONTERREY, N. L., MÉXICO **DICIEMBRE 2009**

Este trabajo de tesis está dedicado a la memoria del

Dr. Hugo Alejo Velasco Molina

Mentor y amigo entrañable

…Yo lo miro desde lejos,
pero somos tan distintos;
es que creció con el siglo
con tranvía y vino tinto…

Viejo, mi querido viejo

AGRADECIMIENTOS

Quiero reiterar mi eterno agradecimiento al apoyo que me dio en vida el Dr. Hugo Alejo Velasco Molina (q.e.p.d.) y mi eterna gratitud a su familia, en especial a la Sra. María Elena Aguirre Vda. de Velasco por todo el cariño y apoyo que durante años he seguido recibiendo y que me ha servido para alcanzar las metas más importantes de mi vida.

Mi reconocimiento y sentido de gratitud está dedicado al Dr. Velumani Subramaniam, por su hábil dirección, paciencia, valiosas sugerencias y el estímulo constante a lo largo de mi investigación.

Estoy muy agradecido con el Dr. Carlos Iván Rivera Solorio por su apoyo y sugerencias en la consolidación y estructuración de mis resultados.

Es con gran satisfacción que aprovecho esta oportunidad para dejar constancia de mi sincero agradecimiento a la Sra. Alicia Garza la Güera de Navarro, quien a lo largo de mis estudios siempre me brindó su amistad y apoyo incondicional.

También quiero agradecer al Dr. Bernard Micheli Masson por su apoyo y consejos en los momentos más difíciles durante mis estudios, al Dr. Federico Viramontes Brown por su constante motivación y acertadas recomendaciones y a la Dra. Oxana Vasilievna Kharissova por sus observaciones y consejos.

Quiero agradecer al Dr. Mario Manzano Camarillo por darme la mano en los momentos difíciles y al Dr. Armando Llamas Terrés su firme apoyo para culminar mis estudios.

Mi personal agradecimiento a los directores Dr. Pathiyamattom Joseph Sebastian, del CIE-UNAM, Temixco, al Dr. José Chávez Carvayar del IIM-UNAM, D. F., al Dr. Victor Sanchez Reséndiz del SEES-CINVESTAV, D. F. y al Dr. Umapada Pal del IFUAP, Puebla por su oportuna ayuda y sus esfuerzos para la caracterización y obtención de los resultados de las muestras analizadas.

Mi sincero agradecimiento a los investigadores Dr. Arturo Morales Acevedo, Dr. Ramón Peña Sierra, Dr. Alejandro Ávila García, Dr. Iouri Alekseevich Koudriavtsev, Dr. Yasuhiro Matsumoto Kuwawara y Dra. Magali Estrada del Cueto, del Departamento de Ingeniería Eléctrica del SEES CINVESTAV-IPN, por proporcionarme los servicios de laboratorio necesarios y el estímulo constante a lo largo del curso de mi investigación.

También quiero agradecer la excelente colaboración de varios miembros del Departamento de Ingeniería Eléctrica del SEES CINVESTAV-IPN en especial al M Sc. Miguel Galván Arellano, al Ing. Miguel Angel Avendaño, al Dr. Gaspar Casados Cruz y a la Ing. Georgina Ramírez Cruz por su excelente colaboración en las pruebas realizadas.

Quiero agradecer de forma muy especial a Enriqueta Aguilar Valencia del SEES CINVESTAV-IPN por brindarme su amistad y por apoyarme en las numerosas deposiciones de los contactos de aluminio para las pruebas eléctricas.

Mi más sincero agradecimiento al M Sc. Luis Ixtlilco Cortés y al Dr. Francisco Vallarta Rodríguez por su hospitalidad durante mis estancias en Temixco y el Distrito Federal, respectivamente.

No encuentro palabras para agradecerle a mi compañera de estudios Vidhya Bhojan por todo el apoyo que proporcionó durante el curso de mi trabajo.

Mi agradecimiento al M Sc. Ernesto Efrén Velázquez por dedicarle tiempo a la revisión y corrección de mi tesis para hacerla más elocuente.

Mi más profundo agradecimiento a la Sra. Myriam Paloma Martínez Robles por haber sido como parte de mi familia durante mi preparación académica.

Quiero expresar mi agradecimiento al Dr. Alberto Bustani Adem, rector del ITESM Campus Monterrey por la beca de sostenimiento que recibí durante mis estudios doctorales.

De igual forma le agradezco al Dr. Hugo Terashima Marín por otorgarme una beca de excelencia y el apoyo económico para la titulación.

Agradezco al proyecto “Agua y Vida”, a la cátedra de Nanoelectrónica, al Centro de Estudios de Energía y al Departamento de Becas del ITESM campus Monterrey por el apoyo económico brindado.

Y por último y no menos importante le agradezco a Dios porque a pesar de los muchos y muy difíciles obstáculos que se me presentaron a lo largo de mi investigación y estudios, siempre surgió una solución para poder continuar y concluir mi doctorado.

RESUMEN

La conversión de energía por medio de dispositivos fotovoltaicos es una alternativa viable para reducir las emisiones que contribuyen al calentamiento global. En la actualidad el silicio representa el principal material empleado en las celdas fotovoltaicas, el cual debe tener una pureza muy elevada y una estructura cristalina casi perfecta. Esto representa procesos muy caros que elevan el costo del producto y hace que la conversión de energía lumínica no sea una opción competitiva en comparación con la generación de energía por medio de combustibles fósiles. Las celdas fotovoltaicas de película delgada permiten reducir los costos de producción y adicionalmente crear celdas con un mínimo de material, reduciendo significativamente su costo. Materiales alternos al silicio como el cobre indio di-selenio (CIS) y el sulfuro de cadmio (CdS) prometen altas eficiencias combinadas con precios más bajos.

El objetivo del presente trabajo de tesis es establecer las mejores condiciones de deposición para optimizar las propiedades de cada elemento que conforma una celda fotovoltaica completa.

Una celda fotovoltaica se divide en cuatro capas principales: Contacto posterior (molibdeno) depositado por pulverización catódica en corriente directa, capa de absorción (CIS) depositada por pulverización catódica en radio frecuencia, capa ventana (CdS) depositado por baño químico asistido por microondas y contacto transparente superior (óxido de indio estaño) depositado por pulverización catódica en radio frecuencia.

Optimización de las propiedades estructurales, ópticas y eléctricas de la capa de absorción

El CIS es un compuesto ternario que pertenece a la familia I-III-VI_2 de los semiconductores. Se utiliza comúnmente como capa de absorción en sistemas fotovoltaicos en forma de película delgada policristalina. La técnica tradicional de deposición del CIS por pulverización catódica es empleando una fuente de corriente directa para depositar una película de CuIn y posteriormente hacer una selenización. En esta tesis se estudió la

deposición de CIS por medio de pulverización catódica a partir de un objetivo de CIS con 99.99% de pureza usando una fuente de radiofrecuencia.

Los efectos de la variación de los parámetros distancia sustrato-objetivo, potencia y espesor fueron analizados. Las películas de CIS fueron depositadas por pulverización catódica en RF a partir de un único objetivo ternario de $CuInSe_2$. Posteriormente se añadió una evaporación de cobre a las películas seguidas de recocido térmico adecuado para mejorar su cristalinidad y proporcionar adecuada estequiometría. El análisis estructural, de composición y morfología superficial se realizaron mediante difracción de rayos X (XRD), dispersión de energía de rayos X (EDAX) y análisis de microscopio electrónico de barrido (SEM), respectivamente. Se estudiaron las propiedades ópticas por medio de espectrofotometría usando longitudes de onda de 300 a 2500 nm. Las propiedades eléctricas se analizaron empleando la caracterización en conducción en corriente alterna (ac), corriente directa (I-V) y estudios de efecto Hall.

La primer deposición de películas delgadas de CIS se basó en las condiciones del método tradicional y los parámetros fueron: espesor de 2000 nm, potencia de 80 W y se analizó el efecto de la distancia sustrato-objetivo de 4.0 a 6.5 cm. El análisis de composición mostró que las películas eran deficientes en cobre, por lo que se incorporó un proceso post-depósito que consistía en evaporar cobre por 13 segundos a una razón de crecimiento de 35Å/s y un tratamiento térmico a 500°C por 15 minutos. Posteriormente el análisis estructural indicó que todas las películas poseían estructura calcopirita con planos correspondientes a (112), (004), (220) y (116). Se observó un cambio en la preferencia del plano de (004) a (112) para la distancia máxima de sustrato-objetivo de 6.5 cm. El análisis de composición mostró que variando la distancia de 4.0 a 6.5 cm, el parámetro Δm = (Cu/In-1) pasó de -0.74 a 0.21 indicando que la difusión del elemento cobre mejora con la distancia, de tal forma que la mejor distancia entre el sustrato y el blanco fue 6.5 cm.

El segundo grupo de películas se depositaron con un espesor de 2000nm, a una distancia sustrato-objetivo de 6.5 cm. y se varió la potencia de 40 a 110 W. La variación de potencia mostró un cambio muy significativo en las propiedades estructurales de las

películas, el tamaño de grano varió de 73 nm en la película depositada a 110 W hasta 287 nm en la película depositada a 40 W. Voltajes negativos fueron observados en el análisis del efecto hall en películas depositadas en potencias mayores a 90 W. El análisis óptico muestra que la película depositada a 80 W exhibía una brecha de energía directa que permite una absorción fotónica a partir de energías de 1.05 eV, el cual se considera adecuado para aplicaciones fotovoltaicas. El efecto Hall demostró que existe una relación entre la composición y el tipo de semiconductor. Se concluyó que el valor adecuado para la potencia era de 80 W.

El tercer grupo de películas se depositaron variando el espesor de 1000 a 3000 nm a 80 W y distancia sustrato-objetivo de 6.5 cm. Los resultados estructurales mostraron que la orientación cambia del plano (112) al plano (103) en espesores superiores a los 2000 nm. Los análisis eléctricos mostraron que la mejor conductividad se da en las películas con orientación al plano (112) de esta forma se concluyó que el espesor óptimo era de 2000 nm debido a su orientación estructural.

Optimización de las propiedades estructurales, ópticas y eléctricas de la capa ventana

El sulfuro de cadmio es un compuesto binario que pertenece a la familia II-VI de los semiconductores. Se emplea como capa ventana en las celdas fotovoltaicas policristalinas de película delgada. Películas delgadas de CdS policristalinas con brecha energía alrededor del 2.42 eV son hasta ahora la mejor capa ventana para heterouniones de CIS en celdas fotovoltaicas.

Se elaboraron películas delgadas de CdS por un método rápido de síntesis llamado baño químico asistido por microondas (MA-CDB). Los compuestos químicos empleados en la deposición fueron: nitrato de cadmio ($Cd(NO_3)_2$), citrato de sodio ($Na_3C_6H_5O_7$), Tiourea ($CS(NH_2)_2$) e hidróxido de amonio (NH_4OH). Para las soluciones que contenían elementos de dopaje, se agregaron a la solución los siguientes reactivos: para el dopaje de cloro, 0.1M de cloruro de amonio (NH_4Cl), para el dopaje de boro, 0.1M de ácido bórico (H_3BO_3), para el dopaje de sodio, 0.1M de cloruro sódico (NaCl).

Las películas delgadas de CdS se depositaron en sustratos de vidrio a 5 diferentes tiempos de depósito para generar 5 espesores distintos. Se adaptó a la unidad de microondas un control de la temperatura para mantener una temperatura constante de 70°C. El tiempo de irradiación de microondas fueron 60, 90, 120, 150 y 180 segundos con un tiempo de deposición total de 10, 15, 20, 25 y 30 minutos respectivamente. Los espesores de las películas depositadas se determinaron por un perfilómetro. La composición de las películas fue analizada utilizando EDAX. Se ha observado que la composición de las partículas de CdS fue prácticamente estequiométrica (42.17% atómico de azufre y 57.83% atómico de cadmio). Se determinaron las transmitancias ópticas de las películas por medio de un espectrofotómetro en un rango de longitudes de onda de 300 a 2500 nm. Los espectros de transmisión revelan un porcentaje relativamente alto de transmisión (80%) en las películas depositadas. La brecha de energía aumenta al aumentar el espesor. Se observaron brechas de energía de 2.46 eV a 2.54 eV. Las caracterizaciones eléctricas muestran que la conductividad aumenta de 270 a 4900S con el aumento en el espesor de 100 a 300 nm. Fotoluminiscencia, espectroscopía Raman y espectroscopía de masas de iones secundarios (SIMS) se emplearon para analizar las propiedades ópticas, estructurales y de composición respectivamente, de las películas de CdS al ser dopadas con Cloro, sodio y Boro. El análisis de fotoluminiscencia demostró que el cloro ha sido el elemento que más influye en el comportamiento del borde de banda. Los espectros de Raman de la película de CdS dopada con boro presentó una bien definida línea aproximadamente a 300 cm^{-1}, que indican que este elemento fue absorbido en la estructura del CdS. SIMS mostró que la película de CdS dopada con boro tiene una mayor uniformidad a lo largo del espesor.

Optimización de las propiedades estructurales, ópticas y eléctricas del contacto superior transparente

Oxido de indio estaño (ITO) usado como contacto superior transparente fue depositado por medio de pulverización catódica en radio frecuencia. La temperatura del sustrato, potencia y espesor fueron optimizados considerando las propiedades ópticas y eléctricas del ITO. El espesor de las películas depositadas de ITO que mostró mejor transmitancia y conductividad fue de 100 nm despositado a una temperatura de sustrato de

100°C y a una potencia de 80W. La película presentaba una valor de transmitancia de 93% y una resistividad de $2.1x10^{-4}$ Ω.

Optimización de las propiedades estructurales y eléctricas del contacto posterior

Las películas de molibdeno (Mo) empleadas como contacto posterior fueron depositadas por pulverización catódica en corriente directa. Se optimizaron las condiciones de deposición en base a las propiedades eléctricas. Las películas delgadas de Mo fueron depositadas sobre sustratos de vidrio variando el espesor de 400 a 1000 nm, la potencia de 20 a 40W y la temperatura de sustrato de temperatura ambiente a 500°C. La menor resistencia eléctrica se encontró en el espesor de 1000 nm con un valor de $6x10^{-4}$ Ω. Se observó que la resistencia disminuía al aumentar la temperatura del sustrato.

ABSTRACT

The energy conversion via photovoltaic devices is a viable alternative for reducing emissions that contribute to global warming. At present, silicon is the main material used in photovoltaic cells, which must have a very high purity and an almost perfect crystal structure. This represents a very expensive process which increases the cost of the product and makes the conversion of light energy a not competitive option compared to energy generation through fossil fuels. Thin-film photovoltaic cells can reduce production costs and additional create cells with a minimum of material, reducing significantly its cost. Alternative materials to silicon such as copper indium di-selenide (CIS) and cadmium sulfide (CdS) promise high efficiencies, combined with lower prices.

Present thesis work focuses on the deposition optimization of CIS, CdS, top and back contacts used in the fabrication of thin film photovoltaic devices.

PV cell consists of four main layers: Contact later (molybdenum) deposited by direct current sputtering, absorber layer (CIS) deposited by radio frequency sputtering, window layer (CdS) deposited by microwave-assisted chemical bath and transparent top contact (indium tin oxide) deposited by radio frequency sputtering.

Optimization of structural, electrical and optical properties of the absorption layer

CIS is a ternary compound that belongs to the I-III-VI_2 family of semiconductors. It is commonly used as absorber layer in photovoltaic systems in the form of polycrystalline thin film. The traditional technique of the CIS deposition by sputtering is using a source of direct current to deposit a CuIn film and subsequently selenization. In this thesis we studied the CIS deposition by sputtering from a target of CIS with 99.99% purity using a radio frequency source.

The effects of substrate to target distance, power and thickness were analyzed. CIS thin films were deposited by one-step sputtering from a single ternary target of $CuInSe_2$.

Since the films were found to be deficit in copper, subsequently Copper granules has been evaporated on to the films and followed by thermal annealing to improve the crystallinity and provide adequate stoichiometry. Structural, composition and surface analysis were performed using X-ray diffraction, energy dispersive X-ray analysis and scanning electron microscope respectively. Optical properties were studied by spectrophotometer over the wavelength range of 300-2500 nm. Electrical parameters were evaluated by ac conduction, I-V characterization and Hall effect studies.

The first set of CIS films were deposited based on traditional method and the parameters were: thickness of 2000 nm, 80W power and distance substrate target varied from 4.0 to 6.5 cm. Composition analysis showed that the films were deficit in elemental copper and therefore, in order to attain the stochiometry, an additional copper evaporation of 13 seconds at a rate of 35 Å/s and annealing of 15 minutes at 500°C were performed. Structural analysis indicates that all the films possess chalcopyrite structure with the peak values corresponding to (112), (004), (220) and (116). Shift in preferred orientation from (004) to (112) has been observed for the maximum substrate to target distance of 6.5 cm. From composition analysis it was found that by varying the distance from 4.0 to 6.5 cm, the parameter Δm = (Cu/In-1) has shifted from -0.74 to 0.21 indicating that diffusion of elemental copper improves with distance, thus it was found that the optimum distance between target and substrate was 6.5 cm.

The second set of CIS thin films were deposited with a thickness of 2000 nm, substrate to target distance of 6.5 cm and power variation from 40 to 110 W. Change in power produces significant changes in structural properties of the films. Grain size varied from 73nm in a film deposited at 100W to 287 nm in a film deposited at 40W. Negative Hall voltage has been observed for films deposited above 90 W. Optical analysis shows that the film deposited at 80W exhibited a direct allowed transition with an average band gap value of 1.05 eV, which is considered appropriate to improve the conversion efficiency. Hall effect showed that there is a relationship between the composition and type of semiconductor. It was concluded that the appropriate value for the power was 80 W.

The third set of films were deposited with five different thicknesses from 1000 to 3000 nm at 80W and 6.5 cm substrate-target distance. Structural results showed that orientation changes from the plane (112) to plane (103) in thicknesses greater than 2000 nm. Electrical analysis showed that the best conductivity is in the orientation to the plane (112) and Optimum thickness was found to be 2000 nm due to the preferred oriented structure.

Optimization of structural, electrical and optical properties of the window layer

Cadmium sulfide is a binary compound that belongs to the II-VI family of semiconductors. It is used as window layers in polycrystalline thin-film photovoltaic cells. CdS polycrystalline thin films with an energy band gap around 2.42 eV are now a day the best window layers for the CIS heterojunction photovoltaic cells.

CdS thin films have been prepared by a rapid of microwave-assisted chemical bath deposition technique (MA-CBD) due to the ability of this technique to achieve homogeneous polycrystalline films in a few minutes instead of hours as it is in the conventional CBD. Chemical solution used for the deposition comprised of Cadmium Nitrate ($Cd(NO_3)_2$), Sodium Citrate ($Na_3C_6H_5O_7$), Thiourea ($CS(NH_2)_2$) and Ammonium Hydroxide (NH_4OH). CdS thin films were deposited onto well-cleaned glass substrates for 5 different deposition times, thus varying the thicknesses of the deposited films. A temperature control is incorporated to the microwave unit to keep a constant temperature of 70°C. The total microwave irradiation times were 60, 90, 120, 150 and 180 seconds during deposition time of 10, 15, 20, 25 and 30 minutes respectively. Thicknesses of the deposited films were determined by a profile-meter. Composition of the films was analyzed using EDAX. It has been observed that the composition of CdS particles was Sulfur 42.17 atomic % and cadmium 57.83 atomic%. The sulfur deficit is expected due to CdS is non-stoichiometric semiconductor and this lack in sulfur allows n type conductivity. Both the cubic sphalerite (Hawleyite) and the hexagonal wurtzite (Greenockite) phases were observed by XRD analysis. Structural parameters such as lattice constants, crystallite size, dislocation density and strain have been evaluated. Optical transmittances of the films have

been determined by spectrophotometer over wavelength range of 300-2500 nm. Transmission spectra reveal a relatively high transmission (80%) in the deposited films. Optical band gap increases with the increase in thickness. A direct band gap ranging from 2.46 eV to 2.54 eV was deduced.

It was found that the electrical properties of CdS thin film can be extremely improve by doping, developing the recombination activity at the grain boundaries. Doping sources were added to the reactants to introduce elements to the films of chlorine, boron and sodium. The doping sources and concentrations added to the reactants were: for chlorine doping, 0.1M ammonium chloride (NH_4Cl), for boron doping, 0.1M boric acid(H_3BO_3), for sodium doping, 0.1M sodium chloride (NaCl). Photoluminescence (PL), Raman spectroscopy and secondary ion mass spectroscopy (SIMS) analysis were performed to examine the optical, structural and composition respectively, of CdS films doped with chlorine, sodium and boron. PL analysis showed that chlorine has been the element that most influences the behavior of band edge. CdS films doped with chlorine presented a shift to the blue edge, indicating an opening of the absorption edge. Raman spectra of the boron doped CdS film present a well-resolved line at approximately 300 cm^{-1}, which indicate that boron element has been absorbed into the CdS structure. SIMS showed the uniform incorporation of boron throughout the entire thickness of the deposited film. Electrical characterization shows that the conductivity increases from 270 to 4900S with the boron incorporation.

Optimization of structural, electrical and optical properties of the top contact layer

Indium tin oxide used as front contact for PV devices were deposited by r.f. sputtering technique. Substrate temperature, power and thickness were optimized considering the optical and electrical properties of ITO. The best ITO layer thickness of the deposited films was in the range of 100 nm deposited at 100°C substrate temperature and power of 80W. This film obtained a maximum transmittance value of 93% and a resistivity of $2.1x10^{-4}$ Ω.

Optimization of structural and electrical properties of the back contact layer

Molybdenum films used as back contact layer were deposited by d.c. sputtering technique. The deposition conditions were optimized based on electrical properties. Mo thin films were deposited on glass substrates using DC sputtering varying the thickness from 400 to 1000 nm, power from 20 to 40 W and substrate temperature from room temperature to 500°C. The minimum resistance was found in 1000 nm thickness with a value of $6x10^{-4}$ Ω. It was observed that the resistance decreases with increasing substrate temperature.

CONTENTS

CHAPTER I Introduction

1.1 INTRODUCTION

According to the Intergovernmental Panel on Climate Change (IPCC), Topic 1, there is a world emergency due to the harmful effects of the global warming over natural and human systems. Warming of the climate system is unequivocal, as is now evident from observations of increases in global average and ocean temperatures, widespread melting of snow and ice and rising global average sea level as can be seen in figure 1.1 [1].

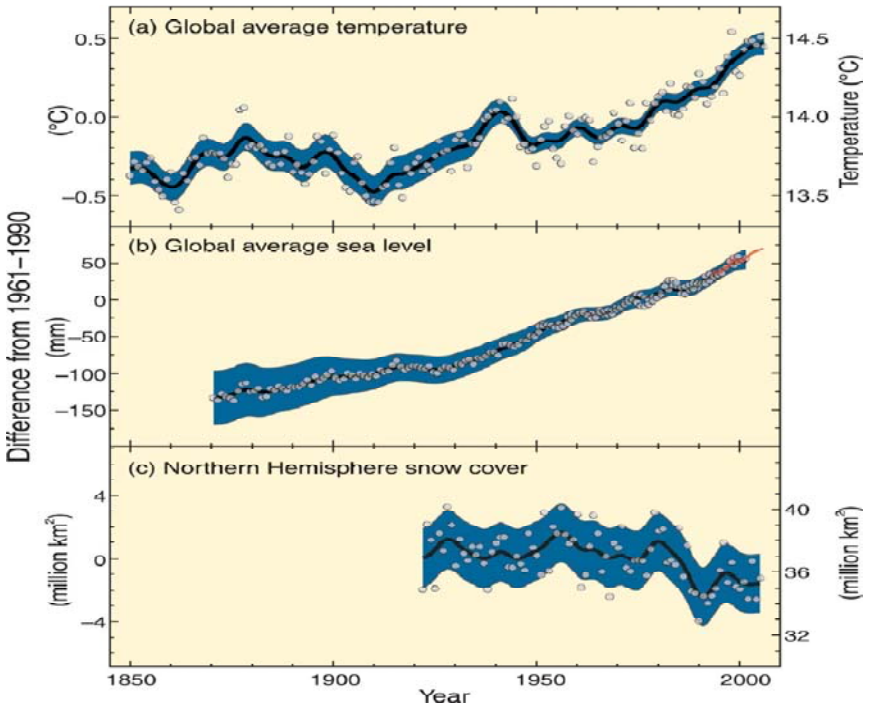

Figure 1.1 Observed changes in (a) global average temperature; (b) global average sea level from tide gauge (blue) and satellite (red) data; and (c) Northern Hemisphere snow cover for March-April.

The present ways of producing energy are mainly based on fossil fuels, essentially coal, oil and natural gas. Only a small amount of the total energy produced worldwide comes from renewable sources, which do not release greenhouse gases that ultimately trap

heat in to the atmosphere. Nonetheless, the interest in renewable energy production is increasing, as several renewable alternatives are being developed at present. The challenge shared by these advanced technologies is to attain a ratio of cost–competitiveness comparable to those of already established non-renewable energy sources.

The Sun emits electromagnetic radiation in a wide range of wavelengths, in which our interest being the most intense sections that reach the surface of the earth, like ultraviolet, visible and infrared of this spectrum. Solar irradiance is greatest at visible wavelengths, 300-800 nm, peaking in the blue-green. Thus the Sun is an abundant, always available free energy source, which can be collected by a solar energy converter. For this purpose there are two types of solar devices: Solar thermal and photovoltaic converters. To distinguish these different types of solar energy converters, we need to consider the different modes of energy transfer from the Sun. The radiant energy absorbed by a device can either increase the kinetic energy of the atoms and electrons in the absorbing material (internal energy), or it can increase the potential energy of the electrons. Which of these occurs depends upon the material and how it is connected to the outside world.

In a solar thermal converter, the radiant energy absorbed is converted mainly into internal energy and raises the temperature of the cell. The difference in temperature between the element and its surroundings allows the solar converter to operate as a heat engine, for instance by driving a steam turbine to generate electric power. Solar thermal converters utilise the full range of solar wavelengths, including the infrared, and are designed to heat up easily. These elements are thermally insulated from their surroundings to make the working temperature difference as large as possible. But, the photovoltaic converter extracts solar energy only from those photons with energy sufficient to bridge the band gap of a determined semiconductor material. It is designed to absorb a photon causing the promotion of an electron to a state of higher energy (an *excited state*). For the extra electronic energy to be extracted, the excited state should be separated from the ground state by an energy gap and then properly collected. Another advantage of photovoltaic devices is, it convert the Sun's energy directly to electricity. Over the last decades, this

technology has emerged to become an application of recognised potential and has attracted the interest of increasing numbers of researchers.

1.2 FOTOVOLTAIC CELLS

Semiconductor materials provide the building blocks for many of our current electronic devices. These materials have an easily controllable electrical conductivity, which allows their use in electronic devices such as transistors, diodes and photovoltaic cells. These materials are defined by their electrical and optical properties. From the electrical point of view, values of volume conductivity for a good conductor lie within the range of 10^4-10^6 ($S \cdot m^{-1}$), while for an insulator it is less than 10^{-10} ($S \cdot m^{-1}$). Accordingly, a semiconductor is a material whose conductivity lies between those of conductors and insulators (10^{-10} – 10^4 ($S \cdot m^{-1}$)) [2-5]. Semiconductors can behave either as conductors or as insulators depending on their temperature or the quality of doping. From an optical point of view, semiconductors can be defined as those materials which have band gap values less than 6 eV.

1.2.1 SEMICONDUCTING COMPOUNDS

Silicon and germanium are the only elements that have practical applications as semiconductors. However, a large number of ceramic and intermetallic compounds display the same effect. Examples are given in Table 1.1 [6, 7].

Table 1.1 Ceramic and intermetallic semiconductors.

Compound	Energy Gap (eV)	Electron Mobility (cm^2/V-s)	Hole Mobility (cm^2/V-s)
ZnS	3.54	180	5
GaP	2.24	300	100
GaAs	1.35	8,800	400
GaSb	0.67	4,000	1,400
InSb	0.165	78,000	750
InAs	0.36	33,000	460
ZnO	3.2	180	
CdS	2.42	400	
PbS	0.37	600	600
$CuInSe_2$	1.04	1,000	180

1.2.2 P-N JUNCTION DEVICE

The *P-N* junction is the classical model of a photovoltaic cell. This type of junction is created by joining an *N*-type semiconductor to a *P*-type semiconductor, forming a *P-N* junction as shown in the Fig. 1.2 [8]. Electrons are concentrated in the *N*-type, while holes are concentrated in the *P*-type. The resulting electrical imbalance creates a voltage or contact potential, across the junction.

In the dark: If an external voltage is placed on the *P-N* junction so that the negative terminal is at the *N*-type side, both the electrons and holes move toward the junction and eventually recombine. The movement of electrons and holes causes a net current to be produced. This is called forward bias, Fig. 1.3 a.

However, if the applied voltage is reversed, creating a reverse bias, both the holes and electrons move away from the junction. With no charge carriers in the depletion zone, the junction behaves as an insulator, and virtually no current flows, Fig. 1.3 b.

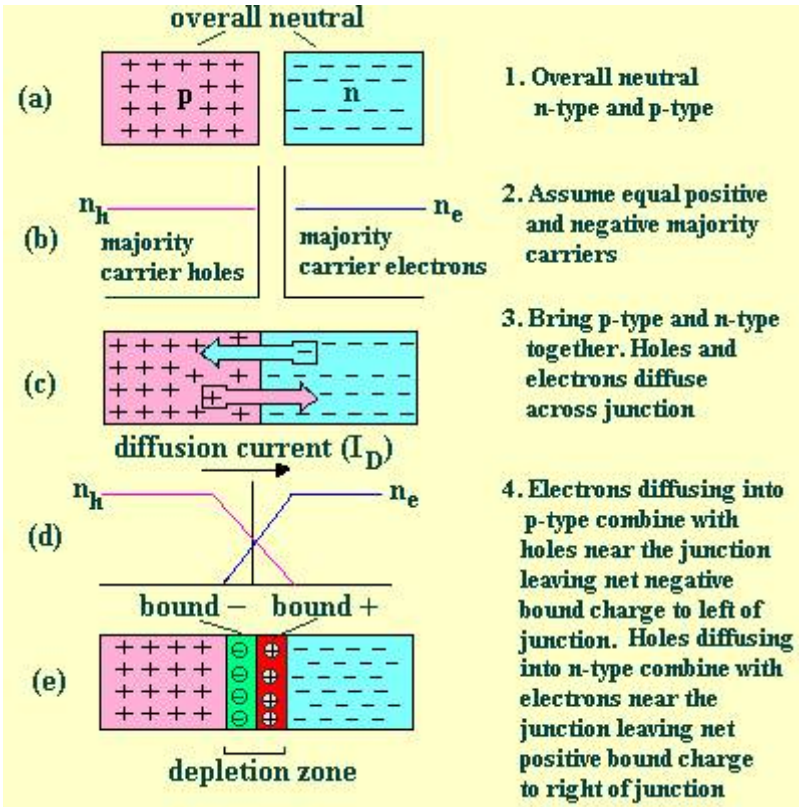

Figure 1.2 Electrical behavior of the p-n junction.

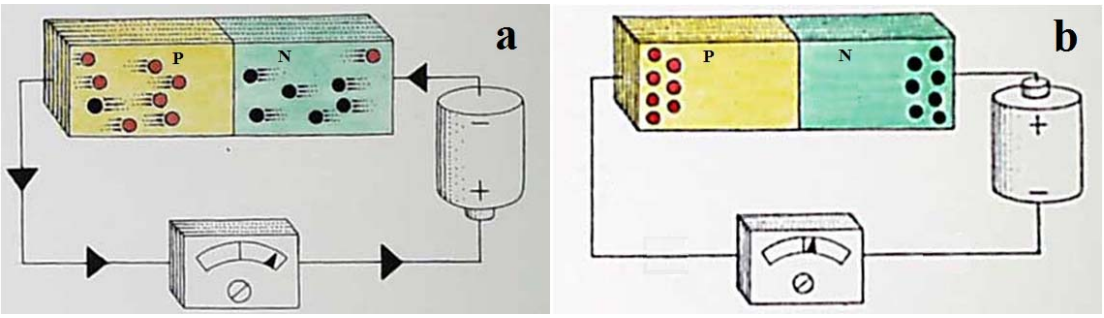

Figure 1.3 The movement of the electrons and holes at a) forward bias connection and b) reverse bias connection.

Because the *P*-*N* junction permits current to flow in only one direction, only half of an alternating current passes through it, therefore converting an alternating current into a direct current. When used in this kind of applications, junctions are called rectifier diodes.

When charged by the Sun: Since the work function of the *P*-type material is larger than that of the *N*-type, the electrostatic potential is different in both materials. Thus, an electric field is established at the junction, which drives photogenerated electrons towards the *N* side and holes towards the *P* side. The junction region is depleted of both electrons and holes, presenting a barrier to majority carriers and a low resistance path to minority carriers. This drives the collection of minority carriers which are photogenerated throughout the *P* and *N* layers and reach the junction by diffusion as shown in Fig. 1.4.

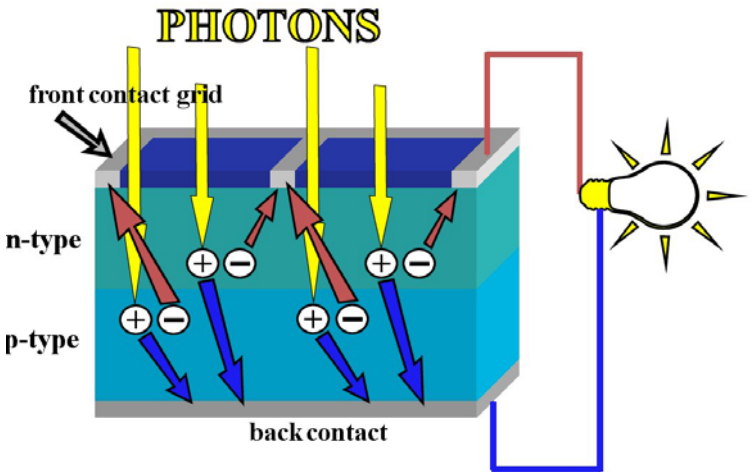

Figure 1.4 In an electrical circuit, the illuminated photovoltaic cell takes the place of a battery.

A photovoltaic cell can take the place of a battery in a simple electrical circuit. While not being illuminated, a cell does not provide energy to the circuit. However, when illuminated by light it develops a potential, or electromotive force (e.m.f.), analogous to the e.m.f. of a battery. The voltage developed when the terminals are isolated (infinite load resistance) is called the open circuit voltage V_{oc}, while the current drawn when the terminals are connected together is the short circuit current I_{sc}. For any intermediate load resistance R_L the cell develops a voltage V between 0 and V_{oc} and delivers a current I such that $V=IR_L$, where $I(V)$ is determined by the current-voltage characteristic of the cell under a particular illumination. Thus both I and V are determined by the illumination as well as the load. Since the current is roughly proportional to the illuminated area, the short circuit current density J_{sc} is the useful quantity for comparison. These quantities are defined for a simple, ideal diode model of a photovoltaic cell [9].

1.2.3 MATERIALS FOR PHOTOVOLTAIC CELLS

Silicon is the one of the most abundant material in the world and, it has a suitable band gap for photovoltaic energy conversion. Consequently it is nowadays the most common material for commercial photovoltaic cells. Silicon is a group IV element which adopts the tetrahedral crystal structure at room temperature and atmospheric pressure. This element has an indirect band gap of 1.1 eV, which reduces the optical absorption compared to direct gap semiconductors. Direct optical transitions occur in silicon at photon energies above 3 eV which is far above the theoretical optimum of 1.4 eV for photovoltaic conversion. The significant requirement for high purity silicon as well as the process to create monocrystalline elements increases its production cost (which normally makes up to 40-50% of the total cost of a finished module). Another detail worth mentioning is that since its absorption coefficient is low, a relatively thick layer of silicon is needed (in conventional silicon designs) to absorb sunlight effectively.

Due to these material constraints, a number of alternative semiconductor materials have been developed for photovoltaic applications. These selected materials are all strong light absorbers and only need to be about 1 micrometer thick to absorb the majority of the incident photons, so material costs are significantly reduced. Good thin film materials

should be low cost, non-toxic, robust and stable. They should absorb light more effectively than silicon. Higher absorption reduces the required cell thickness and so relaxes the requirement for long minority-carrier diffusion lengths, allowing polycrystalline or amorphous materials to be used. For high theoretical conversion efficiencies ($\geq$ 30%), the band gap should lay in the range 1-1.6 eV and we need to be able to produce a *P-N* junction of good quality. For acceptable photocurrent levels, the quantum efficiency should be high over a broad range of wavelengths. This means that the diffusion lengths must be long compared to the absorption depth, which places high demands on the crystal quality. These requirements limit the range of materials which can be used. The most common materials for thin film photovoltaic devices are amorphous silicon (a-Si, still silicon, but in a different form), or polycrystalline materials such as cadmium telluride (CdTe) and copper indium diselenide (CIS).

Each of these three materials is compatible for large area deposition (on to substrates of about 1 square meters) and hence high volume manufacturing. Thin film semiconductor layers are deposited onto either ITO coated glass or stainless steel sheets. Cell designs aims at reducing cost by using less pure or less quantity of semiconductor materials in thin film photovoltaic cells. These "thin film" materials are usually produced by physical or chemical deposition techniques which can be applied to large areas and fast throughput.

In a limited number of materials like cadmium telluride, copper indium diselenide and other related compounds and alloys, it has been found possible to produce efficient and stable photovoltaic cells using low cost methods of deposition [10, 11]. These materials present the advantage of not being severely affected in terms of performance by the presence of grain boundaries, residual unwanted impurities and other crystal defect, as observed in the III-V compounds. These materials also have near optimum energy band gaps and high optical absorption coefficients, although the best values of their minority carrier properties (lifetime, mobility and diffusion length) are not as good as those of the III-V compounds. CIS constitutes a new generation in PV technology [12]. Efficiencies are very promising at 17.7% for cells, 14% for submodules and 11% for modules. Not

surprisingly for a semiconductor based on several elements, the current research focus is on deposition processes and alloying. Okimura et al. [13] have reported that $Cu_{2-x}Se$ layer over n-Si single crystal substrates show an efficiency of 8.8% under a 75 $mWcm^{-2}$ illumination power. CdTe/CdS and $CuInSe_2$/CdS thin film photovoltaic cells present the best possibilities as of today for fabricating photovoltaic cell modules able to compete favourably with thin film arrays based on Si or Cu_2S/CdS [14]. Hence in the present study the ternary semiconductor material $CuInSe_2$ has been selected for investigation as a potential material for thin film photovoltaic cell applications. And considerable development work and device analysis are necessary to enhance the efficiencies of these thin film photovoltaic cells to acceptable values.

1.3 COPPER INDIUM DISELENIDE- Antecedents

CIS, being an I-III-VI_2 ternary compound, crystallizes in the structure of the mineral chalcopyrite $CuFeS_2$. In their crystal and electronic structure, these chalcopyrites are derived from zinc blende (sphalerite) compounds. The chalcopyrite CIS unit cell is shown in Figure 1.5. The bonding situation between Cu-Se and In-Se shows a mixed covalent and ionic bonding character. In this compound, two cations (copper and indium) have four anions (selenium) as near neighbours, while each anion is surrounded by two cations (copper and indium). Second neighbour interactions lead to an ordered array of copper and indium atoms and, as a result, a doubling of the unit cell is necessary to describe the chalcopyrite structure. The projection of each half of the unit cell on the (001) plane shows that the positions of the copper and indium atoms are inverted in the lower and upper part. Generally the bond strengths between Cu-Se and In-Se atoms are different, resulting in the shift of anions from their tetrahedral centered position towards the two copper atoms.

In addition, the unit cell of CIS is tetragonally distorted along the *c*-axis so that the unit cell of the structure is also characterized by the ratio $\delta=c/a$, which has an ideal value of $\delta=2.005$. If the two cations (copper and indium) are randomly distributed, the δ distortion will be removed and the lattice transforms into the cubic sphalerite structure. This phase transformation occurs in CIS at temperatures above 810 °C when apparently the entropy

contribution to the free energy favours the more random distribution of copper and indium atoms. The properties of CIS are given in Table 1.2.

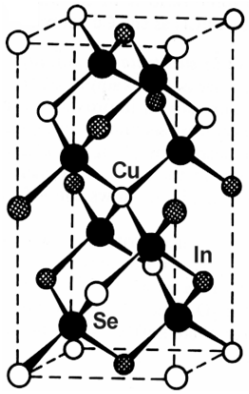

Figure 1.5 Chalcopyrite CIS unit cell.

Table 1.2 Properties of Copper Indium diselenide.

S. No	Property	Value
1	Formula	$CuInSe_2$
2	Energy gap	1.04 eV
3	Absorption Coefficient	10^5 cm^{-1}
4	Mobility, μ_n	100-1000 cm^2 V^{-1} S^{-1} (at 300 K)
5	Mobility, μ_p	50-180 cm^2 V^{-1} S^{-1} (at 300 K)
6	Molecular Weight	336.28 u
7	Density	5.77 gm cm^{-3}
8	Colour	Gray
9	Melting temperature	986 °C
10	Transition to sphalerite structure	810 °C
11	Lattice parameters *a*, *c*	a=5.789 Å; c=11.62 Å
12	Thermal conductivity	0.086 W cm^{-1} K^{-1}
13	Resistivity (Polycrystalline thin films) Copper rich	0.001 Ω cm
14	Resistivity (Polycrystalline thin films) Indium rich	>100 Ω cm

The development of photovoltaic device structures based on the I-III-VI_2 group of ternary compounds, especially copper indium diselenide, has rapidly advanced during the last few years. Copper indium diselenide ($CuInSe_2$ or CIS) is a direct gap semiconductor

with a band gap value of about 1.04 eV and has the highest optical absorption known for any semiconductor. This high value of the optical absorption α (10^5 cm^{-1}) implies that 99% of the incoming photons are absorbed within the first micrometer of the material. As a result, only about 1 μm of this material is required to effectively absorb the most incoming photons, which makes it attractive for thin film photovoltaics. As thin films of CIS with both *N*-type and *P*-type conductivity can be prepared easily, both homojunction and heterojunction potential exist for this material. On the other hand, CIS forms an ideal heterojunction with CdS, since the lattice mismatch between chalcopyrite $CuInSe_2$ and hexagonal CdS is only about 1.2%. Devices based on CIS have achieved high efficiencies of 14.8% [15] and 11.7% [16] respectively on both small and 1 square feet sizes. This 14.8% conversion efficiency is close to the target value of 15% for commercial bulk power applications of the Electric Power Institute and Department of Energy, USA.

$CuInSe_2$ in polycrystalline thin film form has been widely used for the fabrication of photovoltaic cells [17]. No evidence for either long or short term device degradation, as has been found in silicon devices, is observed in $CuInSe_2$ photovoltaic cells [18]. CIS can be obtained by several deposition techniques like: hot wall deposition [19,20], electrodeposition [21-23], metal organic chemical vapor deposition [24], selenization [25, 26], pulsed excimer laser ablation [27], close space vapor transport [28,29] and sputtering [30].

The structural properties of $CuInSe_2$ thin films have been studied by several researchers [31-39]. Kundu et al. [31] have reported that CIS films crystallize in a chalcopyrite structure with a certain amount of secondary phases (Cu-In, Cu-Se and In-Se). However as the annealing temperature increases, these Cu and In binary phases tend to rearrange into a chalcopyrite structure. Large areas of polycrystalline CIS thin film has been electrodeposited on Mo and ITO/In_2Se_3 substrates by Kampmann et al. [32]. They found that their best cell with a Mo/CIS/CdS/ZnO structure, yielded a preliminary efficiency of 4.8%. The epitaxy is very sensitive to the preparation of the surface and improves with increasing temperatures [33]. Ueno et al. [34] have electrodeposited CIS films on titanium substrates. The X-ray diffractogram of as-deposited films did not exhibit

the characteristic peaks of chalcopyrite when the films were annealed at 600 °C for one hour in nitrogen atmosphere. Park et al. [35] have reported that CIS films crystallize in a chalcopyrite structure, and that the amount of the secondary phase ($Cu_{2-x}Se$) increases while increasing copper content. Polycrystalline CIS thin films have been electroplated on titanium substrates by Gomez et al. [36]. They have reported the presence of both chalcopyrite and sphalerite phases in the as-deposited films, but just a simple chalcopyrite phase after annealing. Pern et al. [37] have studied the effect of annealing on structural characteristics of CIS films. They have observed that the annealed copper rich films are predominantly chalcopyrite and the effective grain size increased as the annealing temperature and time increased. Hama et al. [38] have reported the structural properties of CIS films prepared by three source coevaporation and selenization of Cu/In/Se stacked layers. Guillen et al. [39] have obtained CIS films rich in selenium and this excess Se was removed after annealing the films at 400 °C for fifteen minutes.

Optical properties of $CuInSe_2$ thin films have been studied by numerous research groups [40-45]. Firozhasan et al. [40] have studied the optical properties of CIS films prepared by in-situ thermal annealing of stacks of successively evaporated elemental layers. Direct allowed and direct forbidden transitions were observed in the deposited films, and the transition energies were found to be dependent on the composition of the films. Thin films of CIS have been prepared by selenising co-sputtered Cu-In films with selenium vapor by Schmidt et al. [41]. The films were found to have an optical band gap in the range of 0.96 to 1.0 eV. Sahu et al. [42] have reported a direct band gap of 1.1 eV for electrodeposited CIS films. An optical band gap of 1.07 eV has been reported by Kim and Im [43] for selenised CIS films. Padam et al. [44] have stated that CIS thin films have a direct band gap of 1.04 eV, which lies in the energy range for optimum photovoltaic conversion, as well as a high optical absorption coefficient of the order of 10^5 cm^{-1}. Wemple [45] has calculated the refractive index of CIS films using its transmittance spectrum, and has found the values to be in the range 2.4 to 3.18.

Many research groups have carried out electrical characterization studies on CIS thin films [46-49]. Guillen and Herrero [46] have studied the electrical properties of as-

grown and heat-treated CIS films in the temperature range 30-300 K. They have observed a variable range hopping conduction mechanism in lower temperatures and a thermally activated conduction mechanism in the temperature range close to room temperature. The activation energy was found to decrease with annealing.

The effect of composition on the electrical conductivity of CIS films has been studied by Varela et al. [47]. The conductivity and thermal activation energy was found to be dependent on the Cu/In ratio. Datta et al. [48] have reported the conductivity of CIS films of different compositions in the temperature range 100-350 K. They have observed that the electrical data of post-deposition anneal in air and subsequently in hydrogen were in good agreement with the Meyer-Neldel type of conduction. Senthil et al. [49] have carried out D.C. conduction studies on thermally evaporated CIS thin films, and the activation energy was reported as 0.27 eV.

Hall Effect studies have been carried out using the Van der Pauw technique by Soliman [50] and Abo El Soud et al. [51]. Copper rich films have been reported to be *P*-type and indium rich films as *N*-type. The photoconductive properties of CIS thin films have been studied by several research groups [52-54]. Tomar and García [55] have demonstrated the feasibility of preparing thin film photovoltaic cell with structure Zn/*P*-CIS/*N*-CdS using spray pyrolysis technique. Vidyadharan Pillai and Vijayakumar [56] have characterized CIS/CdS thin film photovoltaic cells prepared by chemical bath deposition, and have reported a 3.1% cell efficiency. Masse and Djessas [57] have deposited CIS thin films using close-spaced vapour transport technique and have studied the photovoltaic effect exhibited by CIS/SnO_2 structures. Bindy et al. [58] have prepared CIS thin films through a new selenisation process using chemical bath deposited selenium. They have studied the compositional dependence of the growth process using various Cu/In ratios. The optical band gap was found to decrease while increasing the copper to indium ratio. Tanaka et al. [59] have studied the radiation damage effect on the electrical properties of CIS thin films deposited by R.F. diode sputtering. It has been observed that the films are of *N*-type with a carrier concentration and Hall mobility of $3x10^{16}$ cm^{-3} and 40 cm^2 $V^{-1}s^{-1}$ respectively. Lee et al. [60] have recently reported that as-deposited CIS thin films are *N*-

type with carrier concentration of $4x10^{16}$ cm^{-3} and mobility of 120 cm^2 $v^{-1}s^{-1}$. Lee et al. [61] have reported that CIS photovoltaic cells with a 100 nm thick CIS layer show the best active layer efficiency of 9.59%. Nancheva et al. [62] have deposited CIS films by D.C. magnetron sputtering and have reported that the crystallinity of the films improved while increasing the deposition temperature.

Electrodeposited CIS thin films have been prepared by Xu et al. [63]. They have studied the effect of annealing on the structural properties, and have observed that short annealing time is necessary to avoid losing Se content to obtain *P*-type CIS films for photovoltaic cell applications. Malar et al. [64] have reported that CIS thin films deposited by flash evaporation at a substrate temperature of 300 °C exhibited well-defined grains with an average grain size of 390 Å. Chalcopyrite CIS films have been prepared by Guillen and Herrero [65] using close-space selenisation at 400 °C in vacuum and have reported that films selenised under $4x10^{13}$ mbar show rough surfaces with globular structures. CIS thin film photovoltaic cells with molybdenum back contacts have been fabricated by Meyer and Vanbyk [66]. They have used CdS and ZnO as the buffer and window layers, respectively. After an outdoor exposure of 130 kW H/m^2 they have observed the efficiency of the CIS modules degrade by 10%.

One of the main problems of using CIS as the absorber layer in photovoltaic applications is obtaining suitable thin films over a large area at a low cost. Research into thin film deposition of this compound has proceeded along various routes, like thermal evaporation, electron beam evaporation, flash evaporation and spray pyrolysis. These techniques have so far failed to establish firmly a single process that can deliver the high level of reproducibility and control that this complicated material requires.

The structure and chemistry of CIS and its use in photovoltaic cell applications have been discussed in detail by Rockett et al. [16]. According to their work, properties and device performance were divided into those dominating common CIS and those relevant to the material in its best configuration. While the ideal state of CIS is related to that with less defect points, strongly (112) oriented and with nearly perfect grains, common CIS is a non-

equilibrium material containing numerous lattice defects and secondary phases surrounding the grains. This material is capable of producing photovoltaic cells yielding in excess of 10% conversion efficiency provided that there is no Cu_xSe phase present. It has also been stated in their work that the growth techniques used in depositing CIS thin films, especially physical vapour deposition processes, are generally far from equilibrium. Thus the questions of when and where the secondary phases are formed are important for understanding the processes behind the performance behavior of thin film CIS devices as well as for improving CIS production technologies.

In order to attain an adequate process for massive cell production, it is essential to use a method that avoids interruptions due to time-consuming tasks like changing chemicals or other consumable elements in the associated production line, as it is the case with chemical bath deposition processes. Sputtering deposition technique satisfies this condition. In the sputtering deposition technique, energetic ions are used to knock atoms or molecules out from a target that acts as one electrode and subsequently deposit them on a substrate acting as another electrode. In the case of deposition of semiconductor materials, an alternate (radio frequency) electric field is applied to generate plasma between two electrodes. The various processes occurring during the deposition of thin films by sputtering technique have been theoretically analyzed by Maissel et al. [67]. The detailed literature survey above shows that only very limited studies have been carried out on CIS films deposited by R.F. sputtering technique [68,69]. M. M. Gómez et al. [68] have produced nanocrystalline photovoltaic cells by incorporation of CIS-dithiocyanato-bis ruthenium (II) into sputter deposited titanium oxide films. They achieved photoelectric conversion efficiency as high as 7% for a photovoltaic intensity of 100 W/m^2. CIS photovoltaic cells produced on polyimide foils by roll to roll process using sputter and evaporation techniques were produced by Spemann et al. [69].

1.4 CADMIUM SULFIDE-Antecedents

Cadmium Sulfide (CdS) is an II-VI semiconductor compound with band gap energy of 2.43 eV for the material in bulk form, which lays over the majority of the solar radiation spectrum energies. CdS thin films find their potential applicability in the areas of high

efficiency photovoltaic cells. They are used especially as a partner material as well as very suitable window layer for $CuInSe_2$ and CdTe based photovoltaic cells. The *N*-CdS is an essential component for the union *P*-CIS in order to achieve greater efficiency. The fundamental requirements for a CdS layer are that it must be a highly conductive ($\sigma \approx 10^{16}$ S m^{-1}), thin film that allows a high transmission of the incident radiation, with a high uniformity to eliminate the possibility of a short circuit in the cell. Various properties of CdS are given in Table 1.3.

Table 1.3 Properties of Cadmium Sulfide

S. No	Property	Value
1	Formula	CdS
2	Energy gap	2.43 eV
3	Absorption Coefficient for 0.4μm	$1.6x10^4$ cm^{-1}
4	Mobility, μ_n (monocrystal)	340 cm^2 V^{-1} S^{-1}
5	Mobility, μ_p (monocrystal)	50 cm^2 V^{-1} S^{-1}
6	Mobility, μ_n (polycrystal)	1-5 cm^2 V^{-1} S^{-1}
7	Mobility, μ_p (polycrystal)	1-5 cm^2 V^{-1} S^{-1}
8	m_n/m_0	0.16
9	m_p/m_0	0.8
10	N_c	$2.19x10^{18}$ cm^{-3}
11	N_v	$1.44x10^{20}$ cm^{-3}
12	Lattice parameters *a*, *c* (hexagonal phase)	*a*=4.14 Å ; *c*=6.71 Å
13	Lattice parameters a_0 (cubic phase)	a_0=5.82 Å
14	Time life of minority carriers	0.06-1 ns

The most commonly used methods for depositing CdS thin films are vacuum evaporation [70-72], sputtering [73-75], spray pyrolysis [76-78], molecular beam epitaxy [79-81], electrodeposition [82-84] and chemical bath deposition (CBD) [85-87].

Chemical bath deposition is an “electroless” technique that is attractive as a simple and low cost method for achieving good-quality CdS films. It is a chemical method based on the controlled decomposition of thiourea in an alkali solution with the presence of Cd^+

ions. This deposition technique is appropriate for coating surfaces of any morphology and geometry. In the original work of Kaurs [88] cadmium acetate was used and the reaction involved is as follows:

$$Cd(CH_3COO)_2+SC(NH_2)_2 \rightarrow CdS(s)+H_2CN_2+2CH_3COO+2H_2O \quad (1.10)$$

There are many variations to this chemical bath deposition method. The films obtained at a solution temperature of 90 °C were heterogeneous. The BP group [81, 82] has reported CdS films that show 10-20% cadmium excess in relation to sulfur, which is attributed to the presence of $Cd(OH)_2$ and CdO [85, 89-94]. A deposition mechanism, where reversible adsorption of dihydroxo-cadmium species is formed from the tetra amino cadmium complex has been proposed by Ortega -Borges and Lincot[95].

$$Cd(NH_3)_4^{2+}+SC(NH_2)_2+2OH^- \rightarrow CdS+CH_2N_2+4NH_3+2H_2O \quad (1.11)$$

It is well known that the deposition conditions (bath composition, reagent concentrations, temperature, pH, etc.) strongly influence the film stoichiometry, microstructure and crystallinity, which in turn determine the optical and electrical properties of CdS films [96].

Band gap values up to 2.58 eV for chemically bath deposited CdS thin films based on the substitution of ammonia by sodium citrate as the complexing agent in the reaction solution have been achieved by Sandoval et al. [97]. In another work, CdS thin films have been grown using a modified chemical bath deposition method by Archbold et al. [98]. The complexing agent used was ethylenediamine, which enabled the use of low cadmium concentrations. The films obtained were homogeneous with no visible pinholes and showed both cubic and hexagonal structures. According to Çetinörgü et al. [99], annealing the chemically deposited films in air resulted in a shift of the absorption edge towards higher wavelengths and a decrease in the gap value from 2.45 to 2.38 eV.

1.5 CONCLUSIONS

The presented literature review on CIS/CdS photovoltaic cells has been conducted with the objective of revealing the highest possible conversion efficiencies as well as the processes and parameters used to attain them. As it can be noted, many of the researches mentioned have focused on empiric methods of study. This approach has created the technology that is currently being used in the semiconductor industry. However, the polycrystalline characteristic of the thin films that on one hand makes them economically attractive for the industry, on the other hand is also responsible for some of its associated technical difficulties. That said, many of the steps involved in the fabrication of the cells are correlated and have influence over critical parameters of the finished products.

The research effort on photovoltaics is currently focused on the fabrication of a new generation of photovoltaic cells. One can conclude from the detailed analysis of the current literature that for tapping the full potential of CIS and CdS as material components for thin film photovoltaic cells, further studies on the different deposition techniques are required. Particularly, limited work has been done on CIS films prepared by R.F. sputtering deposition compared to any other methods of preparation. As it has been previously mentioned, cell properties are very sensitive to the method and conditions of preparation; therefore the analysis of parameters such as structural, optical, electrical and dielectrical properties as well as photo sensitivity is of great importance to properly analyze the potential of this deposition technique.

The aim of the present work is to establish the best deposition conditions for each element of a complete photovoltaic cell, such as the window layer, the absorber layer and top and back contacts. This task is to be done by the analysis and characterization of films deposited with a variety of conditions, using different deposition techniques: R.F. sputter deposition for CIS and ITO (top contact), microwave assisted chemical bath deposition for CdS and D.C. sputter deposition for Molibdenum (back contact).

In the present work I have adopted the following methodology:

I. Deposit CIS films by R.F. sputtering using different values of power, distances between substrate and target, substrate temperatures and deposition times.
II. Deposit CdS films by microwave assisted chemical bath deposition using various deposition times and doping materials concentrations
III. Deposit ITO and Mo by R. F. and D. C. sputtering respectively
IV. Analyze the crystal structure and the surface morphology of the deposited films by X-ray diffraction (XRD) and Scanning Electron Microscopy (SEM).
V. Perform the composition analysis using Energy-dispersive X-ray analysis (EDAX).
VI. Calculate the optical parameters such as absorption coefficient, refractive index, band gap energy and extinction coefficient.
VII. Sensitize the films by annealing in nitrogen atmosphere at different temperatures, and study the electrical and optical properties of the modified films.
VIII. Study the influence of light on the dielectric properties of the deposited films.

REFERENCES

[1] IPCC, Climate Change Report, 17th November 2007, Valencia, Spain

[2] Charles Kittel, Introduction to solid state physics, Seventh edition, John Wiley and Sons, Inc, New York, 1996

[3] P. V. Pavlov, A. F. Joslov, Física del estado sólido, Editorial Mir, Moscú 1985

[4] S. M. Sze, Physics of semiconductor devices, John Wiley and Sons, N. Y. 1985

[5] K. L. Chopra, Thin film phenomena, Mc Graw Hill, New York, 1969

[6] Donald R. Askeland, Science and Engineering of Materials, third edition, Wadsworth Publishing Company, Boston 1994, p. 619

[7] Jenny Nelson, The Physics of Solar Cells, Imprerial College, UK 2003

[8] Hook, J. R., H. E. Hall, Solid State Physics, John Wiley & Sons, 2001

[9] Osvaldo Vigil Galán, Andrés Martel Alberto, Física de semiconductores, IPN, México, D. F., 2000

[10] R. W. Miles, Vacuum, 80 (2006) 1090-1097

[11] Torres Luis, Alternativenergy, BP Solar, 11th march 2006, Valencia España

[12] R. D. McConnell, T. Surek, C. E. Witt, Renewable energy, 15 (1998) 502-505

[13] H. Okimura, T. Matsumae, R. Makabe, Thin Solid Films, 71 (1980) 53

[14] K. L. Chopra, S. R. Das, Thin Film Solar Cells, Plenum Press, New York, (1983) 426

[15] L. Stolt, M. Bodegard, J. Kessler, M. Ruckh, K. O. Velthaus, H.W.Schock, Proceedings of 11th EC Photovoltaic Solar Energy Conference, Montreux, Switzerland, (1992)

[16] A. Rockett, F. Abou-Elfotouh, D. Albin, M. Bode, J. Erner, R. Klenk, T. C. Lommasson, T. W. F. Russell, R. D. Tomlinson, J. Tuttle, L. Stolt, T. Walter, T. Peterson, Thin Solid Films, 237 (1994) 1

[17] J. Hedstrom, M. Bodegard, A. Kylner, L. Stolt, D. Hariskon, H. W. Schock, Proceedings of 23rd IEEE Photovoltaic Specialists Conference, New York, (1993)

[18] Wilhelm Durisch, King-Hang Lam, Josie Closel, Applied Energy, 83 (2006) 1339-1350

[19] S. Agilan, D. Mangalaraj, Sa.K. Narayandass, S. Velumani, Alex Ignatiev, Vacuum, 81 (2007) 813-818

[20] S. Agilan, S. Venkatachalam, D. Mangalaraj, Sa. K. Narayandass, S. Velumani, G. Mohan Rao, Vijay P. Singh, Materials Characterization, 58 (2007) 701-707

[21] K.T.L. De Silva, W. A. A. Priyantha, J. K. D. S. Jayanetti, B. D. Chithrani, W. Siripala, K. Blake, I. M. Dharmadasa, Thin Solid Films, 382 (2001) 158-163

[22] R. P. Raffaelle, T. Potdevin, A. F. Hepp and S. G. Bailey, Materials Science in Semiconductor Processing, 2 (1999) 289-296

[23] N. B. Chaure, J. Young, A. P. Samantilleke, I. M. Dharmadasa, Solar Energy Materials and Solar Cells, 81 (2004) 125-133

[24] Seok Hwan Yoon, Thin Solid Films, 515 (2006) 1544-1547

[25] Markus E. Beck, Michael Cocivera, Thin Solid Films, 272 (1996) 71-82

[26] G. Gordillo, C. Calderón, W. Bolaños, E. Romero, Superficies y Vacío, 16 (2003) 12-15

[27] P. Victor, J. Nagaraju, S. B. Krupanidhi, Solid State Communications, 116 (2000) 649-653

[28] M. D. Kannan, R. Balasundaraprabhu, S. Jayakumar, P. Ramanathaswamy, Solar Energy Materials and Solar Cells, 81 (2004) 379-395

[29] O. Vigil-Galán, E. Sánchez-Meza, J. Sastré-Hernández, F. Cruz-Gandarilla, E. Marín, G. Contreras-Puente, E. Saucedo, C.M. Ruiz, M. Tufiño-Velázquez, A. Calderón, Thin Solid Films, 516 (2008) 3818-3823

[30] John H. Scofield, A. Duda, D. Albin, B. L. Ballard, P. K. Predecki, Thin Solid Films, 260 (1995) 26-31

[31] S. N. Kundu, D. Bhattacharyya, S. Chaudhuri, A. K. Pal, Materials Chemistry and Physics, 57 (1999) 207-313

[32] A. Kampmann, V. Sittinger, J. Rechid, R. Reineke-Koch, Thin Solid Films, 361-362 (2000) 309-313

[33] M. J. Furlong, M. Froment, M. C. Bernard, R. Cortès, A. N. Tiwari, M. Krejci, H. Zogg, D. Lincot, journal of Crystal Growth, 193 (1998) 114-122

[34] Y. Ueno, H. Kawai, T. Sugiur, H. Minoura, Thin Solid Films, 157 (1988) 159

[35] Y. W. Park, G. Y. Chung, G. T. Ahn, H. B. Im, J. S. Song, Thin Solid Films, 245 (1995) 174

[36] H. Gomez, R. Schrebler, L. Basaez, E. A. Dalchiele, Journal of Physics: Condensed Matter, 5 (1993) 349

[37] F. L. Pern, R. Noufi, A. Mason and A. Franz, Thin Solid Films, 202 (1991) 299

[38] T. Hama, T. Ihara, H. Sato, H. Fujisawa, M. Ohsawa, Y. Ichikaea and H. Sakai, Solar Energy Materials, 23 (1991) 380

[39] C. Guillen, E. Galiano, J. Herrero, Thin Solid Films, 202 (1998) 137

[40] S. M. Firozhasan, L. Quadir, Kh. S. Begum, M. A. Subhan, Kh. M. Mannan, Solar Energy Materials and Solar Cells, 58 (1999) 349-360

[41] J. Schmidt, H. H. Roscher, R. Labusch, Thin Solid Films, 251 (1994) 116

[42] S. N. Sahu, R. D. L. Kristensen, D. Hanemann, Solar Energy Materials and Solar Cells, 18 (1989) 385

[43] S. J. Kim, H. B. Im, Thin Solid Films, 214 (1992) 454

[44] G. K. Padam, G. L. Malhotra and S. K. Gupta, Solar Energy Materials, 22 (1991) 303

[45] S. H. Wemple, Journal of Applied Physics, 46 (1975) 3597

[46] C. Guillen, J. Herrero, Journal of Applied Physics, 46 (1975) 3597

[47] M. Varela, J. L. Morenzza, J. Esteve, J. M. Codina, Journal of Physics: Applied Physics, 17 (1984) 2423

[48] T. Datta, R. Noufi, S. K. Deb, Applied Physics Letter, 47 (1985) 1102

[49] K. Senthil, D. Nataraj, K. Prabakar, D. Mangalaraj, Sa. K. Narayandass, N. Udhayakumar, N. Krishnakumar, Materials Chemistry and Physics, 2395 (1999) 1

[50] L. I. Soliman, Indian Journal of Applied Physics, 32 (1993) 166

[51] A. M. Abo El Soud, H. A. Zayed, L. I. Soliman, Thin Solid Films, 229 (1993) 232

[52] V. Ramanathan, T. Datta, R. Noufi, Applied Physics Letters, 51 (1987) 7

[53] A. Vahid Shahidi, I. Shih, T. Araki, C. H. Champness, Solar Energy Materials, 12 (1985) 383

[54] A. Vahid Shahidi, I. Shih, T. Araki, C. H. Champness, Journal of Electronic Materials, 14 (1985) 297

[55] M. S. Tomar, P. J. Garcia, Thin Solid Films, 90 (1982) 419

[56] P. K. Vicyadharan Pillai, K. P. Vijayakumar, Solar Energy Materials and Solar Cells, 51 (1998) 47

[57] G. Masse, K. Djessas, Thin Solid Films, 257 (1995) 137

[58] K. Bindu, C. Sudha Kartha, K. P. Vijayakumar, T. Abe, Y. Kashiwaba, Solar Energy Materials and Solar Cells, 79 (2003) 67-79

[59] T. Tanaka, T. Yamakuchi, A. Wakahara, A. Yoshida, R. Toniguchi, Y. Matsuda, M. Fujishiro, Solar Energy Materials and Solar Cells, 75 (2003) 115

[60] H. S. Lee, H. Okada, A. Wakahara, A. Yoshida, T. Ohshima, H. Itoh, S. Kawakita, M. Imaizumi, S. Matsuda, Solar Energy Materials and Solar Cells, 75 (2003) 109

[61] D. Y. Lee, J. H. Yun, K. H. Yoon, B. T. Ahn, Thin Solid Films, 410 (2002) 171

[62] N. Nancheva, P. Docheva, N. Djourelov, M. Balcheva, Materials Letters, 54 (2002) 169

[63] J. L. Xu, X. F. Yao, J. Y. Feng, Solar Energy Materials and Solar Cells, 73 (2002) 203

[64] P. Malar, S. Kasiviswanathan, R. Devanathan, V. Damodara Das, Materials Research Bulletin, 37 (2002) 659

[65] C. Guillen, J. Herrero, Vacuum, 67 (2002) 659

[66] E, K, Meyer, E. E. Vanbyk, Renewable Energy, 28 (2003) 1455

[67] Leon I. Maissel, Reinhard Glang, Handbook of Thin Film Technology, Mc Graw Hill 1970

[68] M. M. Gómez, J. Lu, E. Olsson, A. Hagfeldt, C. G. Granqvist, Solar Energy Materials and Solar Cells, 64 (2000) 385-392

[69] D. Spemann, R. Deltschew, M. Lorenz, T. Butz, Nuclear Instruments and Methods in Physic Research Section B: Beam Interactions with Materials and Atoms, 219-220 (2004) 693-698

[70] Zhibing He, Gaoling Zhao, Wenjian Weng, Piyi Du, Ge Shen, Gaorong Han, Vacuum, 79 (2005) 14-18

[71] Jae-Hyeong Lee, Dong-Gun Lim, Jun-Sin Yi, Solar Energy Materials & Solar Cells, 75 (2003) 235-242

[72] K. Senthil, D. Mangalaraj, Sa.K. Narayandass, R. Kesavamoorthy, G.L.N. Reddy, B. Sundaravel, Physica B: Condensed Matter, 304 (2001) 175-180

[73] Jae-Hyeong lee, Dong-Jin Lee, Thin Solid Films, 515 (2007) 6055-6059

[74] P. K. Ghosh, U. N. Maiti, K. K. Chattopadhyay, Materials Letters, 60 (2006) 2881-2885

[75] Byung-Sik Moon, Jae-Hyeong Lee, Hakkee Jung, Thin Solid Films, 511 – 512 (2006) 299 – 303

[76] J. Hiie, T. Dedova, V. Valdna, K. Muska, Thin Solid Films, 511-512 (2006) 443-447

[77] V. Krishna Kumar, K. Ramamurthi, E. Elangovan, Solid State Communications, 132 (2004) 673-677

[78] F. Atay, S. Kose, V. Bilgin, I. Akyuz, Materials Letters, 57 (2003) 3461-3472

[79] Joo Won Choi, A. Bhupathiraju, M. A. Hasan, John M. Lannon, Crystal Growth, 255 (2003) 1-7

[80] M. Grün, A. Storzum, M. Hetterich, A. Kamilli, W. Send, Th. Walter, C. Klingshirn, Crystal Growth, 201-202 (1999) 457-460

[81] A. Dinger, M. Hetterich, M. Göppert, M. Grün, C. Klingshirn, B. Weise, J. Liang, V. Wagner, J. Geurts, Crystal Growth, 200 (1999) 391-398

[82] Wenbin Yang, Zhi Wu, Zhongyuan Lu, Xuping Yang, Lixian Song, Microelectronic Engineering, 83 (2006) 1971-1974

[83] K. Premaratne, S. N. Akuranthilaka, I. M. Dharmadasa, A. P. Samantilleka, Renewable Energy, 29 (2003) 549-557

[84] N. W. Duffy, D. Lane, M. E. Ôzsan, L. M. Peter, K. D. Rogers, R. L. Wang, Thin Solid Film, 361-362 (2000) 314-320

[85] Joel Pantoja Enríquez, Xavier Mathew, Solar Energy Materials and Solar Cells, 76 (2003) 313-322

[86] G. Sasikala, P. Thilakan, C. Subramanian, Solar Energy Materials and Solar Cells, 62 (2000) 275

[87] K. S. Ramaiah, R. D. Pilkington, A. E. Hill, R. D. Tomlinson, A. K. Bhatnagar, Materials Chemistry and Physics, 68 (2001) 22

[88] I. Kaurs, D. K. Pandya, K. L. Chopra, Journal of Electrochemical Society, 127 (1980) 943

[89] K. D. Rogers, J. D. Painter, M. J. Healy, D. W. Lane, M. E. Özsan, Thin Solid Films, 339 (1999) 299-304

[90] K. D. Rogers, D. A. Wood, J. D. Painter, D. W. Lane, M. E. Özsan, Thin Solid Films, 361-362 (2000) 234-238

[91] Jorge G. Ibañez, Flora Gomez, Ivonne Konik, Diane E. Lozano, Journal of Chemical Education, 74 (1997) 1205

[92] Fuyi Chen, Wanqi Jie and Xiaomei Cai, Thin Solid Films, 516 (2008) 2823-2828

[93] P.J. Sebastian, H. Hu, Advanced Materials for Optical Electronics, 4 (1994) 407

[94] C. Guillén, M. A. Martínez, J. Herrero, Thin Solid Films, 335 (1998) 37

[95] R. Ortega Borges, D. Lincot, Journal of Electrochemical Society of India 144 (1997) 4081

[96] R. Grecu, E. J. Popovici, M. L. dar, L. Pascu, E. Indreaa, Optoelectronics and Advanced Materials, 6 (2004) 127-132

[97] M. G. Sandovel-Paz, M. Sotelo-Lerma, A. Mendoza-Galvan, R. Ramírez-Bon, Thin Solid Films, 515 (2007) 3356-3362

[98] M. D. Archbold, D. P. Halliday, K. Durose, T. P. A. Hase, D. S. Boyle, S. Mazzamuto, N. Romeo, A. Bosio, Thin Solid Films, 515 (2007) 2954-2957

[99] Çetionörgü, C. Gümüş, R. Esen, Thin Solid Films, 515 (2006) 1688-1693

CHAPTER II Experimental details

In this chapter, thin film deposition and characterization techniques, relevant to the present work are discussed in detail, in order to analyze various intricacies involved in the materials properties

2.1 INTRODUCTION

Thin films are generally defined as materials in two dimensional nanostructures, created by the process of condensation of atoms, molecules or ions, which acquire unique properties significantly different from those of the corresponding bulk materials as a result of their physical dimensions, geometry, and micro-structure. Additionally, these characteristic features of thin films can be drastically modified and adapted to obtain numerous desired physical properties, such as low resistivity, high transparency, etc.

Many methods developed for the deposition of thin films are widely used in industrial applications, which provide a great driving force for further development and improvement of these techniques. Choosing a film deposition technique for a determined application depends on several factors, such as the melting point of the material to be deposited, its stability, desired purity, process and materials costs, etc. However, different methods may attain similar material properties [1-4]. In general, thin film deposition techniques can be classified into two groups, namely chemical and physical methods.

2.2 PHYSICAL METHODS

When applying physical methods to thin film deposition, the vapour species of a solid material can be created either by thermal evaporation or mechanically knocking out the atoms or molecules from the surface by using energetic heavy particles. The process of deposition in the former case is referred to as vacuum evaporation and in the latter as sputtering. The thermal melting and consequent evaporation of the material to form a film on a substrate is achieved by various methods such as:

1. Thermal evaporation
2. Flash evaporation

3. Multi-source evaporation
4. R.F. Heating
5. Discharge-assisted evaporation, etc.

During a film deposition by sputtering, the vapour species may be produced either by establishing a glow discharge between the target and the substrate holder or by using a separate ion-beam source [5-7]. Accordingly, this method is referred to as glow discharge sputtering and ion-beam sputtering, respectively. The ions formed in the glow discharge are accelerated to impinge on the target material. The momentum transferred between the impinging ions and the atoms of the target enables the formation of a thin film [8-11]. This technique has become a viable process and is being applied on a large scale for various coatings. Several essential factors during sputtering depositions have been discussed by various researchers [7, 12-16].

Some major differences between evaporation and sputtering are briefly summarized below [17]:

1. The deposition pressure used differs significantly. Evaporation uses low pressures typically ranging from 10^{-3} to 10^{-10} Torr, whereas sputtering requires a relatively high pressure typically of ~100 Torr.
2. Atoms or molecules in an evaporation chamber do not typically collide with each other, whereas the atoms and molecules in sputtering do collide with each other prior to the arrival at the growth surface.
3. Evaporation is a process describable by thermodynamic equilibrium, whereas sputtering is not.
4. The growth surface (substrate) is not activated in evaporation, whereas in sputtering it is constantly under electron bombardment and thus is highly energetic.
5. Evaporated films consist of large grains, whereas sputtered films consist of smaller grains with better adhesion to the substrates.
6. Fractionation of multi-component systems is a serious challenge in evaporation, whereas target and film can share the same composition in sputtering.

2.2.1 R.F. SPUTTERING DEPOSITION

The key element of R.F. sputtering is that the target self-biases to a negative potential and behaves like a DC target. Such a self-negative target bias is a consequence of the fact that electrons are considerably more mobile than ions and have little difficulty in following the periodic change in the electric field [18]. To prevent simultaneous sputtering on the growth film or substrate, the sputter target must be an insulator and be capacitively coupled to the RF generator. This capacitor will have a low RF impedance and thus allow the formation of a DC bias on the electrodes.

Typical RF frequencies employed range from 5 to 30 MHz. However, 13.56 MHz has been reserved for plasma processing by the Federal Communications Commission and is widely used.

2.2.2 SPUTTERING UNIT

A schematic sketch and a photograph of the experimental setup of the coating system (sputtering and evaporative coating system, Intercovamex Model V3; Cuernavaca Morelos) used in the present study are shown in Figures 2.1 and 2.2. The system can be subdivided into three main parts, namely, the vacuum chamber, the pumping system and the control panel. The vacuum chamber is linked with the pumping system, which consists of a rotary pump and reaches atmospheric pressure up to 10^{-3} Torr and a turbo-pump which reaches 10^{-3} to 10^{-6} Torr. Pirani and cold cathode gauges are provided for the measurement of the pressure inside the vacuum chamber.

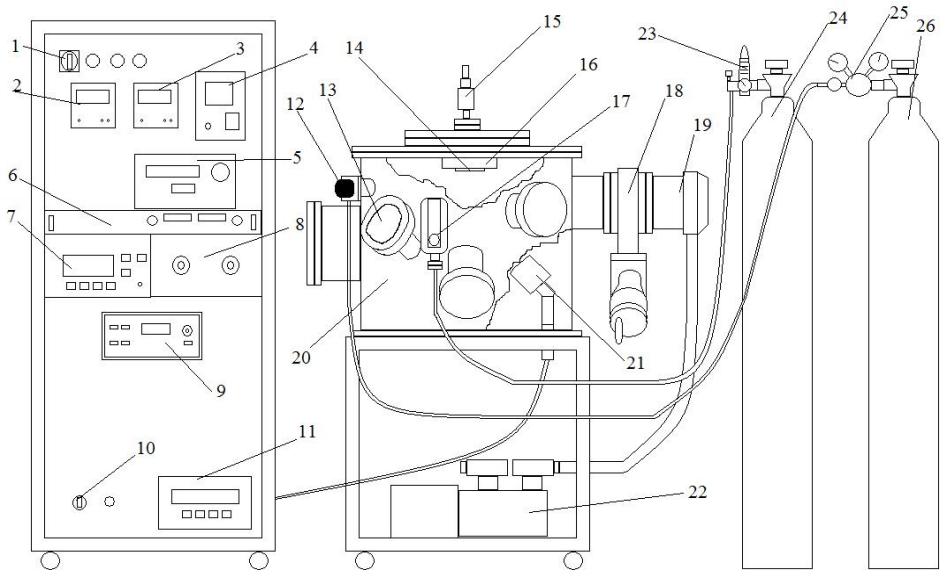

Figure 2.1 Sketch of coating unit.

1. Main switch
2. Pirani gauge
3. Cold cathode gauge
4. Heater controller
5. Thickness monitor
6. Evaporation power supply
7. R.F. sputtering power supply
8. R.F. sputtering control panel
9. D.C. sputtering power supply
10. Rotary pump switch
11. Turbo pump control
12. Vent valve
13. Glass window
14. Substrate holder
15. Substrate rotating motor
16. Substrate heater
17. Argon valve
18. Vacuum valve
19. Turbo-pump
20. Vacuum chamber
21. Sputtering gun
22. Rotary pump
23. Argon flux meter
24. Argon tank
25. Nitrogen flux regulator
26. Nitrogen tank

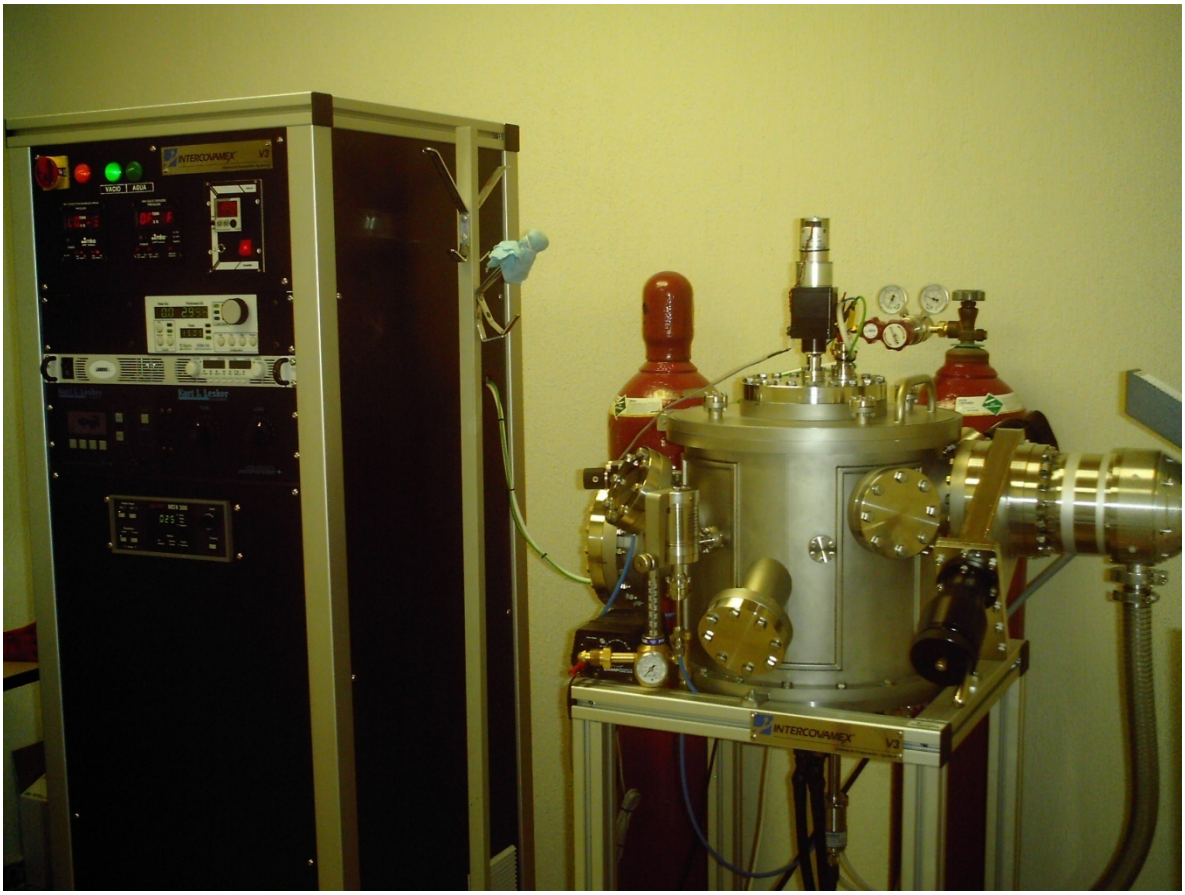

Figure 2.2 Photograph of the vacuum deposition unit.

2.2.3 SPUTTERING SET-UP

In order to achieve homogeneous two dimensional nanocrystalline thin films, the deposition procedure was as follows:

A substrate size of 38 mm x 25 mm was chosen. Substrate rotation at 60 rpm was used to achieve uniform deposition. Sintered ceramic targets of CIS of 2 inches diameter with 99.999% purity were used for the depositions. The separation between target and substrate was limited from 4.0 to 6.5 cm. Argon was used as the sputtering gas, which was controlled by a mass flow controller. The sputtering pressure was fixed at 6 x 10^{-3} Torr. After the chamber was evacuated to a base pressure below 9x10^{-5} Torr, a pre-sputtering process during 10 minutes was carried out at an argon gas pressure of 6x10^{-3} Torr in order to clean the target surface. The R.F. sputtering power was varied from 60 to 110 W. The films were deposited at 400 °C, with deposited thickness values of 1000-3000 nm.

2.3 CHEMICAL METHODS

Chemical methods are essentially subdivided into two groups: vapour-phase deposition and liquid-based growth.

Few examples of different vapour-phase chemical methods are: atmospheric pressure chemical vapour deposition, low pressure chemical vapour deposition, plasma-enhanced chemical vapour deposition and close-spaced vapour transport deposition. Some examples of liquid-phase chemical methods are: electro-deposition, anodization, spray pyrolysis and chemical bath deposition. As a whole, all chemical methods depend upon a specific chemical reaction for the formation of the films.

2.3.1 CHEMICAL BATH DEPOSITION

The chemical bath deposition technique (CBD) is based on the principle of solubility product equilibrium, which establishes that in a saturated solution of a poorly soluble compound, the product of molar concentrations of ions is constant at a given temperature [19]. Here, a saturated solution of an electrolyte in contact with its own solid phase originates a well-defined numerical relationship among the concentrations of ions in the solution known as the solubility product (K).

$$A_xB_y \leftrightarrow xA^{y+} + yB^{x-} \qquad (2.1)$$

In this reaction, the ionic product is given by:

$$K = [A]^x[B]^y = Constant \qquad (2.2)$$

The chemical balance is reached if this expression is fulfilled; accordingly the precipitation occurs when this product is exceeded. However, this precipitation is usually massive and the solid formed does not grow in a defined, homogeneous pattern. To achieve a good deposition by a controlled ion by ion reaction, spontaneous precipitations must be avoided. This can be attained whether a formation of stable complex compound from metal ions is induced. This compound will provide a determined number of metal ions in a controlled manner according to the equilibrium reaction:

$$M\,(L)^{Z+} \leftrightarrow M^{Z+} + L \qquad (2.3)$$

Where M represents an atom of the cation element, Z is its valence and L the complexing agent. In this case, the concentration of free metal ions in the solution at a constant temperature is given by the following equation [20, 21]:

$$\frac{\left[M^{Z+}\right][L]}{\left[M(A)^{Z+}\right]} = K_{SP} \qquad (2.4)$$

Where $K_{SP,}$ is the instability constant of the ion complex.

2.3.2 DEPOSITION OF CdS BY CBD

In this work, CdS thin films were prepared by the decomposition of thiourea as a sulfur source in an alkaline solution of cadmium salts according to the reaction (1.11) [22-26]. With the adsorption of thiourea, the dihydroxocadmium adsorbed species forms a metastable complex as per the equation

$$[Cd(OH)_2]_{ads} + SC(NH_2)_2 \rightarrow [Cd(OH)_2\ SC(NH_2)_2]^{2+}_{ads} \qquad (2.5)$$

The metastable complex decomposes and CdS is formed according to the equation

$$[Cd(OH)_2]SC(NH_2)_2]^{2+}_{ads} \rightarrow CdS + CN_2H_2 + 2H_2O \qquad (2.6)$$

Being a thermodynamic mechanism of crystal growth in a solution, the supersaturation ratio for the formation of a solid CdS phase in the aqueous medium is defined as:

$$S = \left(\frac{([Cd^{2+}] \cdot [S^{2-}])}{K_{SP}} \right)^{\frac{1}{2}} = \frac{K}{[NH_3]^2} \qquad (2.7)$$

K is considered constant in the dilute solution of $Cd(NH_3)_4$ and thiourea, so the supersaturation ratio S strongly depends on the complexing agent (ammonia) concentration

[27]. At room temperature, cadmium sulfide may crystallize either in the zinc blende or wurtzite structures.

2.2.3 MICROWAVE-ASSITED CHEMICAL BATH DEPOSITION

It was found that the CBD method was somehow time-consuming, in which the required reaction time is as long as several hours. Therefore, a more rapid and efficient method was required to promote the deposition of CdS.

Microwave heating is a quite fast, simple and efficient method to prepare inorganic materials. The exact nature of microwave interaction with reactants during the synthesis of materials is somewhat unclear and speculative. However, energy transfer from microwaves to the material is believed to occur either through resonance or relaxation [28]. Electric dipoles present in such materials respond to the applied electric field. This constant reorientation creates friction and collisions between molecules, which subsequently generates heat. That is to say, this heating mechanism is realized directly from the molecules of the materials. Compared with conventional bathing heating, which is realized mainly by heat conduction, microwave heating is more efficient and rapid. In this thesis, CdS films were grown by microwave-assisted chemical bath deposition (MA-CBD) setup show in figure 2.3, which takes advantage of both CBD and microwave heating.

Figure 2.3 Microwave setup, temperature control is incorporated to the microwave unit to keep a constant temperature of the chemical bath.

2.3.4 MA-CBD SET UP

For the CdS thin films synthesis, 100 ml of the chemical bath is formed by an aqueous solution containing the following reactants in the specified molar concentrations: 0.1M cadmium nitrate ($Cd(NO_3)_2$) as cadmium source, 1M sodium citrate ($Na_3C_6H_5O_7$) as buffer, 1M thiourea ($SC(NH_2)_2$) as sulfur source, and 30% of ammonium hydroxide (NH_4OH). For solutions contained doping elements, the doping sources added to the reactants were: 0.1M ammonium chloride (NH_4Cl) as chlorine source, 0.1M boric acid (H_3BO_3) as boron source and 0.1M sodium chloride (NaCl) as sodium source. Commercial glass slides were used as substrates, which were cleaned in propanol, ethanol and methanol ultrasonically, then etched in a 5% hydrofluoric acid (HF) solution and finally washed again ultrasonically with methanol. For the deposition, the cleaned substrates were mounted vertically using a Teflon holder in a closed vessel. The temperature during the deposition process was maintained at 70 °C. All the solutions used for the deposition were clear solutions without precipitation. The bath solution was held at rest without stirring. The microwave irradiation time were 60, 90, 120, 150 and 180 seconds giving a total deposition time of 10, 15, 20, 25 and 30 minutes respectively giving various thicknesses of CdS films. After the deposition, the CdS films were ultrasonically washed with methanol to remove the loosely adhered CdS particles on the film and finally dried in air. The resulted transparent films presented a pale yellow color with a bright surface and high adherence to the substrates. The as-deposited films were then annealed in a nitrogen atmosphere at different temperatures (200, 250, 300, 350 and 400 ºC). The annealing time was maintained as 1 hour for all the films.

2.4 SUBSTRATE CLEANING

The quality of the surface is the most important requirement of a substrate since here is where the film-substrate interaction occurs. Also, the substrate should be chemically stable and amenable for high temperature pre-deposition treatments. No substrate will be suitable for all applications, and hence soda lime glass and stainless steel were chosen as substrates for this investigation.

The film adhesion is strongly dependent on the chemical nature, cleanliness and microscopic topography of the substrate surface. Better results are obtained at higher values of (i) kinetic energy of the incident species, (ii) adsorption energy of the deposit and (iii) initial nucleation density. Presence of contaminants on the substrate surface may increase of decrease the adhesion depending on whether the adsorption energy is increased or decreased respectively.

The substrate cleanliness is a prerequisite for the preparation of films with reproducible properties, and plays a vital role in the film growth and adhesion. An appropriate cleaning technique depends on the nature of the substrate, type of contaminants, and degree of cleanliness required. Cleaning requires that bonds are broken between contaminant molecules as well as between the contaminant and the substrate without any physical damage to the substrate. This may be accomplished by chemical means such as solvent cleaning. Suitable reagents like aqueous solutions of acids and alkalis as well as organic solvents, such as alcohols and ketones are used in solvent cleaning processes. To increase the rate of contaminant removal, solvent heating or ultrasonic agitation are commonly employed.

In the present investigation, each one of the substrates used followed two: first, a degreasing method for the removal of greasy substances, and then a piranha etch [29], used to clean organic residues off substrates as well as hydroxylate most surfaces (adding of OH groups), which makes them extremely adhesive to the films.

Degreasing method:

1. Commercial glass slides were dipped in a soap solution for 20 minutes with ultrasonic agitation for the removal of grease and other oily materials.
2. Then, they were washed meticulously with running distilled water.
3. Next, they were subjected to ultrasonic agitation for about 20 minutes in ethylic alcohol.
4. Again, they were washed in the running distilled water.

5. Afterwards, they were dipped in acetone for 20 minutes with ultrasonic agitation.
6. Finally, they were washed again in running distilled water.

Piranha etch:

After the degreasing method, the substrates were dipped in a mixture of 3:1 concentrated sulfuric acid (H_2SO_4) to hydrogen peroxide (H_2O_2) for 30 minutes. Finally the glass substrates were dried with nitrogen.

2.5 CHARACTERIZATION TECHNIQUES

The microstructure of thin films is directly influenced by the type of substrate used and by the deposition conditions prevailing during the film formation, such as substrate temperature, deposition rate, etc. Several techniques are available for the analysis of the structure, examples being X-ray diffraction (XRD), Scanning electron microscopy (SEM), Transmission electron microscopy (TEM), Atomic force microscopy (AFM), etc.

2.5.1 X-RAY DIFFRACTION TECHNIQUE

An X-ray diffractometer essentially consists of three parts: a basic diffraction unit, a counter goniometer and an electronic circuit panel with an automatic recorder. The diffraction angles and intensity of the result lines can be measured with great accuracy. A schematic diagram of an XRD measurement is illustrated in Figure 2.4.

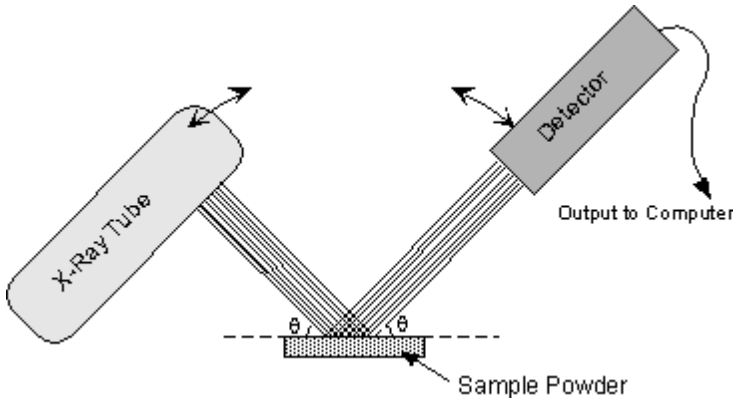

Figure 2.4 Schematic diagram giving details regarding the formation of X-ray diffraction pattern and focussing.

The foundation of XRD is the Bragg's law, which describes the conditions for constructive interference of X-rays scattered from the atomic planes of a crystal. The condition for constructive interference is:

$$2d\sin\theta = n\lambda \qquad (2.8)$$

Where λ is the wavelength of the X-rays, d is the lattice spacing, n is the order of diffraction and θ is the glancing angle of the X-rays. The factor d is related to the (hkl) indices of the atomic planes and the dimension of the unit cells. It is therefore seen that the direction of the diffracted X-rays is solely determined by the structure and size of the unit cell.

In the present work, the crystallite sizes (D) were calculated using the Scherrer formula [30]:

$$D = \frac{k\lambda_X}{\beta Cos\,\theta} \qquad (2.9)$$

Where D is the grain size, k is the Scherrer constant (0.94), λ_x is the wavelength of the X-ray used, β is the full width at half maximum (FWHM) and θ is the Bragg angle.

The strain (ε) was calculated from the slope of the $\beta cos\theta$ versus $sin\theta$ plot using the relation:

$$\beta = \frac{\lambda}{D\cos\theta} - \varepsilon\tan\theta \qquad (2.10)$$

The dislocation density and the number of crystallites per surface area unit have been determined by the following formulas [31]:

$$\delta = \frac{1}{D^2} \qquad (2.11)$$

$$N = \frac{t}{D^3} \qquad (2.12)$$

Where δ is the dislocation density, N the number of crystallites per surface are unit and t the thickness of the film.

The lattice parameter a for the cubic structure was evaluated from the equation [32]:

$$a = d\sqrt{\left(h^2 + k^2 + l^2\right)} \qquad (2.13)$$

And for the hexagonal structure, the lattice parameters a and c were evaluated from the equation [33]

$$\frac{1}{d^2} = \frac{4}{3}\frac{h \ + hk^2 + k^2}{a^2} + \frac{l^2}{c^2} \qquad (2.14)$$

In the present investigation, the structure of the films was analyzed using a Grazing Incidence X-ray diffractometer (Rigaku D-Max 2000, using Cu-Kα radiation with λ = 1.5406 Å). Measurements were made for 2θ values between 20-70° in steps of 0.03° with a count time of 5 s and a grazing angle equal to 1.5º.

2.5.2 COMPOSITIONAL ANALYSIS

Composition is one of the most important parameters in thin film characterization since compound materials dissociate during deposition due to their different melting points and vapor pressures.

2.5.2.1 ENERGY DISPERSIVE ANALYSIS USING X-RAYS

Energy dispersive X-ray spectrometers help in determining the elemental contents of a material in a very accurate manner. In this technique, a core level electron of a surface atom is removed by an impinging electron or an X-ray photon. The excited atom decays to a lower energy state through an electronic rearrangement in which an additional electron from a higher level is knocked out leaving the atom in a doubly ionized state. The energy

difference between these two states is given to the ejected electron, which will have a kinetic energy characteristic of the atom. In order to produce characteristic X-rays from an element it is necessary to apply a suitable critical excitation potential (E_g=17.5 KeV for K radiation in the case of molybdenum). Usually the EDAX system is coupled to a SEM.

2.5.2.2 Secondary ion mass spectrometry (SIMS)

SIMS is a technique to analyze the composition of solid surfaces and thin films by sputtering the surface of the specimen with a focused primary ion beam and collecting and analyzing ejected secondary ions. In this work, an ion microscope-microprobe ims-6f CAMECA (fig. 2.5) was used for SIMS measurements. A focused primary ion beam performs the ion sputtering of the sample surface. Secondary ions, both positive and negative, are collected by an electron optical system, and they are analysed with an energy and mass analyser (magnetic sector) and registered with a detector.

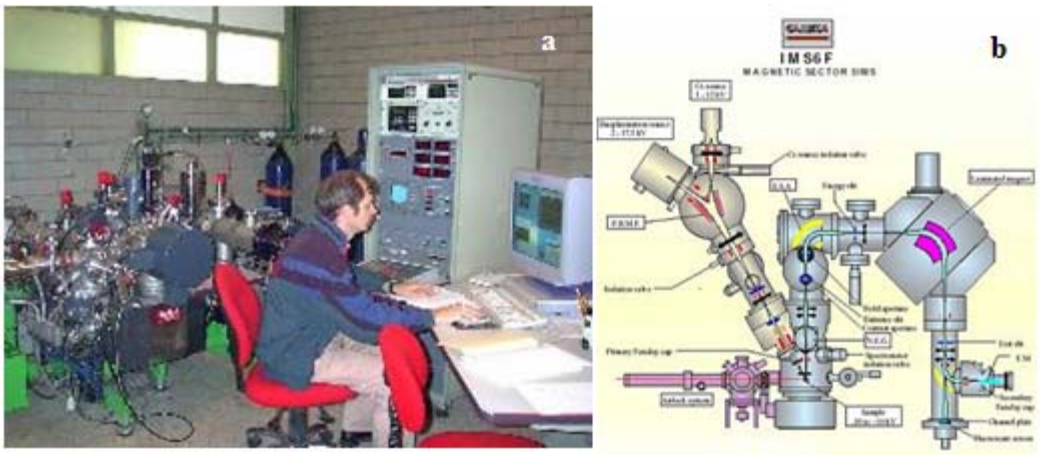

Figure 2.5 SIMS mod. ims-6f CAMECA, image a) and diagram b), Electric Engineer department-SEES CINVESTAV-IPN

2.5.3 SURFACE ANALYSIS

2.5.3.1 SCANNING ELECTRON MICROSCOPY (SEM)

SEM is a useful and popular technique for the direct observation of surfaces, employed to predict the growth mechanisms leading to the reminiscent structures. In a SEM analysis, the areas or micro-volumes to be examined are irradiated with a fine electron beam produced by the electron gun and focussed by electron lenses. The scanning coils

deflect this beam and sweep it over the film surface. A cathode ray tube is scanned synchronously with the electron beam. The brightness of the display tube is modulated by the signal which arises from the interactions of the beam with the film surface. The strength of this signal is thus translated into image contrast.

The types of signals produced when the electron beam impinges on the specimen surface include secondary electrons, Auger electrons, characteristic X-rays and photons of various energies. These signals are obtained from specific emission volumes within the samples, which ultimately determine surface topography, crystallography, composition, etc.

In the present work, the surface of the thin films was examined by using a Stereoscan 440 microscope. The equipment has a maximum magnification of 1:80,000 with resolution of 60 Ax. Since the sample analyzed is not electrically conducting, the sample surface is coated with a very thin gold layer to provide a conducting surface.

2.5.3.2 ATOMIC FORCE MICROSCOPY

The Atomic force microscope (AFM) is a very high-resolution type of scanning probe microscope, with demonstrated resolution of fractions of a nanometer, more than 1000 times better than the optical diffraction limit. The AFM is one of the foremost tools for imaging, measuring and manipulating matter at the nanoscale level. Piezoelectric elements that facilitate tiny but accurate and precise movements on (electronic) command are what permit the very precise scanning. Atomic Force Microscopy (AFM) analysis of the thin films was performed using Veeco Instruments Multimode SPM in the tapping mode with a 10 μm piezoelectric scanner at Scan Speed of 0.7 Hz.

2.5.4 OPTICAL PROPERTIES

The development of techniques for the optical characterization of solid films has greatly contributed to the phenomenal growth of diverse scientific, technological and industrial applications. Thin films are currently being used in a wide variety of optical devices such as mirror coatings, interference filters, antireflection coatings, absorption filters, optical and thermal detectors, etc. [34-38].

Optical characteristics of thin films are strongly influenced by their related deposition method and its process parameters. Optical films are primarily characterized by their absorption/transmittance and refractive index. An absorption/transmittance versus wavelength plot can be divided basically into three regions (1) ultraviolet (UV), (2) Visible and near infrared (NIR), and (3) infrared (IR) and far infrared (FIR). The desired region of high absorption/transmittance is located in the second region and it strongly depends on the material purity and stoichiometry. In region 1, the absorption depends on the electronic structure of the material, while in region 3 it depends on lattice vibrations or, in the case of semiconductors, on free carrier absorption [39].

2.5.4.1 ABSORPTION AND BAND GAP

Optical photons incident on any material may be reflected, transmitted or absorbed. The absorption of light in a semiconductor can lead to:

1. Photoionisation of semiconductor atoms: This is the excitation of valence electrons to the conduction band. The energy required must be greater or equal to the band gap.
2. Photoionisation of impurity atoms: This leads to the transition of an electron from the donor level to the conduction band or from the valence band to the acceptor level.
3. Excitation of electrons from the valence band to an imperfection level.
4. Formation of excitons.
5. Excitation of free carriers to a higher energy state in the same band.
6. Excitation or absorption of phonons.

Of all these absorption processes the first three directly give rise to photoconductivity. The optical absorption and transmittance studies are useful for the identification of band gap energies, impurity states, refractive index, extinction coefficient, etc. The optical absorption spectra of semiconductors generally exhibit a sharp rise at a certain value of the incident photon energy, which can be attributed to the excitation of electrons from the valence band to the conduction band. In optoelectronic applications of

thin films, optical absorption studies play an important role giving an insight into the nature of transitions, either direct or indirect. The absorption coefficient α can be calculated using the relation [40]

$$\alpha = \frac{2.303A}{t} \qquad (2.15)$$

Where A is the absorbance value at a particular wavelength and t is the thickness of the semiconductor film. Similarly the absorption coefficient α can be estimated from the optical transmittance spectra using the relation:

$$\alpha = \frac{2.303\log\left(\frac{1}{T}\right)}{t}, \qquad (2.16)$$

Where T is the transmittance.

The absorption of radiation that gives rise to transition of electrons between the valence and conduction bands is of two types,

a) Direct transition: The necessary condition for a direct transition to take place is that in the excitation process no change in the k-value of the electron should occur. The following dependencies are observed during this transition:

$\alpha \rightarrow (E_v - E_i)^{1/2}$ for allowed transitions

$\alpha \rightarrow (E_v - E_i)^{3/2}$ for forbidden transitions

Where α is the absorption coefficient, E_v is the energy of the top of the valence band and E_i is the energy of the initial state from which the transition is made.

The band gap values for direct allowed transitions can be calculated by plotting $(\alpha hv)^2$ versus $E(eV)$ and taking the slope of the graph at the beginning of the band-to-band absorption. In these formulas, h is the Planck constant and v the wave frequency.

b) Indirect transition: The transition involving a change in the crystal momentum is termed as an indirect transition. In this case, either absorption of both a photon and a phonon or the absorption of the first and the emission of the latter take place [41, 42]. The following dependencies are observed during this indirect excitation:

$\alpha \rightarrow (E_v - E_i)^2$ for allowed transitions

$\alpha \rightarrow (E_v - E_i)^3$ for forbidden transitions

The band gap values for indirect excitation can be calculated by plotting $(\alpha hv)^{1/2}$ versus $E(eV)$ and taking the slope of the graph at the beginning of band-to-band absorption.

2.5.4.2 EXTINCTION COEFFICIENT AND REFRACTIVE INDEX

The refractive index of thin films often differs from that of the material in bulk form. At optical frequencies, this value is mainly determined by the polarizability of the valence electrons. In compounds, the type of bonding also influences the index.

The analysis of the wavelength dependency on the refractive index n and the extinction coefficient k is of considerable interest due to the possibility of optoelectronic applications. These optical parameters can be calculated from the equations corresponding to the propagation of electromagnetic waves through the layers of plane-parallel faces, consisting of an absorbing thin semiconductor film and a transparent glass substrate. The extinction coefficient and the refractive index [43] can be evaluated from the relations:

$$\alpha = \frac{4\pi k}{\lambda} \qquad (2.17)$$

$$T = \frac{n_2}{n_0} \frac{(1+\delta_1)^2 (1+\delta_2)^2}{1+(\delta_1^2 \delta_2^2)+2\delta_1\delta_2 \cos 2\Gamma} \qquad (2.18)$$

Where

$$\delta_1 = \frac{n_0^2 + n_1^2}{(n_0 + n_1)^2},\ \delta_2 = \frac{n_1^2 - n_2^2}{(n_1 + n_2)^2},\ \text{and}\ \Gamma = \frac{2\pi n_1 t}{\lambda}$$

Where λ is the wavelength of the incident radiation, and n_0, n_1, n_2 are the refractive indices of air, film and glass, respectively. Substituting the experimental values for T, t, n_0 and n_2, the above equation can be solved for n_1 and k using an iteration method until the desired convergence is achieved.

In this work, the optical properties of the thin films were measured with a Shimadzu 3101 PC UV-VIS-NIR spectrophotometer in the wavelength range 250-2500 nm. The spectral distributions of transmittance were determined at room temperature. The substrate absorption was corrected by introducing an uncoated clean glass in the reference beam.

2.5.4.3 PHOTOLUMINESCENCE SPECTROSCOPY (PL)

Photoluminescence spectroscopy is a contactless, nondestructive method of probing the electronic structure of materials. Light is directed onto a sample, where it is absorbed and imparts excess energy into the material in a process called photo-excitation. One way this excess energy can be dissipated by the sample is through the emission of light, or luminescence. In the case of photo-excitation, this luminescence is called photoluminescence. The intensity and spectral content of this photoluminescence is a direct measure of various important material properties. The PL studies were done between 10 K and room temperature, using a SPEX double monochromator.

2.5.5 ELECTRICAL PROPERTIES

The conduction mechanism can be understood from the AC conductivity studies of the films with a Metal-Semiconductor-Metal (MSM) structure as it is illustrated in figure 2.6 [44, 45].

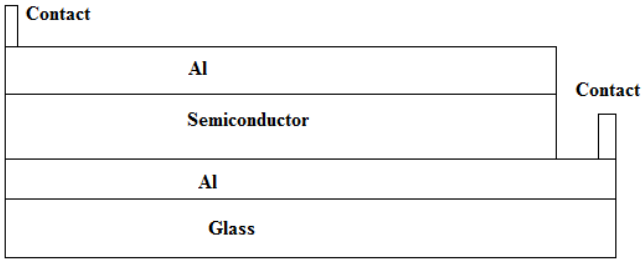

Figure 2.6 Metal (MSM) structure for electrical properties

The number of electrons of other charge carriers available for conduction in semiconductors can be assumed to depend on the bonding of atoms and will be reflected in conductivity, which depends on their mobility as well as temperature. The general mechanism is complex and affected by factors such as thermal vibration of atoms, presence of defects and impurities in the films. In a semiconductor, the presence of suitable impurities, defects, disorders, etc., create energy states in the forbidden gap as a result of which there may be a large change in their electrical conductivities with thermal excitation. This possibility of varying the electrical properties of semiconductors using impurities has made semiconductors as the only choice for electronic devices. The most common technique for determining the density of the carriers is the Hall effect.

2.5.5.1 HALL EFFECT

When a current-carrying semiconductor is kept in a magnetic field, charge carriers experience a force in a direction perpendicular to both magnetic and current fields. This is called the Hall Effect in semiconductors. When there is not a magnetic field, the charges follow a straight line path. However, when a perpendicular magnetic field is applied, their path is curved so that moving charges accumulate on one face of the material. This leaves equal and opposite charges exposed on the other face, where there is a scarcity of mobile charges. The separation of charge establishes an electric field that opposes the migration of further charge, so a steady electrical potential builds up as long as the current is flowing. The Hall coefficient is defined as:

$$R_H = \frac{E_y}{J_x B} = \frac{V_H}{I\left(\frac{B}{d}\right)} = -\frac{1}{ne} \qquad (2.19)$$

Where I is the current across the plate, B is the magnetic flux density, d is the depth of the plate, e is the electron charge, V_H is the Hall voltage, and n is the charge carrier density of the carrier electrons.

The simple formula for the Hall coefficient given above becomes more complex in semiconductors where the carriers are generally both electrons and holes, which may be

present in different concentrations and have different mobilities. For moderate magnetic fields the Hall coefficient is:

$$R_H = \frac{-n\mu_e^2 + p\mu_h^2}{e(n\mu_e + p\mu_h)^2} \qquad (2.20)$$

Where n is the electron concentration, p is the hole concentration, μ_e is the electron mobility, μ_h is the hole mobility and e is the electronic charge.

For large applied fields and a single carrier type, the following simpler expression can be used:

$$R_H = \frac{1}{(n-p)e} \qquad (2.21)$$

2.5.5.2 PHOTOSENSITIVITY

The concept of photosensitivity may be defined in several ways. One way is to define a particular quantity, the specific sensitivity *SS*, which is the change in conductivity caused by excitation divided by the excitation intensity.

Excitation intensity is the power absorbed per unit volume ($P/l \cdot b \cdot t$), where P is the absorbed power. Thus the specific sensitivity is given by:

$$SS = \frac{\delta\sigma lbt}{P} = \frac{\delta_i}{V}\frac{l}{bt}\frac{lbt}{P} = \frac{\delta_i l^2}{VP} \qquad (2.22)$$

Where δ_i is the photocurrent, σ is the conductivity, V is the applied voltage, P is the absorbed radiation power, l is the length, b is the width, and t is the thickness of the film. Here, *SS* is expressed in mho-cm^2 per watt. The specific sensitivity is an intrinsic property of the material, which is independent of applied voltage and light intensity if the photoconductivity varies linearly with voltage and light intensity.

Another important quantity, the relative photosensitivity *ps*, is defined as the ratio of the change in light conductivity to the dark conductivity.

$$ps = \frac{\sigma_L - \sigma_D}{\sigma_D} \qquad (2.23)$$

Where σ_L is the light conductivity and σ_D is the dark conductivity. In both cases $\sigma = I / R \cdot A$, where R is the resistance, I is the length and A the area of cross section of the photoconductor. Substituting this in the above equation gives:

$$ps = \frac{R_D - R_L}{R_L} \qquad (2.24)$$

$$ps = \frac{R_D}{R_L}, \text{ if } R_D >> R_L \qquad (2.25)$$

2.5.6 RAMAN SPECTROSCOPY

Raman spectroscopy is a spectroscopic technique used to study vibrational, rotational, and other low-frequency modes in a system. It relies on inelastic scattering, or Raman scattering, of monochromatic light, usually from a laser in the visible, near infrared, or near ultraviolet range. The laser light interacts with phonons or other excitations in the system, resulting in the energy of the laser photons being shifted up or down. The shift in energy gives information about the phonon modes in the system. Infrared spectroscopy yields similar, but complementary, information. The Raman dispersion studies were done in a Horiba–Jobin Yvon equipment, model LabRAM HR800 with a resolution of 1 cm^{-1}.

2.6 CONCLUSIONS

Sputtering and chemical bath techniques offer homogeneous and good quality thin films. To achieve this it is important to have a precise control of the parameters of deposition, by example for the preparation of CIS films by Sputtering is crucial to identify the potential coupled with the distance and temperature of deposition for films that meet the

stoichiometry. The CIS and CdS films are subject to a physical treatment with the aim of improving its structural, optical and electrical properties. This treatment is an annealing at high temperature in nitrogen atmosphere.

In this chapter, the experimental details and basic theory behind the experiments and characterizations carried out has been explained. The concepts analyzed in this chapter will help to understand the structural, optical, electrical and photoconductive properties of the semiconductor materials CIS and CdS prepared for this work.

REFERENCES

[1] A. Goswami, Thin Film Fundamentals, New Age International (P) Ltd, N.Y., 2003

[2] L. Holland, Vacuum Deposition of Thin Films, John Wiley, New York, (1956)

[3] R. Glang, Handbook of Thin Film Technology, Edited by L. I. Maissel and R. Glang, Mc Graw-Hill Publications, New York, 1970

[4] K. L. Chopra, S. R. Das, Thin Film Solar Cells, Plenum Press, New York and London, 1983

[5] W. R. Grove, The correlation of Physical Forces, Kessinger Publishing, N. J., 2006

[6] L. I. Maissel, Physics of Thin Films, Edited by G. Hass and R. E. Thun, Academic Press, New York 1966.

[7] L. I. Maissel, Handbook of Thin Film Technology, Edited by L. I. Maissel and R. Glang, McGraw-Hill Publications, New York, 1970

[8] Pliskin, W. A., E. E. Conrad, Electrochemical technology, 2 (1964) 196

[9] G. K. Wehner, Physical Review, 93 (1954) 633

[10] G. K. Wehner, Physical Review, 114 (1959) 1270

[11] G. K. Wehner, Journal of Applied Physics, 31 (1960) 1392

[12] Brennemann, A. E., L. V. Gregor, Journal of Electrochemistry, 112 (1965) 1194

[13] G. S. Anderson, Journal of Applied Physics, 33 (1962) 2017

[14] S. C. Brown, Introduction to Electrical Discharge in Gases, John Wiley, New York, 1963

[15] H. S. Butler, G. S. Kino, Physics of Fluids, 6 (1963) 1346

[16] P. D. Davidse, SCP Solid State Technology, 12 (1966) 36

[17] Guozhong Cao, Nanostructures and Nanomaterials, Imperial College Press, USA 2004

[18] M. Ohring, The Materials Science of Thin Films, Academic Press, San Diego, CA, 1992

[19] Jorge G. Ibañez, Flora Gomez, Ivonne Konik, Diane E. Lozano, Journal of Chemical Education, 74 (1997) 1205

[20] O Savadogo, Solar Energy Materials and Solar Cells, 52 (1998) 361

[21] Victor Manuel García S., La revista Solar, 11 (2001) 27

[22] E. Çetinörgü, C. Gümüş, R. Esen Thin Solid Films, 515 (2006) 1688-1693

[23] Joel Pantoja Enríquez, Xavier Mathew, Solar Energy Materials and Solar Cells, 76 (2003) 313-322

[24] P.J. Sebastian, H. Hu, Advanced Materials for Optical Electronics, 4 (1994) 407

[25] C. Guillén, M. A. Martínez, J. Herrero, Thin Solid Films, 335 (1998) 37

[26] N. G. Dhere, D. L. Waterhouse, K. B. Sundaram, O. Melendez, N. R. Parikh, B. Patnaik, J. Mater. Sci. Mater. Electron. 6 (1995) 52

[27] Fuyi Chen, Wanqi Jie, Xiaomei Cai, Thin Solid Films, 516 (2008) 2823-2828

[28] Ran Zhai, ShuBo Wang, HaiYan Xu, Hao Wang, Hui Yan, Materials Letters 59 (2005) 1497-1501

[29] K. J. Seu, A. P. Pandey, F. Haque, E. A. Proctor, A. E. Ribbe, J. S. Hovis Biophysical 92 (2007) 2445-2450

[30] Donald R. Askeland, Science and Engineering of Materials, third edition, Wadsworth Publishing Company, Boston 1994, p. 68

[31] B.D. Cullity, Elements of X-ray Diffraction, Addison-Wesley, Reading, MA, 1972, p. 102

[32] G. B. Williamson, R. C. Smallman, Phil. Mag. 1 (1956) 34

[33] H. P. Kulg, L. E. Alexander, X-ray Diffraction Procedures, Wiley, New York, 1974

[34] P. Galarneau, C. Malouin, A. Sngh, R. A. Lessard, Appl. Opt., 27 (1988) 1491

[35] J. A. Aguilera, J. Aguilera, P. Baumeister, A. Bloom, D. Coursen, J. A. Dobrowolski, F. T. Goldstein, D. E. Gaustafson, R. A. Kemp, Appl. Opt., 27 (1988) 2832

[36] L. R. Gilbert, R. Messier, R. Roy, Thin Solid Films, 54 (1978) 149

[37] H. F. Taylor, A. Yariv, Proceedings IEEE, 62 (1974)1044

[38] L. Kuhn, M. L. Dakrs, P. F. Heidrich, R. A. Lessard, Appl. Phys. Lett., 17 (1971) 1564

[39] H. K. Pulker Applied Optics, 18 (1979) 1569

[40] S. Velumani, Xavier Mathew, P. J. Sebastian, Sa. K. Narayandass, D. Mangalaraj, Solar Energy Materials and Solar Cells, 76 (2003) 347-358

[41] Hall, Bardeen, Blatt, Physics Review, 95 (1954)51

[42] Bardeen, Blatt, Hall, Photoconductivity conference, Atlantic city, (1954), Willey (1956), 194

[43] S. Ahmed, E. E. Khawaja, Thin Solid Films, 112 (1984) 16

[44] N. F. Mott, Phil. Mag., 19(1969)836

[45] M. Pollack, Phil. Mag., 23 (1971)519

CHAPTER III Characterization of CIS absorber layer

3.1 INTRODUCTION

In this chapter the results of the structural, morphology, composition, electrical and optical characterization of the sputtered CIS thin films, as deposited and annealed to high temperature will be discussed.

Structural characterization of thin films is the most important characterization because; all the properties of thin films are governed and controlled by their structure. The knowledge on structural formation of thin films is an essential factor to understand its behaviour and to impart meaning to different physical properties, which are ultimately used for device applications. The electron exchange behavior at the photovoltaic junction is strongly affected by the structural configuration of the interface at the junction. Therefore, study of the thin film structural properties is one of the important factors for designing photovoltaic cells. Out of the various structural characterization techniques, X-ray diffraction technique has been found to be more successful due to its advantages; such as non-destructiveness, relative easiness and convenience. Moreover, large diffraction angles help in making accurate measurement of diffraction patterns representing the average crystalline lattice throughout the film due to increased penetration and simultaneous display of diffraction patterns from the film. In the present work, the structural properties of the thin films were measured using a Rigaku D-Max 2000 Grazing Incidence X-ray diffractometer, using Cu-Kα radiation with λ = 1.5406 Å.

There are several techniques and methods for understanding the surface topography of the films, for instance scanning electron microscopy, atomic force microscopy, interferometry, x-ray topography, etc. In the present investigation Stereoscan 440 scanning electron microscope has been used for morphological studies with a maximum magnification of 1:80,000 with resolution of 60 Ax. Elemental identification and composition can be studied by energy dispersive x-ray analysis, wavelength dispersive x-ray analysis, auger electron microscope, x-ray photoelectron spectroscopy, secondary ion mass spectrometry, electron prove microanalysis etc. In the present study energy dispersive

X-ray analysis (EDAX) attached to the scanning electron microscope has been employed to identify the chemical constituents in the films.

The knowledge of optical properties of solid films has widely contributed to the phenomenal growth of their applications in scientific, technological and industrial fields. In this thesis, optical properties of the thin films were measured with a Shimadzu 3101 PC UV-VIS-NIR spectrophotometer in the wavelength range 250-2500 nm.

The study of electrical properties is another important means of analyzing the conducting nature of semiconductor films. Electrical properties such as lifetime, mobility and diffusion length can be measured using ac conduction studies and Hall effect techniques. The equipments used in our analysis of electrical properties were DSP Lock-in Amplifier model SR 830 and an experimental arrangement for Hall effect consisting of Walker scientific gaussmetter d. c. power supply, magnetron and Keithley voltmeters.

3.2 COMPOSITION, STRUCTURE AND SURFACE ANALYSIS

The structural properties of CIS thin films prepared by different techniques have been reported by several workers [1-16]. X-ray diffraction studies carried out by De Silva *et al.* [1] on electrodeposited CIS thin films have indicated the presence of chalcopyrite phase for both annealed and indium diffused films, however they also reported the presence of sphalerite phase. Kim and Im [2] have reported that the optimum condition for fabricating single phase chalcopyrite CIS films is the sputter deposition of Cu and In metals in the range of sputtered molecularity (M)=Cu/In= 0.28 – 0.31. CIS by molecular beam deposition method have been prepared by Kim *et al* [3] and they found that in copper rich films (In/Cu<1) only the (112) diffraction line appeared to be strong, where as indium rich films (In/Cu>1) consisted of randomly oriented polycrystals. Mehdaoui *et al* [4] observed an increase in intensity of peaks in the x-ray diffractogram with increase of film thickness for CIS thin films prepared by thermal evaporation technique. They have estimated the crystallite size as 170 and 213 Å for films of thickness 175 and 230 nm respectively. X-ray diffraction studies carried out by Agilan *et al* [5] on CIS films grown by hot wall vacuum evaporation show that films grown at substrate temperature greater than 420° C are

polycrystalline single phase chalcopyrite. Haneman *et al* [6] have grown CIS films by flash evaporation technique on GaAs substrates and further studied by reflection high energy electron diffraction technique. They have reported that films grown at substrate temperature less than 570 K are polycrystalline. Above this temperature a gradual transition from polycrystalline to single crystalline state was observed. The composition of CIS films can be varied precisely by changing both the source and substrate temperatures, as reported by Kohiki *et al* [7]. They have obtained larger grain size for copper rich films (1-2 μm) than for the indium rich films (less than 0.7 μm) and the grain size of the near stoichiometric film was intermediate (0.5 – 1 μm). The intensity of the preferred (112) orientation was found to increase with the increase in Cu: In ratio and the copper rich films exhibited only (112) orientation. The lattice parameters have been reported as a= 5.78 Å and c=11.62 Å. CIS films deposited by two source vacuum evaporation $CuInSe_2$ and Se powders at a substrate temperature 200°C have been reported by Aren et al [8]. The films exhibited three peaks corresponding to (112), (220, 204) and (424) orientations, where (112) peak was observed to be very intense.

3.2.1 Results and discussion

The composition of CIS films used as absorbers in thin film solar cells is a topic of main importance since many cell properties are influenced by deviations form stoichiometry. Based on the defect chemistry model of ternary compounds proposed by Groenik and Janse [9] the deviations from stoichiometric composition can be described by two parameters Δm and Δs, which respectively determine the deviation from molecularity and stoichiometry.

$$\Delta m = \frac{[Cu]}{[In]} - 1 \qquad (3.1)$$

$$\Delta s = \frac{2[Se]}{[Cu]+3[In]} - 1 \qquad (3.2)$$

The meanings of deviations from zero for these parameters are described as follows:

1. $\Delta m > 0 \rightarrow$ Cu rich films

$\Delta m < 0 \rightarrow$ In rich films

2. $\Delta s > 0 \rightarrow$ excess of selenium
   $\Delta s < 0 \rightarrow$ selenium deficiency

The crystallinity and the grain size of CIS thin films increase with the substrate temperature, however at very high temperatures films showed a drop in Se content indicating evaporation of Se from the substrates. All our depositions in the present investigations were made at 400ºC, since this temperature was found to yield stoichiometric films and optimum for photovoltaic applications as reported by Shah *et al* [10-12]. The optimal distance between the target and the substrate was the first parameter to be analyzed due to the non-availability of much references. For the first six CIS films deposition, the parameters were set as follow: Power at 80 W based on references [13, 14] 2000nm thickness which is the most widely used in the absorber layer in photovoltaic cell [15] and varying the distance from 4 to 6.5 cm. The compositions of the deposited CIS thin films, determined using energy dispersive X-ray analysis, are shown in ternary graphs in figures 3.1. The stoichiometric point (Cu =25 atomic%, In =25 atomic% and Se =50 atomic%) has been marked with a circle as a reference. The compositions values of the films are reported in table 3.1.

Table 3.1 Composition of the sputtered CIS films deposited at a substrate temp of 400ºC, 80W Power, 2000 nm thickness and varying the distance from 4 to 6.5 cm

Distance (cm)	at%Cu	at%In	at%Se	Δm	Δs	% CIS
4	6.17	47.97	45.86	-0.87	-0.39	24.68
4.5	7.54	41.73	50.73	-0.82	-0.24	30.16
5	6.03	42.13	51.84	-0.86	-0.22	24.12
5.5	6.69	43.82	49.49	-0.85	-0.28	26.76
6	7.24	42.89	49.87	-0.83	-0.27	28.96
6.5	8.18	43.31	48.51	-0.81	-0.30	32.72

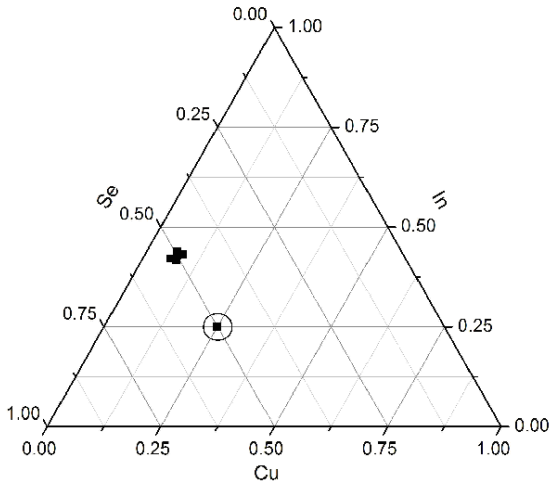

Figure 3.1 Ternary diagrams of composition results of CIS film deposited at a substrate temp of 400ºC, 80W Power, 2000 nm thickness and varying the distance from 4 to 6.5 cm

Table 3.1 shows that the films are copper deficit. The absence of elemental copper could be due to its high reactive state which is thought to be favored by broad atomic distribution of copper and indium within the entire mass of the alloy materials [16]. In order to improve the copper content, deposition of copper over the prepared films were performed by thermal evaporation and the evaporation time was varied from 1s to 15s at the rate of 35 Å/s. After the deposition, the films were annealed at 500°C for 15 minutes in order to incorporate copper into the CIS structure and also to improve the crystallinity [17]. The copper evaporation time that showed the best improvement in stoichiometry was 13 seconds and furthermore copper evaporation is not needed. Other important issue is that with annealing, a little amount of selenium got evaporated. The composition values of the copper incorporated CIS thin films are shown in ternary graph 3.2 and table 3.2.

Table 3.2 Composition of the sputtered CIS films deposited at a substrate temp of 400ºC, 80W Power, 2000 nm thickness and varying the substrate-target distance from 4 to 6.5 cm with 13s copper evaporation and 15 min annealed at 500ºC

Distance (cm)	at%Cu	at%In	at%Se	Δm	Δs	% CIS
4	11.14	42.08	46.78	-0.74	-0.32	44.56
4.5	29.9	30.59	39.51	-0.02	-0.35	79.02
5	18.1	39.08	42.82	-0.54	-0.37	72.4
5.5	16.86	36.71	46.43	-0.54	-0.27	67.44
6	24.54	34.32	41.14	-0.28	-0.35	79.46
6.5	33.04	27.23	39.73	0.21	-0.31	82.28

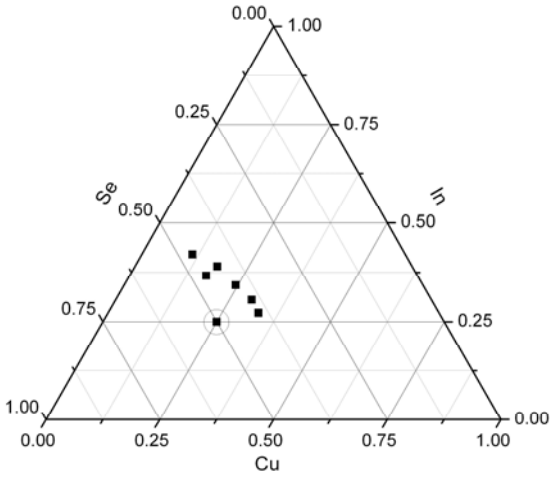

Figure 3.2 Ternary diagrams of composition results of CIS film deposited at a substrate temp of 400ºC, 80W Power, 2000 nm thickness and varying the distance from 4 to 6.5 cm with 13s copper evaporation and 15 min annealed at 500ºC

All the films are indium rich and seem to be selenium deficit. Indium rich CIS films are generally n-type material, never the less the material that most influent in the type of the material is selenium [18]. However the percentage of CIS in the films was improved from 32.72 to 82.28.

Once the optimal distance for obtaining higher-quality CIS films was fixed, the following step was to validate the deposition power to improve film quality. For the next deposition of CIS films, the parameters were set as follow: the power varying from 40 to 100 W, 2000 nm thickness, 6.5 cm distance, 13s copper evaporation and 15 min annealing at 500ºC. The composition values of the CIS films deposited varying the power are shown in the ternary graph in figure 3.2 and table 3.2

Table 3.3 Composition of the sputtered CIS films deposited at a substrate temp of 400ºC, varying power from 40 to 80W, 2000 nm thickness, 6.5 cm distance with 13s copper evaporation and 15 min annealed at 500ºC

Power (W)	at%Cu	at%In	at%Se	Δm	Δs	% CIS
40	16.27	40.18	43.55	-0.6	-0.36	65.08
60	17.53	27.24	55.23	-0.36	0.11	70.12
70	19.75	28.46	51.79	-0.31	-0.01	79
80	33.04	27.23	39.73	0.21	-0.31	82.28
90	24.54	35.86	39.6	-0.32	-0.40	79.2
100	25.93	33.48	40.59	-0.23	-0.36	81.18
110	24.7	34.09	41.21	-0.28	-0.35	82.42

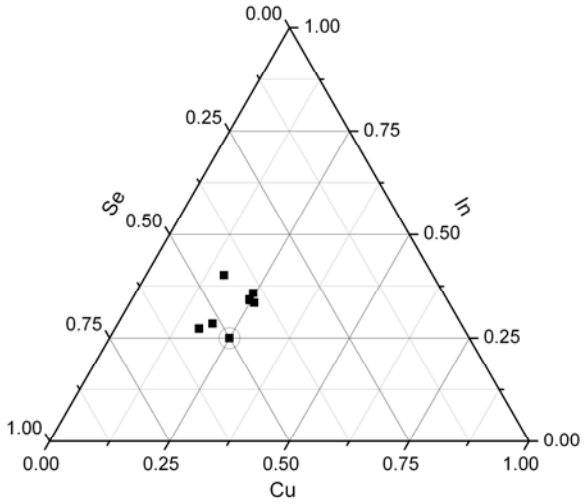

Figure 3.3 Composition of the sputtered CIS films deposited at a substrate temp of 400ºC, varying power from 40 to 80W, 2000 nm thickness, 6.5 cm distance with 13s copper evaporation and 15 min annealed at 500ºC

It is observed that the films with better stoichiometry were those deposited at 80 and 110 W, which is consistent with the literature that the power of 80 W produced good stoichiometry [13, 14]. Having optimized the power, since the thickness influences the properties of thin film; further depositions were made by varying the thickness from 1000 to 3000 nm, setting the power at 80W, distance at 6.5 cm, 13s copper evaporation and 15 min annealing at 500ºC.

Table 3.4 Composition of the sputtered CIS films deposited at a substrate temp of 400ºC, varying thickness from 1000 to 3000 nm, 80W power, 6.5 cm distance with 13s copper evaporation and 15 min annealed at 500ºC

Thickness (nm)	at%Cu	at%In	at%Se	Δm	Δs	% CIS
1000	24.15	31.77	44.08	-0.24	-0.26	88.16
1500	25.32	30.21	44.47	-0.16	-0.23	88.94
2000	33.04	27.23	39.73	0.21	-0.31	82.28
2500	22.66	28.13	49.21	-0.19	-0.09	90.64
3000	35.19	19.43	45.38	0.81	-0.03	90.76

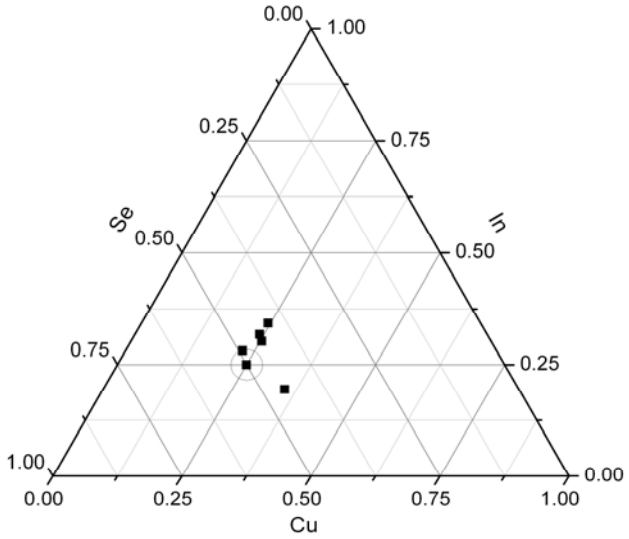

Figure 3.4 Ternary diagram of composition of the sputtered CIS films deposited at a substrate temp of 400ºC, varying thickness from 1000 to 3000 nm, 80W power, 6.5 cm distance with 13s copper evaporation and 15 min annealed at 500ºC

Figure 3.4 and Table 3.4 shows that through the process of r.f. sputtering, copper evaporation and annealing, it is possible to obtain CIS thin films with a composition close to stoichiometry (90.76%). By these analyses it can be concluded that the parameters that favor the stoichiometry are: Power at 80W, distance at 6.5 cm, 13 s of copper evaporation at 35 Å/s. Anneal of 500°C for 15 minutes.

The figure 3.5 shows the diffractograms of the CIS films deposited at different distance, 4.0, 4.5, 5.0, 5.5, 6.0 and 6.5 cm.

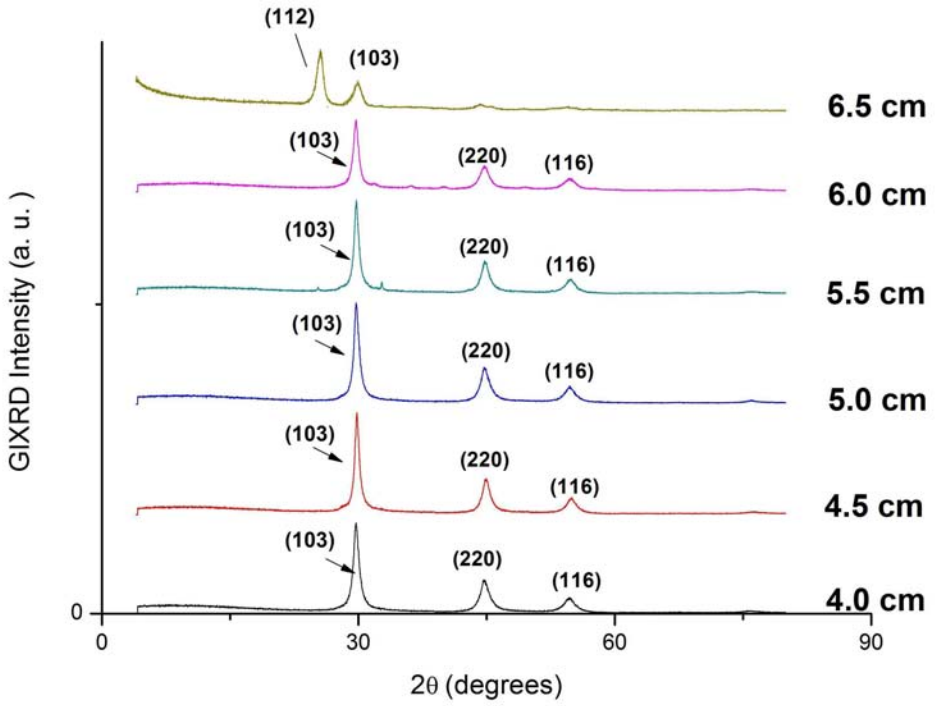

Figure 3.5 X-ray diffractogram of CIS films deposited at distances of 4.0, 4.5, 5.0, 5.5, 6.0 and 6.5 cm.

The films deposited at distance between 4 and 6 cm show the peaks corresponding to the (004), (220) and (116) orientation. Alternatively, the film deposited at 6.5 cm, shows the peaks (112) and (004). Composition analysis result shows that the deposited film at 6.5 cm has a composition of Cu=33.04 atomic%, In=27.23 atomic% and Se=39.73 atomic% with a Cu/In ratio = 1.21. This copper excess compared to the other five films composition (Cu/In ratio < 1.0) is probably the reason that the film has different orientation planes. Besides this fact there is no other relevant detail that can be seen in the graph. From the formulas presented in chapter II (eq. 2.08 to eq. 2.14) the structural parameter of the films deposited at different distances are presented in Table 3.5.

Table 3.5 Structural parameters of CIS films deposited at distances of 4.0, 4.5, 5.0, 5.5, 6.0 and 6.5 cm at 80 W.

Sample Distance (cm)	Observed (hkl) planes	Grain size (nm)	Dislocation density (δ) (10^{14} lines/m^2)	Numb. of crystallites/unit area ($10^{15}m^{-2}$)	Strain (ε) (10^{-3})	a (Å)		c (Å)		c/a Ratio
						Observed	ASTM	Observed	ASTM	
4	(004)(220) (116)	198	28	236	2	5.77	5.789	11.53	11.62	1.99
4.5	(004)(220) (116)	241	19	128	1	5.78		11.53		1.99
5	(004)(220) (116)	239	20	145	1	5.78		11.53		1.99
5.5	(004)(220) (116)	189	31	263	2	5.77		11.53		1.99
6	(004)(220) (116)	199	28	451	2	5.82		11.90		2.04
6.5	(112)(004)	198	28	236	2	5.62		12.42		2.21

The x-ray diffractograms of the CIS films deposited at power of 40, 60, 70, 80, 90, 100 and 110 W are shown in figure 3.6. The X-ray diffractograms of the films with power of 40 and 70 W show three peaks corresponding to (004) plane at 2θ = 29° 47', (220) at 2θ = 43° 58' and (301) plane at 2θ = 47° 56' which are characteristic of the chalcopyrite structure. Film deposited at 60 W shows the diffraction peaks corresponding to (112), (004), (220) and (301) orientations. Similar peaks for CIS films deposited by CSVT technique have been reported by Masse and Djessas [19]. Film deposited at 80 W shows two diffraction peaks corresponding to (112) plane at 2θ = 26° 43' and (004) plane at 2θ = 30° 30'. The film deposited at 90 W presents diffraction peaks corresponding to the (101), (112) and (004) orientations. The film deposited at 100 W shows a peak corresponding to the (112) plane and the films deposited at 110 W show three broadening peaks corresponding to the (112), (220) and (301) orientations.

From the graph 3.6 it is explicit that at lower power, the peak seems to be sharper, and at higher power, the peaks broadened. Therefore it can be inferred that as the power increases, the grain size reduces as seen in Table 3.6. Below 70 W, the preferred orientation was found to be along the plane (004) and above it the orientation changed to (112) plane or in the case of 90 W to (101).

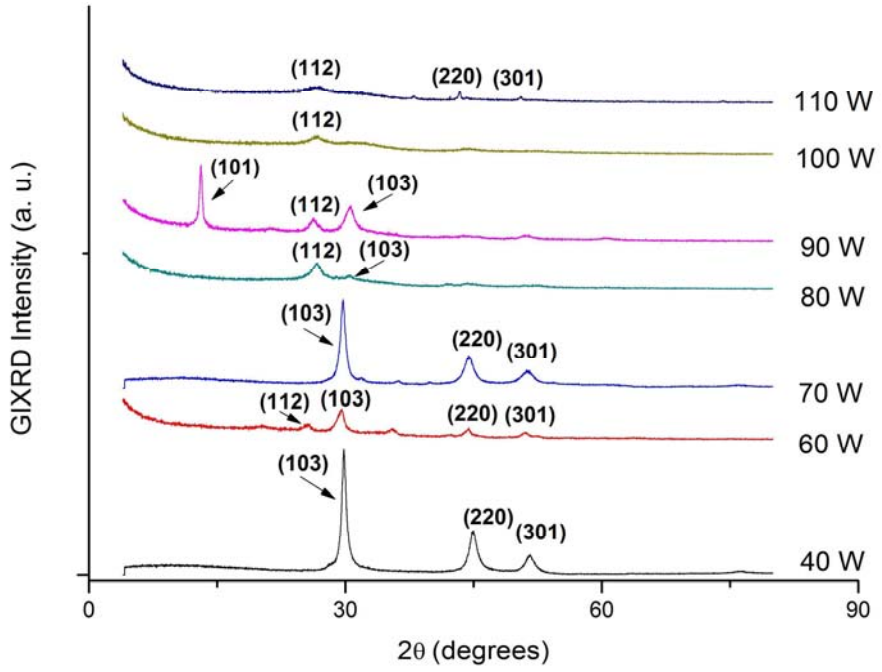

Figure 3.6 X-ray diffractograms of CIS films deposited at power of 40, 60, 70, 80, 90, 100 and 110 W

Table 3.6 Structural parameters of CIS films deposited at 40, 60, 70, 80, 90, 100 and 110 W at a distance substrate-target of 6.5 cm.

Sample Power (W)	Observed (hkl) planes	Grain size (nm)	Dislocation density (δ) (10^{14} lines/m^2)	Numb. of crystallites/unit area ($10^{15}m^{-2}$)	Strain (ε) (10^{-3})	a (Å)		c (Å)		c/a Ratio
						Observed	ASTM	Observed	ASTM	
40	(004)(220) (301)	241	19	128	1	5.78	5.789	11.53	11.62	1.99
60	(112)((004) (220)(301)	196	28	312	2	5.77		11.48		1.98
70	(004)(220) (301)	204	26	208	1	5.82		11.90		2.04
80	(112)(004)	198	28	236	2	5.62		12.42		2.21
90	(101)(112) (004)	287	32	435	2	5.83		11.91		2.04
100	(112)	121	112	2708	4					
110	(112)(220) (301)	73	187	5113	5	5.84		11.83		2.03

The x-ray diffractograms of the deposited CIS films of thicknesses 1000, 1500, 2000, 2500 and 3000 nm are shown in figure 3.7. The X-ray diffractogram of the film with 1000 nm thickness shows an intense peak that appears at 2θ = 26°43' which is associated to the (112) plane corresponding to the CIS phase. As the thickness increases, the peak starts

broadening and after the thickness of 2000 nm, the peak corresponding to the (004) plane at 2θ = 30° 30' emerges and its intensity increases as the film thickness increases due to the growth of the deposited material involved in the process, similar to other reports [20]. This indicates that below the thickness of 2000 nm, the preferential orientation is (112). This orientation is believed to be beneficial for CIS films to be employed for solar energy conversion [21]. Although above the thickness of 2000 nm, the orientation shifts from (112) to (004). This change in orientation can be attributed to the increase of strain energy as the thickness increases [22].

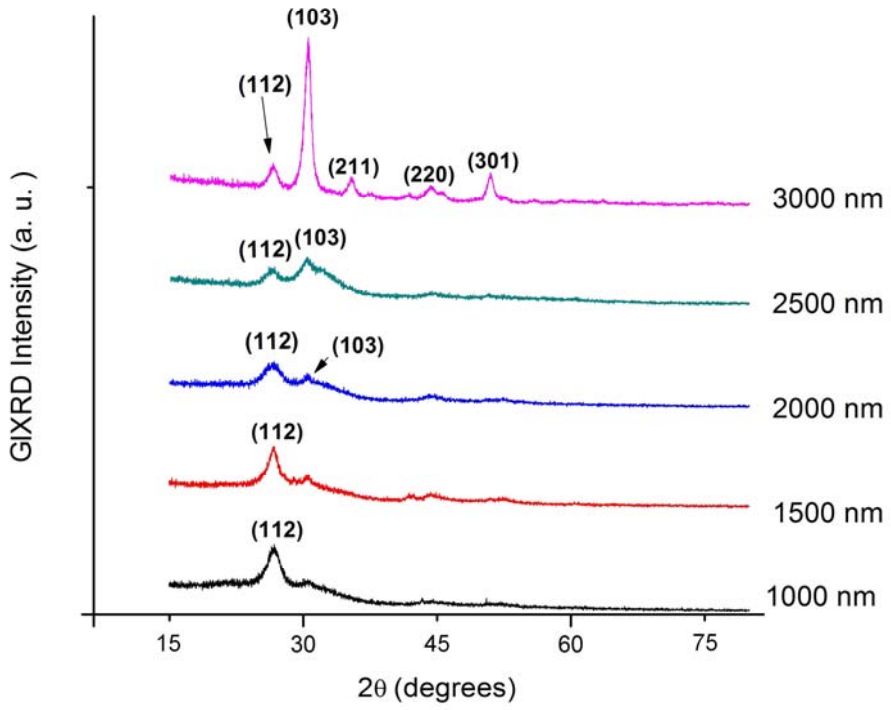

Figure 3.7 X-ray diffractograms of CIS films with thicknesses 1000, 1500, 2000, 2500 and 3000 nm.

When the strain is relatively high and there is high percentage of defects, the orientation of the film tends to change direction. The film with thickness 3000 nm exhibits characteristic peaks corresponding to chalcopyrite structure. The orientation of the planes in these films are, (112) at 2θ = 26° 39', (004) at 2θ = 30° 34', (211) at 2θ = 35° 26', (220) at

2θ = 43° 17' and (301) at 2θ = 47° 59'. The presence of the peak (112) in all the five films indicates that the CIS films exhibit a tetragonal chalcopyrite structure. Structural parameters of these films are given in Table 3.7. The lattice parameter values 'a' and 'c' of the CIS films of various thicknesses are in good agreement with International Centre for Diffraction Data (ICDD) (40-1487) and reported values [10, 11, 14].

Table 3.7 Structural parameters of CIS films prepared by r.f. sputter technique, incorporated with copper and annealed at 500°C

Sample thickness (nm)	Observed (hkl) planes	Grain size (nm)	Dislocation density (δ) (10^{14} lines/m^2)	Numb. of crystallites/unit area ($10^{15}m^{-2}$)	Strain (ε) (10^{-3})	a (Å)		c (Å)		c/a Ratio
						Observed	ASTM	Observed	ASTM	
1000 nm	(112)	116	74	639	3		5.789		11.62	
1500 nm	(112)	145	47	491	3					
2000 nm	(112)(004)	198	28	236	2	5.62		12.42		2.21
2500 nm	(112)(004)	174	33	380	2	5.60		12.44		2.22
3000 nm	(112)(004) (211)(220) (301)	199	28	451	2	5.78		11.60		2.01

The scanning electron micrograph of CIS films of thickness 1000 and 3000 nm are shown in figures 3.8 a) and b) respectively. The micrographs revealed that the deposited films are polycrystalline in nature. Similar results have been reported by Tverjanovich et al [23] for CIS films deposited by close-spaced vapour transport technique at a source temperature of 713 K. They have obtained a Cu/In ratio equal to 0.95 and In/(Cu+In) ratio equal to 1.29.

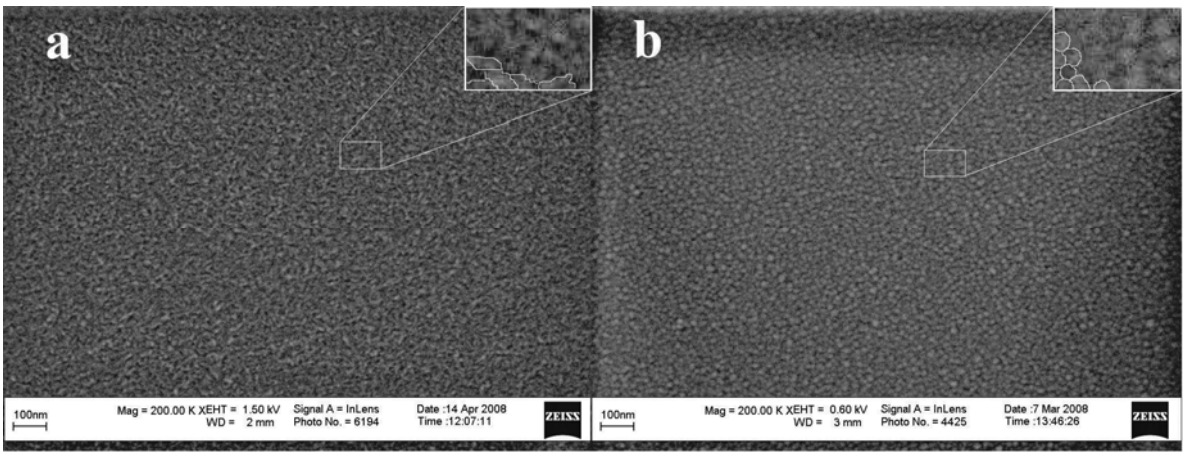

Figure 3.8 SEM micrograph of CIS film of thickness a) 1000 nm and b) 3000 nm

The composition and structure analysis shows that up to 90.76% of stoichiometry can be achieved and presents complete formation of chalcopyrite structure of the films with high degree of preferred orientation towards (112) plane.

3.3 OPTICAL PROPERTIES

I-III-VI_2 chalcopyrite semiconductors such as CIS are the leading materials for absorbers in heterojunction photovoltaic devices because of their direct band gap and high absorption coefficient as reported in the references [24-31]. A direct band gap values for the as-deposited and annealed CIS films of 1.04, 0.99 (300 °C) and 0.94 eV (450 °C) respectively have been reported by Mehdaoui *et al* [24] and they have attributed the decrease in band gap to quantum size effect, which results due to the small grain size (5nm). CIS thin films deposited by vacuum evaporation with composition Cu: 0.20, In: 0.17 and Se: 0.63 showed an energy gap of 1.04 eV as reported by Moharram *et al* [25]. An energy gap of 1.02±0.015 eV has been reported by Amara *et al* [26] for CIS films prepared by simultaneous vacuum evaporation. Yang [27] has observed the band gap of CIS films prepared by selenization of co-sputtered Cu-In films to lie in the range 0.96-1.01 eV. The variation in band gap is attributed to high free carrier and impurity concentration [28, 29]. Absorption coefficient (α) of the order of 10^5 cm^{-1} has been reported for copper rich films by Kajari *et al* [30]. They have observed that copper rich films have higher α value than indium rich films. CIS films with at least two types of optical transitions have been reported by Valdés *et al* [31]. They have observed the first fundamental transition to be direct allowed and the subsequent two transitions as direct forbidden. Energy gap of 1.02 eV for stoichiometric CIS films has been reported by Yamaguchi [32] with composition Cu/In =0.93 to 0.94 prepared by r. f. sputtering. The observed variation in band gap for different films has been attributed to the non-uniformities in the composition of polycrystalline films. The variation of absorption coefficient with composition has been studied by Isomura [33]. It has been observed that the absorption coefficient is increasing until the Cu/In ratio approaches unity and then decreasing as the ratio increased beyond unity. The dependence of room temperature absorption coefficient on photon energy for CIS films produced at $[O_2]/([Ar]+[O_2])$ = 0%, 3% and 5% have been studied by Dhanam

[34]. For films produced at 0% they have obtained an absorption coefficient greater than $3x10^4$ cm^{-1} and a direct band gap ≈ 1.0 eV. The band gap was found to increase with increase in $[O_2]/([Ar]+[O_2])$ ratio. The optical bandgap values were obtained using equations 2.15 to 2.18 from chapter II.

3.3.1 Results and discussion

Figure 3.9 shows the transmittance spectra and the plots of $(\alpha h\nu)^2$ versus hν of CIS films deposited at different substrate-target distances.

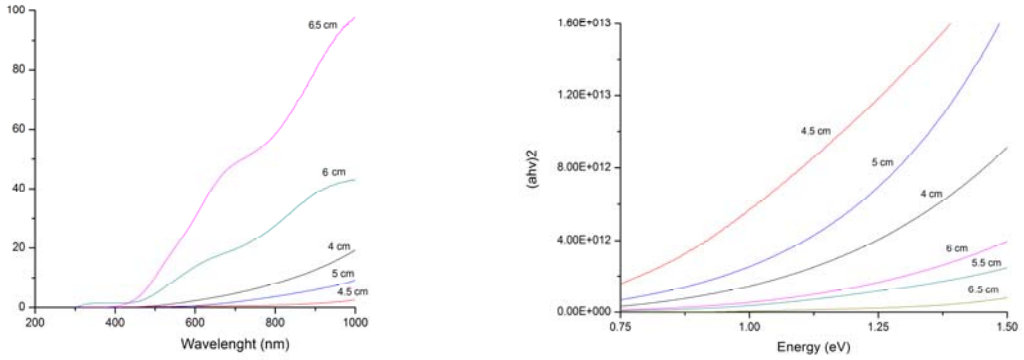

Figure 3.9 Transmittance spectra and the plot of $(\alpha h\nu)^2$ vs hν of CIS deposited at different distances.

The energy gap of the films have been determined by extrapolating the linear portion of the plots $(\alpha h\nu)^2$ versus hν to the energy axis. The presence of a single slope in the curves suggests that all the films are single phase in nature with direct allowed transition. This type of transition has already been reported by several workers for CIS films [22-34]. From the structural values we can see the relation between the grain size and the band gap. As the grain size increase, the band gap value gets closer to the bulk (1.04 eV). Table 3.8 presents the calculated optical values of the CIS films deposited at different distance from the source.

Table 3.8 Optical parameters of the r. f. sputtered CIS thin films deposited at different substrate-target distances

Distance (cm)	Band gap	*n* at 900 nm	*α* (cm-1)	*k* (10^{-2})	εr	εi
4	1.03	3.75	4229.90	3.03	14.09	0.2274
4.5	1.04	3.76	13057.55	9.35	14.13	0.7032
5	1.04	5.01	5990.50	4.29	25.10	0.4299
5.5	1.01	3.74	942.86	0.68	13.98	0.0505
6	1.03	3.79	1894.65	1.36	14.36	0.1028
6.5	1.03	4.03	1139.45	0.82	16.22	0.0657

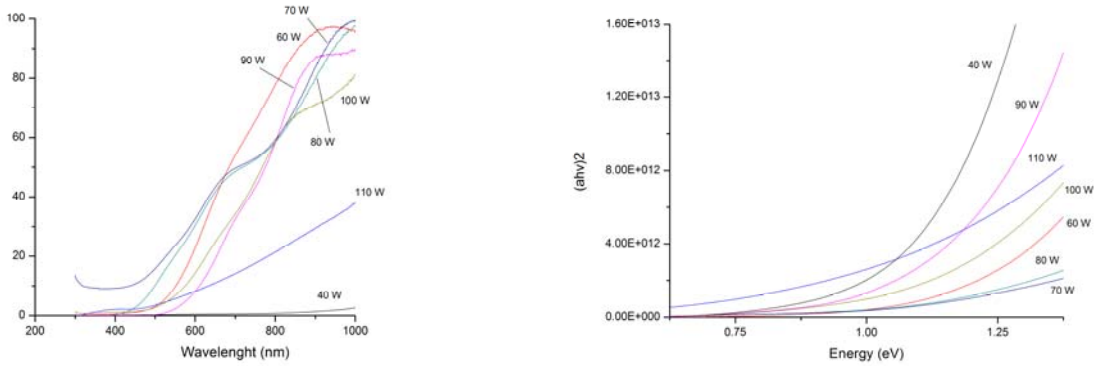

Figure 3.10 Transmittance spectra and the plot of $(\alpha h\nu)^2$ vs hν of CIS deposited at different power supply

Figures 3.10 shows the transmittance spectra and the plots of $(\alpha h\nu)^2$ versus hν of CIS films deposited at different power. From the graph $(\alpha h\nu)^2$ vs hν we can see that the film deposited at 110 W has different shape than the other graphs, this is due that the grain size is to small (73 nm) compared to the others.

Table 3.9 Optical parameters of the r. f. sputtered CIS thin films deposited at different Power

Power (W)	Band gap	*n* at 900 nm	*α* (cm^{-1})	*k* (10^{-2})	εr	εi
40	1.05	3.76	13057.55	9.35	14.13	0.7032
60	1.03	1.61	234.87	0.17	2.58	0.0054
70	1.04	1.94	2501.68	1.78	10.83	0.1174
80	1.03	4.03	1139.45	0.82	16.22	0.0657
90	1.05	2.29	711.23	0.51	5.24	0.0233
100	1.01	4.01	1702.28	1.22	16.06	0.0977
110	0.95	3.79	1894.65	1.36	14.36	0.1028

The transmittance spectra of CIS thin films with different thicknesses and the plot of $(\alpha h\nu)^2$ versus hν are shown in the figure 3.11. The absorption coefficient (α) has been calculated from the transmittance values and is found to be of the order of 10^4 cm^{-1}. This is in accordance with the reported values [34].

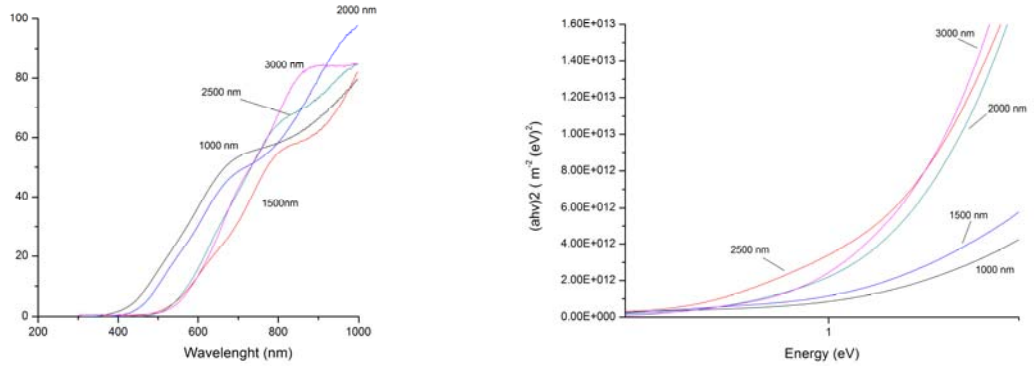

Figure 3.11 Transmittance spectra and the plot of $(\alpha h\nu)^2$ vs hν of CIS with different thicknesses.

The optical parameters of the deposited CIS with different thicknesses are given in Table 3.10.

Table 3.10 Optical parameters of the r. f. sputtered CIS thin films deposited with different thickness.

Thickness (nm)	Band gap	*n* at 900 nm	α (cm^{-1})	*k* (10^{-2})	εr	εi
1000	1.07	2.43	4112.77	2.95	5.92	0.1434
1500	1.05	4.25	3186.89	2.28	18.04	0.1939
2000	1.03	4.03	1139.45	0.82	16.22	0.0657
2500	1.02	2.92	1247.89	0.89	8.51	0.0521
3000	1.01	2.72	573.98	0.41	7.41	0.0224

The band gap of all CIS films has been found to lie in the range between 0.95 and 1.05 eV. Hörig *et al* [35] have analysed the variation of band gap and have attributed it to small stoichiometric variations, defects in layers and small non-parabolicities in the band structure. Cu/In ratio less than one means that more indium atoms are available on copper site. Masse [36] has reported that a local increase or decrease in the energy gap was induced when an atom was replaced by another atom having a different size in CIS and I-III-VI_2 compounds.

3.4 ELECTRICAL PROPERTIES

A decisive step in the development of solar cells is to understand the photovoltaic characteristics and transport mechanism of the device. Understanding the physical origin of the recombination current is very important for improving the performance of the photovoltaic cells. The ac, Hall Effect and photosensitivity measurements of the r. f.

sputtered films are presented in this section. The chief advantage of ac measurement is that permits investigation into the interior of the insulating materials. Since the biasing voltage is only 0.05 V, that is the minimum field within the insulating material, there is no possibility of more than one conduction process being active. Another main reason for the study of ac conduction is the assumption that conductivity is dominated by the deep defect levels lying in the mobility gap of these materials. Hence study of ac conductivity in these materials will explain the nature of these levels. The study of ac conduction properties provides knowledge of the activation energy, frequency dependence of conductivity etc.

3.4.1 AC conduction studies

The frequency dependence of the ac conductivity of thin film capacitors for different distance substrate-target, power and thicknesses under dark are shown in logarithmic plots in figures 3.12 a, b and c respectively. Figures 3.13, shows the frequency dependence of ac conductivity of the films under 1000 lux.

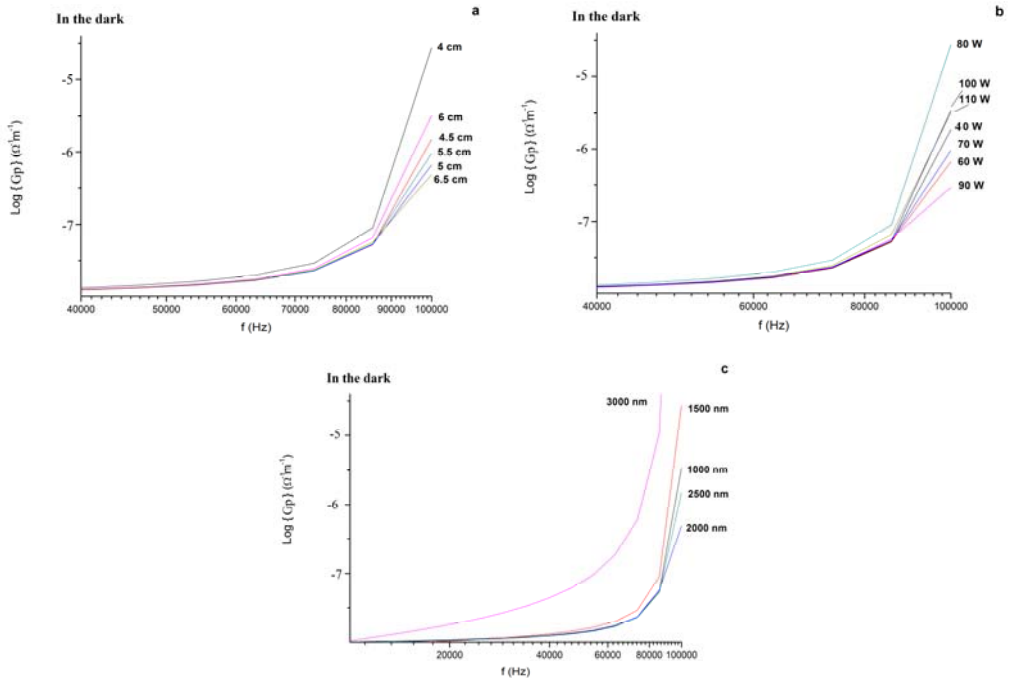

Figure 3.12 Frequency dependence CIS thin films in dark with varying a) Distance, b) Power and c)Thickness.

In all the films, under dark as well as under 1000 lux, the curves exhibit two dispersive regions; one below 60 kHz and the other above 60 kHz. The ac conductivity is observed to be proportional to ω^n, where n varies depending on the frequency. The presence of two dispersive regions in the conductivity versus frequency plot suggests that there are two dissipation mechanisms operating in the frequency range studied. This behavior suggests that the mechanism responsible for conductivity is hopping type. In the first region (<60 kHz) the value of n is found to vary from 0.5 to 0.8. It has been observed that n increases as the thickness increases; except for the thicknesses 2000 and 2500 nm, for which n drastically decreased. The differing contributions to conductance from the carrier movement (carrier movements between and within defect wells) at different thicknesses results in the increase of n, similar results reported by Djellal [37]. In the second region (>60kHz) n is found to vary from 1.5 to 1.8, it shows a square law dependence on frequency at all thicknesses examined.

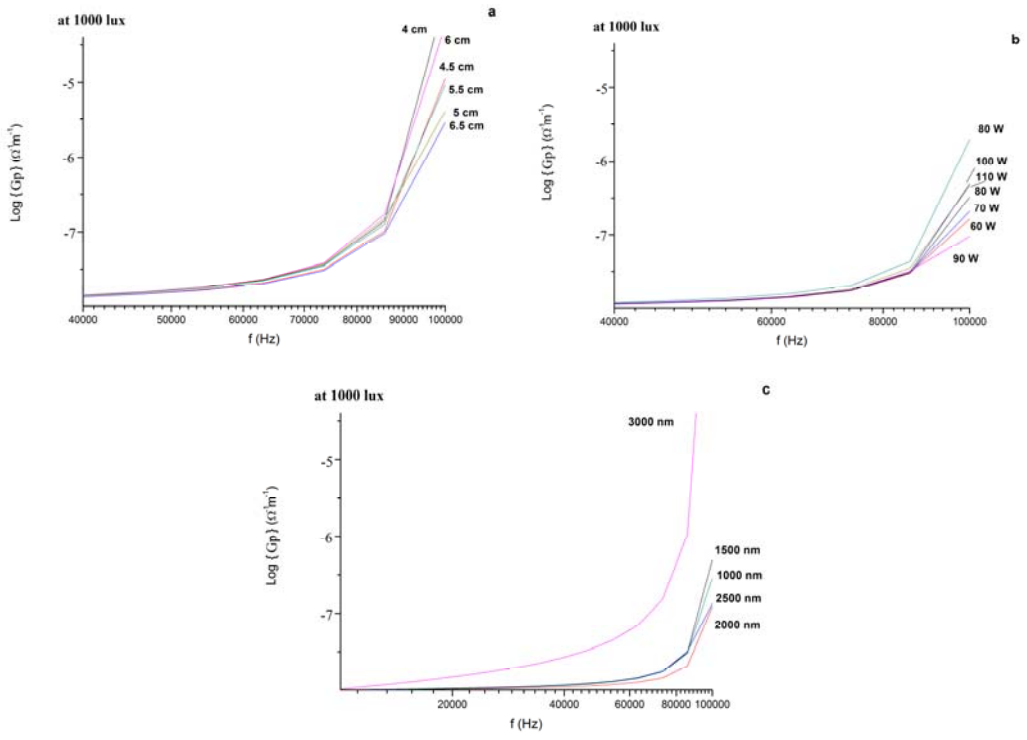

Figure 3.13 Frequency dependence under 1000 lux of CIS thin films varying a) Distance, b) Power and c) Thickness.

3.4.2 Hall effect calculations

Hall voltage has been measured for CIS thin films deposited at different powers, thicknesses and distance from source. Positive Hall voltage has been observed for most of the films. The obtained positive Hall voltage indicates that CIS films are of p-type nature with holes as majority charge carriers. Hall coefficients (R_H) of the sputtered deposited CIS thin films have been evaluated from the measured Hall voltage values. The presence of p-type or n-type conductivity nature in CIS films depending on composition is revealed by the positive and negative values of the Hall coefficients. Table 3.11 presents the composition and Hall coefficient results of the CIS films deposited at different substrate-target distances.

Table 3.11 Composition and Hall Coefficient results of the sputtered CIS thin film deposited at different substrate-target distances.

Distance (cm)	Cu/In	Se/(Cu+In)	Hall Coefficient	Type
4	0.26	0.88	1.2	P
4.5	0.98	0.65	1.3	P
5	0.46	0.75	1.4	P
5.5	0.46	0.87	1.0	P
6	0.72	0.70	1.4	P
6.5	1.21	0.66	1.6	P

All the films presented p-type conductivity. The composition and Hall coefficient results of CIS films deposited at different power are presented in table 3.12.

Table 3.12 Composition and Hall Coefficient results of the sputtered CIS thin film deposited at different power.

Power (W)	Cu/In	Se/(Cu+In)	Hall Coefficient	Type
40	0.4	0.77	1.6	P
60	0.64	1.23	1.1	P
70	0.69	1.07	1.5	P
80	1.21	0.66	1.6	P
90	0.68	0.66	-0.4	N
100	0.77	0.68	-0.6	N
110	0.72	0.7	-0.6	N

Three of the CIS films presented negative Hall voltage. The observed negative Hall voltage clearly suggests that these films are of n-type with electrons as majority charge carriers. As it can be seen in table 3.12, there is a relation between the composition and the semiconductor type. Similar observation of the presence of n-type or p-type conductivity

depending on the composition in CIS films has been reported by several workers [16, 38]. It may be assumed that the concentration of Se-vacancies (donor type defect) increases the electron carriers [38]. Film deposited at 80 W presented p-type conductivity even though selenium concentration is low. One possible explanation for this is because the copper content is large amount higher to the other films. Similar dependence of carrier density on copper and selenium concentration in CIS films has been reported by Kaigawa *et al* [18]. The variation of Hall coefficient with thickness is shown in Fig. 3.13.

Table 3.13 Composition and Hall Coefficient results of the sputtered CIS thin film deposited with different thickness.

Thickness (nm)	Cu/In	Se/(Cu+In)	Hall Coefficient	Type
1000	0.76	0.79	1.8	P
1500	0.84	0.8	2.5	P
2000	1.21	0.66	1.6	P
2500	0.81	0.97	1.4	P
3000	1.81	0.83	1.2	P

The carrier concentration of the deposited CIS films has been calculated using the experimentally obtained Hall coefficient values. The carrier concentration is found to be of the order of 10^{17} cm^{-3}. In general, the carrier concentration is also observed to vary with the concentration. The carrier concentration is found to increase with increase in selenium as shown in figure 3.14.

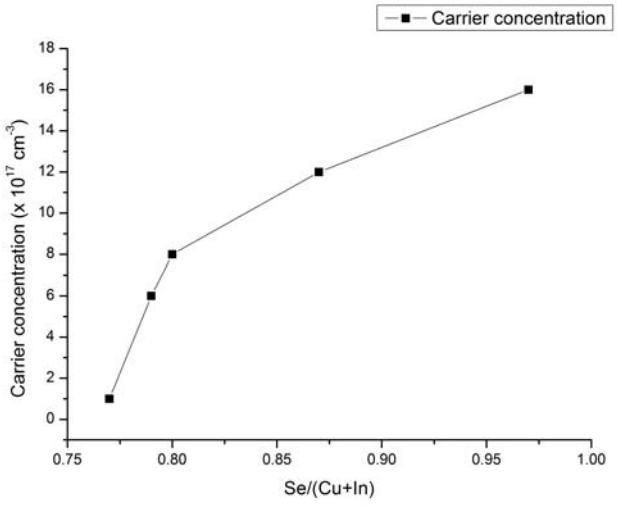

Figure 3.14 Carrier concentration varying selenium concentration.

3.4.3 I-V results

Figure 3.15 shows the results of measuring the resistivity of a CIS film in darkness and under illumination (1000 lux) varying the voltage from 1 to -1 V. Upon illumination, a large part of the photo generated charge carriers got trapped in the grain boundary. This causes a reduction in the height of the barrier between grains and the carriers can move with less resistance [39]. The resistivity of the films was evaluated from the I-V measurements and it is shown in table 3.7.

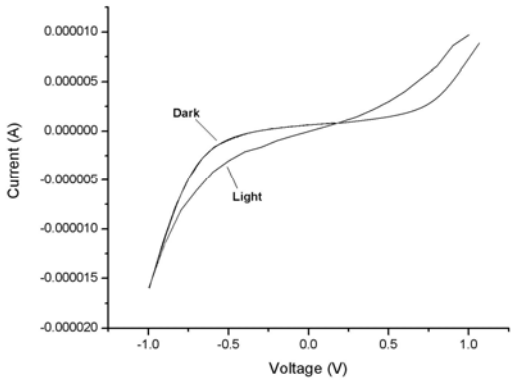

Figure 3.15 I-V result under illumination and dark of the CIS film with thickness of 2000 nm.

Table 3.14 presents the values of the resistivity in the dark and under 1000 lux of illumination.

Table 3.14 Resistivity under illumination and dark of the sputtered CIS thin film deposited at different distance.

Distance (cm)	Resistivity (Dark) (Ω-cm)	Resistivity (1000 lux) (Ω-cm)
4	1.77	1.39
4.5	1.71	1.67
5	1.54	1.47
5.5	1.31	1.04
6	1.27	1.20
6.5	2.07	1.49

Distance parameter does not make a direct relation to the resistivity property.

Table 3.15 Resistivity under illumination and dark of the sputtered CIS thin film deposited at different power.

Power (W)	Resistivity (Dark) (Ω-cm)	Resistivity (1000 lux) (Ω-cm)
40	1.36	1.20
60	2.12	1.94
70	3.24	1.61
80	2.07	1.49
90	3.84	2.30
100	4.27	2.31
110	7.30	4.07

Table 3.15 presents that at higher power, the resistivity increases, and it may be attributed to the presence of more crystallites per unit area for eg. films deposited at 100 and 110 W have higher number of crystallites per unit area than the other films (2708 and 5113 resp). Higher numbers of crystallites reduces the electron drift velocity and thus increases the resistivity. The resistivity values of CIS films deposited with different thicknesses are reported in table 3.16.

Table 3.16 Resistivity under illumination and dark of the sputtered CIS thin film deposited with different thickness.

Thickness (nm)	Resistivity (Dark) (Ω-cm)	Resistivity (1000 lux) (Ω-cm)
1000	8.89	4.02
1500	6.94	1.55
2000	2.07	1.49
2500	2.72	1.20
3000	1.21	1.05

As expected resistivity of the films decreases with thickness, but as shown in the table 3.16, the resistivity under illumination is less dependent on thickness than in the dark. The effect of decreasing resistivity with the thickness can be explained as follows: by increasing the thickness of the films, the grain size increases, which finally results in decreasing the grain boundaries and thus reducing the resistivity.

3.5 CONCLUSIONS

From the above investigations, CIS thin films were successfully prepared by single target r. f. sputtered technique. The sputtering technique, similar to other plasma techniques is very sensitive to the input parameters. For this reason, in the present investigation, the

effects of distance, power and thickness were analyzed and the following conclusions were obtained:

The energy dispersive x-ray analysis shows that one step r. f. sputtering deposition is not enough to obtain stoichiometric and device quality CIS films. It was found from the composition analysis that the films were deficit in elemental copper and therefore, in order to attain the stochiometry, an additional copper evaporation and annealing treatment was performed. After this process, the films showed good stoichiometry, crystallinity and morphology.

It was found that by varying the distance between the substrate and the source, the composition Cu/In ration shifted from 0.26 to 1.21. Hence it is found to have influence over the concentration of the films. Films deposited at 6.5 cm had better stoichiometry than those deposited at smaller distance. The structural analysis indicated that all the films possess chalcopyrite structure. The films had preferred orientation to the (004) plane with the exemption of the film deposited at 6.5 cm, which had a preferred orientation to the (112) plane. Various structural parameters were evaluated and discussed, for eg. the grain size was found to vary from 198 nm to 239 nm without any linearity and the strain fluctuated around the value of 1.5×10^{-3}. The optical band gap was determined from optical transmittance data and it was found that the band gap of the CIS films did not significantly change with the distance. The optical band gap of the films is 1.03 eV, almost the bulk value. The results of electrical properties like Hall effect, I-V, AC conduction studies on CIS films deposited at various distances between source and substrate yielded the resistivity as ± 0.45 Ω-cm in dark and ± 0.33 Ω-cm under illumination. Also it showed that the films had a resistance value of 1.04 Ω-cm, which is adequate for high quality photovoltaic devices. The results from Hall effect measurements showed that all the films are P type semiconductors.

Having been optimized the films for its stoichiometry with varying distances between source and substrate, the effect of input power on the nature of the films were systematically studied. The most remarkable effect of varying the power over deposition is

the grain size. It was found to vary from 73 nm to 287 nm with a variation of from 40 to 110 W. Even though there is no linear variation of orientation with power, the preferential orientations was also affected by the power in which some films were preferentially oriented to (004) and others to (101) or (112). The fact is that as lower is the power, the film grows slowly by allowing the grains to have more time to grow so as to obtain further oriented films. However, the planes observed at low power (40-70 W) are not the best planes desired for photovoltaic purposes. On the other hand, at a higher power (100-110 W), there was no preferential orientation and the grain size is too small, thus the resistivity is too high to get high quality energy conversion. High quality films can be assured in a power range between 80 to 90 W. The optical analysis suggested that the films exhibit a direct allowed transition with an average band gap of 1.02 eV which is considered suitable for photovoltaic applications. From the Hall effect analysis it was found that the films deposited at power above 80 W presented a N type material. The resistivity of the p type films lied 2.19 and 1.56 Ω-cm in dark and under illumination respectively.

Films were optimized with different source substrate distance and with various input power. In order to study the influence of thickness over various parameters and on the crystallization of the films, CIS of various thicknesses were deposited on glass substrates. Consequently structure analysis indicated that as the thickness of the CIS films increased from 1000 to 3000 nm, the grain size of the films linearly increased from 116 to 199 nm. However the preferred orientation for photovoltaic purposes is the (112) plane and there is a shift from (112) to (004) plane at 2500 nm. Considering this fact, it is not recommended to go beyond the thickness of 2000 nm. From the optical analysis it is seen that all the films showed suitable optical properties for energy conversion. The value of 10^4 cm^{-1} for the absorption coefficient is enough to absorb the light for energy conversion, and the band gap of nearly 1.03 eV is considered suitable for photovoltaic cell applications. It was determined from the electrical analysis that the resistivity noticeably decreased with increasing thickness.

Therefore the recommended conditions to achieve suitable CIS films for photovoltaic absorber layer are:

1. 6.5 cm distance between the source and the substrate.
2. 80 W of source power deposition
3. 2000 nm thickness
4. 13 seconds of copper evaporation at 35 Å/s
5. 15 minutes of annealing at 500°C

These condition will achieve polycrystalline CIS films with chalcopyrite structure with a preferred orientation to the (112) plane, grain size of 167 nm, band gap of 1.03 eV, absorption coefficient of 1.14×10^4 cm^{-1} and a resistivity under illumination of 1.49 Ω-cm.

REFERENCES

[1] K. T. L. De Silva, W. A. A. Priyantha, J. K. D. S. Jayanetti, B. D. Chithrani, W. Siripala, K. Blake, I. M. Dharmadasa, Thin Solid Films, 382 (2001) 158-163.

[2] S.J. Kim, H.B. Im, Thin Solid Films, 214 (1992) 194-199.

[3] W. K. Kim, E. A. Payzant, S. Yoon, T. J. Anderson, Journal of Crystal Growth, 294 (2006) 231-235.

[4] S. Mehdaoui, O. Aissaoui, N. Benslim, M. Benabdesslem, L. Bechiri, L. Mahdjoubi, G. Nouet, Vacuum, 82 (2008) 1194-1197.

[5] S. Agilan, D. Mangalaraj, Sa. K. Narayandass, S. Velumani, Alex Ignatiev, Vacuum, 81 (2007) 813-818.

[6] D. Haneman, S. N. Sahu, R. D. L. Kristensen, Thin Solid Films, 163 (1988) 167-174.

[7] S. Kohiki, M. Nishitani, K. Nishikura, T. Negami, M. Terauchi, T. Hirao, Thin Solid Films, 207 (1992) 265-269.

[8] G. Aren, V. D. Vankar and O. P. Agnihotri, Journal of Applied Physics, 72 (1992) 3659-3663.

[9] J. A. Groenink, P. H. Janse, Z. Physical Chemistry 110 (1978) 17-20.

[10] N.M. Shah, C.J. Panchal, V.A. Kheraj, J.R. Ray, M.S. Desai, Solar Energy, 83 (2009) 753-760.

[11] N. M. Shah, J.R. Ray, K. J. Patel, V.A. Kheraj, M.S. Desai, Thin Solid Films 517 (2009) 3639-3644.

[12] Alaa A. Akl, H.H. Afify, Materials Research Bulletin, 43 (2008) 1539-1548.

[13] G.S. Chen, J.C.Yang, Y.C.Chan, L.C.Yang, Welson Huang, Solar Energy Materials & Solar Cells 93 (2009) 1351-1355.

[14] T. Tanaka, T. Yamakuchi, A. Wakahara, A. Yoshida, R. Toniguchi, Y. Matsuda, M. Fujishiro, Solar Energy Materials and Solar Cells, 75 (2003) 115-120.

[15] Jenny Nelson, The Physics of Solar Cells, Imprerial College, UK 2003

[16] F. O. Adurodija, S. F. Kim, S. D. Kim, J. S. Song, K. H. Yoon, B. T. Ahn, Solar Energy Materials and Solar Cells, 55 (1998) 225-236.

[17] F. Hergert, S. Jost, R. Hock, M. Purwins, Journal of Solid State Chemistry, 179 (2006) 2394-2415.

[18] R. Kaigawa, T. Uesugi, T. Yoshida, S. Merdes, R. Klenk, Thin Solid Films, 517 (2009) 2184-2186.

[19] G. Masse, K. Djessas, Thin Solid Films, 226 (1993) 254-258.

[20] Akhlesh Gupta, S. Isomura, Solar Energy Materials and Solar Cells, 53 (1998) 385-401.

[21] J. Bekker, Solar Energy Materials and Solar Cells, 93 (2009) 539-543.

[22] Guozhong Cao, Nanostructures and nanomaterials, Imperial College, USA

[23] A. Tverjanovich, E.N. Borisov, E.S. Vasilieva, O.V. Tolochko, I.E. Vahhi, S. Bereznev, Yu.S. Tveryanovich, Solar Energy Materials and Solar Cells, 90 (2006) 3624-3632.

[24] S. Mehdaoui, N. Benslim, O. Aissaoui, M.Benabdeslem, L. Bechiri, A. Otmani, X. Portier, G. Nouet, Materials Characterization, 60 (2009) 451-455.

[25] A. H. Moharram, I. M. Al-Mekkawy, A. Salem, Applied Surface Science, 191 (2002) 85-93.

[26] A. Amara, A. Ferdi A. Drici, J. C. Bernède, M. Morsli, M. Guerioune, Catalysis Today, 113 (2006) 251-256.

[27] L. C. Yang, Journal of Crystal Growth, 294 (2006) 202-208.

[28] N. Stratieva, E. Tzvetkova, M. Ganchev, K. Kochev, I. Tomov, Solar Energy Materials and Solar Cells, 45 (1997) 87-96.

[29] T. Tanaka, A. Wakahara, A. Yoshida, Journal of Applied Physics, 87 (2000) 3282.

[30] Kajari Das, Subhendu K. Panda, Soma Gorai, Pratima Mishra, Subhadra Chaudhuri, Materials Research Bulletin, 43 (2008) 2742-2750.

[31] M. Valdés, M. Vázquez, A. Goossens, Electrochemica Acta, 54 (2008) 524-529.

[32] Toshiyuki Yamaguchi, Jiro Matsufusa, Akira Yoshida, Solar Energy Materials and Solar Cells, 27 (1992) 25-35.

[33] S. Isomura, S. Shirakata, T. Abe, Solar Energy Materials, 22 (1991) 223-230.

[34] M. D. Kannan, R. Balasundaraprabhu, S. Jayakumar, P. Ramanathaswamy, Solar Energy Materials and Solar Cells, 81 (2004) 379-395.

[35] W. Hörig, H. Neumann, H. Sobotta, B. Schumann, G. Kühn, Thin Solid Films, 48 (1978) 67-72.

[36] G. Masse, Journal of Applied Physics, 68 (1990) 2206.

[37] L. Djellal, A. Bouguelia, M. Kadi Hanifi, M. Trari, Solar Energy Materials & Solar Cells 92 (2008) 594–600.

[38] R. Klenk, T. Walter, H. W. Shock, D. Cahen, Adv. Mater. 5 (1993) 114.

[39] Joel Pantoja Enríquez, Xavier Mathew, Solar Energy Materials and Solar Cells, 76 (2003) 313-322.

CHAPTER IV Characterization of window and contact layers

4.1 INTRODUCTION

This chapter is dedicated to the analysis and discussion of experimental techniques and characterization of the window (CdS) and contact (ITO and MO) layers of photovoltaic structure which are important for device fabrication. CdS thin films used as window layer were deposited by microwave assisted chemical bath deposition. The influence of thickness as well as annealing temperature on the structural, optical and electrical properties will be discussed. Indium tin oxide and Molybdenum, used as front and back contacts respectively, were deposited by r.f. sputtering technique. Structural properties, surface morphology, optical and electrical properties of the deposited thin film contact layers were studied and reported.

4.2 CADMIUM SULFIDE (WINDOW LAYER)

Cadmium Sulfide (CdS) is widely used as a window layer for both CdTe and $CuInSe_2$ based devices [1, 2]. The CdS/CIS heterojunction has been actively investigated as a photovoltaic junction [3, 4]. This junction has been fabricated via many methods such as sputtering, close space sublimation and physical vapor deposition [5-7]. Inspite of the fact that CdS has been investigated extensively as a hetero-junction partner to the absorber layer in photovoltaic cells, there are many other issues that have to be still understood. In photovoltaic applications, film thickness is an important parameter since it affects the microstructure of the film as well as its optical and electrical characteristics, especially the junction performance.

4.2.1 STRUCTURE, COMPOSITION AND SURFACE ANALYSIS OF CdS

Cadmium sulfide exists in two different crystalline structures: the stable hexagonal (wurtzite) and the metastable cubic (greenockite) structures. It is worth noting that both structures can be present in a material at the same time.

The formation of cubic or hexagonal structures depends on numerous factors, one of them being the selected deposition method. In a chemical bath deposition, structure of the deposited film depends on the composition, temperature and pH of the solution. For

example, the cubic phase has been reportedly obtained [8,9] by using cadmium chloride ($CdCl_2$), potassium hydroxide (KOH), ammonia nitrate (NH_4NO_3) and thiourea ($SC(NH_2)_2$) as precursors, at deposition temperature of 75 °C. In other cases [10,11], the films presented an hexagonal structure by using cadmium nitrate ($Cd(NO_3)_2$), sodium citrate ($Na_3C_6H_5O_7$), ammonia (NH_3) and thiourea ($SC(NH_2)_2$) as precursors, at a deposition temperature of 60 °C. Other sources [12-14] have been used, for which both the cubic and hexagonal structures have been obtained by chemical bath deposition. In the present synthesis, 100 ml of chemical bath is formed by an aqueous solution containing the following reactants in specified molar concentrations: 0.1M cadmium nitrate ($Cd(NO_3)_2$) as cadmium source, 1M sodium citrate ($Na_3C_6H_5O_7$) as buffer, 1M thiourea ($SC(NH_2)_2$) as sulfur source, and 30% of ammonium hydroxide (NH_4OH).

4.2.1a EFFECT OF THICKNESS

X-ray diffraction patterns of the CdS films with thickness values of 40, 53, 80, 105, 143 and 190 nm are shown in Figure 4.1. Several diffraction peaks can be observed, indicating that the films are polycrystalline in nature. The peak intensity increases as the film thickness increases and this is due to the growth of material involved in diffraction process. For thinner films of 40 and 53 nm there are no considerable peaks, thus there is no representative structure. However, as thickness increases, the peaks corresponding to both hexagonal and cubic structures become visible, indicating that there is a mixture of phases. The peak at 2θ=25.12° corresponds to hexagonal (100) plane, the peak at 26.68° is associated with the mixture of hexagonal (002) and cubic (111) planes, the peak at 28.55° corresponds to hexagonal (101) plane, the peak at 44.26° is associated with the hexagonal (110) and cubic (220) planes, and the peak at 52.39° is associated with the hexagonal (112) and cubic (311) planes. Four hexagonal peaks against three cubic peaks demonstrate that the structure of the films is predominantly hexagonal, similar to other reports [15]. The intense peak that appears at 25.12° indicates a preferential orientation of the hexagonal plane (100).

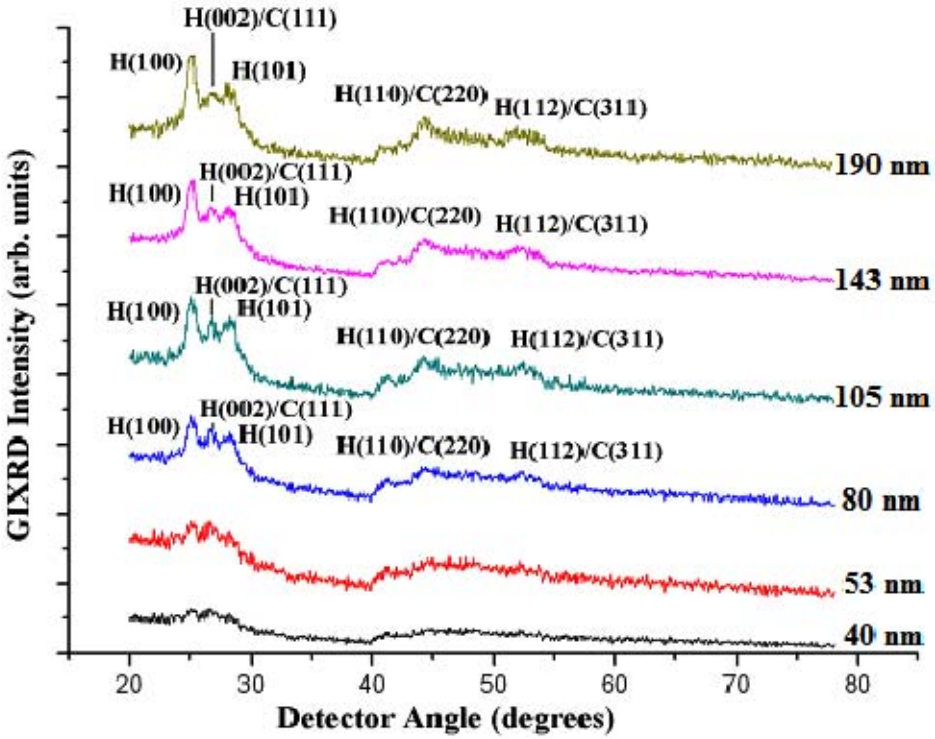

Figure 4.1 XRD patterns of the CdS films with thicknesses 400, 530, 800, 1050, 1430 and 1900 Å.

Identification and assignments of the observed diffraction patterns were made using the International Centre for Diffraction Data (ICDD), and by comparison with previous published results [16-18].

Table 4.1 Structural parameters of the hexagonal and cubic structures of CdS films with various thicknesses.

Thickness (nm)	Structure	Lattice (Å)		Grain Size (nm)	Dislocation density (δ) (10^{14} lines/m^2)	Numb. of crystallites/unit area (10^{15} m^{-2})	Strain (ε) (10^{-4})
		a	*c*				
53	**Hexagonal**	**4.1526**	**6.5627**	**9.6**	**109**	**132**	**3.96**
105	**Hexagonal**	**4.1478**	**6.7380**	**9.6**	**108**	**117**	**2.56**
190	**Hexagonal**	**4.0816**	**6.6096**	**9.9**	**102**	**195**	**2.48**
53	***Cubic***	***5.8687***		***17.5***	***33***	***21***	***2.32***
105	***Cubic***	***5.8112***		***12.8***	***61***	***50***	***3.14***
190	***Cubic***	***5.4889***		***13.1***	***58***	***84***	***2.90***

The structural parameters are shown in Table 4.1. From these values, it can be seen that the films present a nanocrystalline structure. For hexagonal structure, grain size increases while increasing the thickness, whereas in cubic structure the grain size first

decreases and then slightly increases. The decrease in strain indicates a decrease in concentration of lattice imperfections as the film thickness increases.

The morphology of CdS nanoparticles was also observed using TEM as shown in Figures 4.2 (a) and (c). It is supposed that each particle is composed of fine nanocrystallites (seen as white grains in figure), whose sizes were determined by XRD technique. The inset of corresponding figure showed the selected area electron diffraction (SAED) patterns presented in Figures 4.2(b) and (d). Each pattern shows a set of concentric rings due to the random orientation of the crystallites, corresponding to diffraction from different planes of the nanocrystallites [16, 17]. The diffraction rings have been indexed to (111), (220), and (311) planes of the cubic CdS phase (ICDD card, file No. 80-0019). The thick rings in Figure 4.2(b) show that the crystals are not well defined for the thickness of 40 nm, but for 90 nm the crystal structure is clear and therefore the rings are thin as presented in Figure 4.2(d).

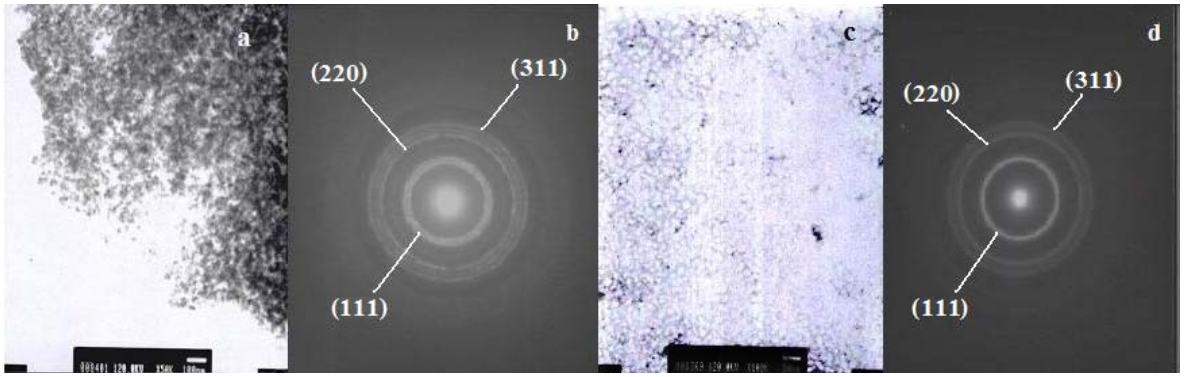

Figure 4.2 (a) and (c) show transmission electron micrographs of CdS thin films of thickness 40 nm and 190 nm, respectively. (b) and (d) show SAED patterns of CdS thin films of thickness 40 nm and 190 nm, respectively.

Surface morphology of the CBD-CdS thin films is depicted in Figure 4.3. Colloidal particles precipitate over the film during deposition, which can be clearly seen as white crystals.

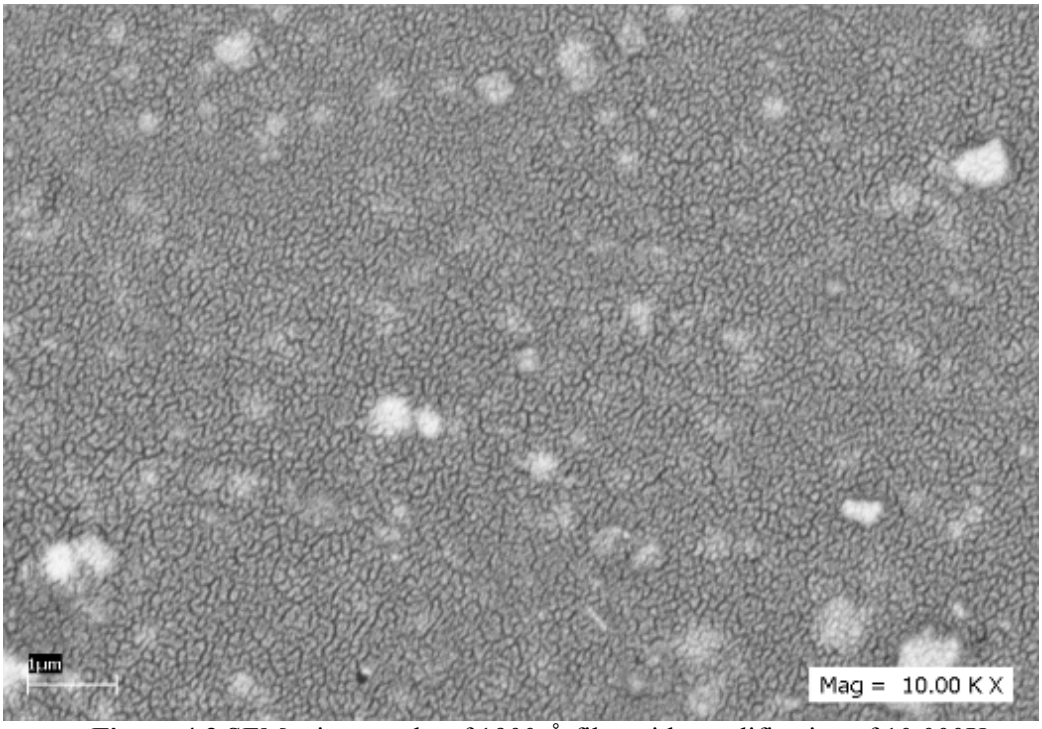

Figure 4.3 SEM micrographs of 1900 Å film with amplification of 10,000X.

Composition information was obtained from EDAX measurements (Figure 4.4). According to the results, elemental composition of CdS thin film, as shown in Figure 4.4(a), is sulfur 30.37 % at and cadmium 69.63% at.

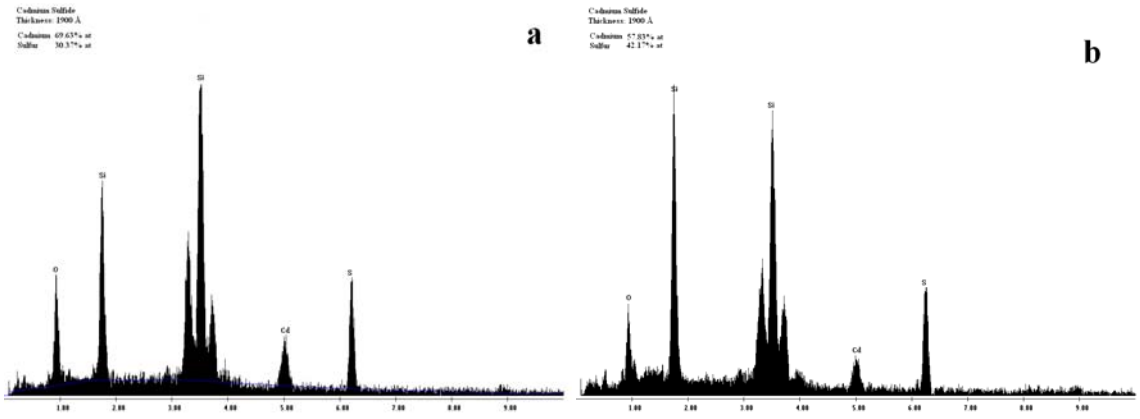

Figure 4.4 Energy distribution of the emitted radiation from (a) the 1900 Å CdS film and (b) the colloidal particles.

The colloidal particles were also analyzed, and the composition obtained, as shown in Figure 4.4(b), is sulfur 42.17 % at and cadmium 57.83% at. Colloidal particles are closer

to stoichiometry than the films, this is because colloidal particles are formed in liquid where the ion availability is higher.

AFM was used to investigate the CdS film morphology. Figure 4.5 shows two dimensional (2-D) AFM images obtained from (a) 5 x 5 μm^2 and (b) 2 x 2 μm^2 areas of the film sample with a thickness value of 40 nm. For each condition, the left image shows the height profile of sample surface whereas the image on right shows the phase profile of signal measured at each point of the surface.

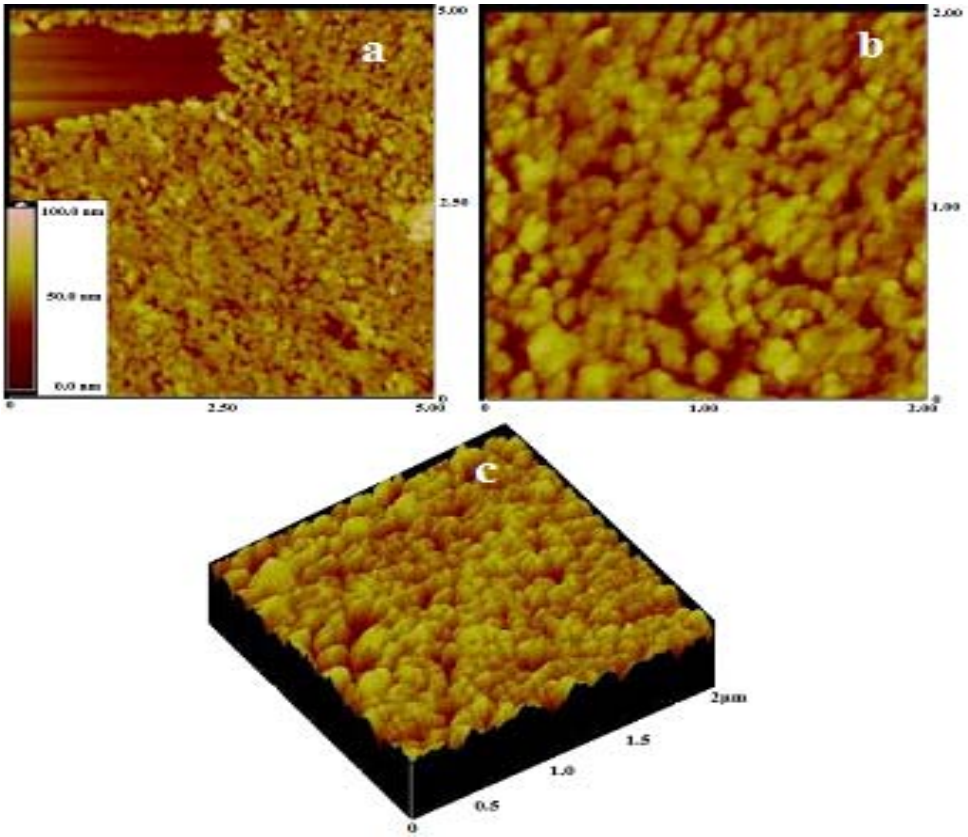

Figure 4.5 Two dimensional AFM images of the 40 nm film with areas of (a) 5 x 5 μm^2 and (b) 2 x 2 μm^2 and (c) a three dimensional AFM image of the 40 nm film with an area of 2 x 2 μm^2.

In Figure 4.5(a), the z-scale is shown at the left and a good agreement between the thickness values obtained from profile meter and AFM technique is observed. The image in Figure 4.5(b) shows good uniformity of the particles. Figure 4.5(c) presents a three dimensional (3-D) AFM image of the same 40 nm film. A normal thin film growth without any agglomeration is observed here.

4.2.1b EFFECT OF ANNEALING

Diffraction patterns of the film of thickness 143 nm annealed at 200, 250, 300, 350 and 400 °C are shown in Figure 4.6. It is observed that the peaks at 25.12° and 28.55° get broadened as the annealing temperature increases and become more pronounced at 400 °C. The peak at 26.68° is not detectable in the as-deposited film, though it can be observed after annealing at 200-300 °C, and it gets more intense when annealed at 350-400 °C. The peak at 44.26° is not observed in the as-deposited film either, yet its intensity increases as the annealing temperature increases. By examining all the patterns, it can be concluded that these films contain a mixture of both hexagonal (wurtzite) and cubic (zinc blende) structures. Since the pattern at 25.12°, corresponding to the hexagonal (100) plane, becomes sharper and higher as the annealing temperature increases; it can be assumed that the percentage of hexagonal structured crystallites in the film increases when films are annealed at higher temperatures.

Structural parameters are shown in Table 4.2. It can be noted that for hexagonal structure, grain size increases while increasing the annealing temperature up to 250 °C, after which the grain size begins to decrease.

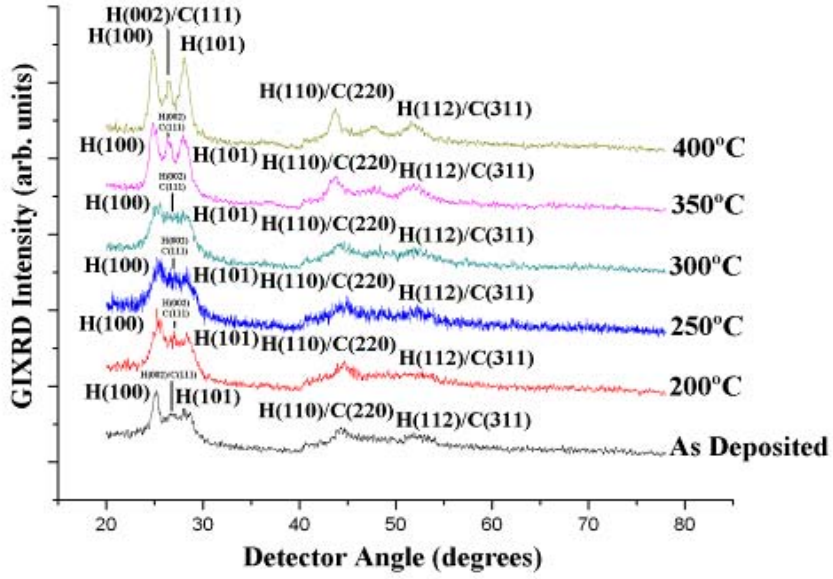

Figure 4.6 XRD patterns of the annealed CdS films.

Table 4.2 Structural parameters of hexagonal and cubic structures of CdS films at room temperature and annealed at 200, 250, 300, 350 and 400 °C.

Annealing Temperature	Structure	Lattice (Å)		Grain Size (nm)	Dislocation density (δ) (10^{14} lines/m^2)	Numb. of crystallites/unit area (10^{15} m^{-2})	Strain (ε)
		a	*c*				
RT	**Hexagonal**	**4.0816**	**6.6096**	**9.9**	**102**	**195**	**2.48**
200 °C	**Hexagonal**	**4.07**	**6.9514**	**14.2**	**50**	**67**	**1.72**
250 °C	**Hexagonal**	**4.0332**	**7.222**	**28.7**	**12**	**8**	**0.84**
300 °C	**Hexagonal**	**4.0963**	**7.2431**	**13.2**	**57**	**82**	**1.86**
350 °C	**Hexagonal**	**4.0929**	**6.9154**	**10.4**	**92**	**167**	**2.38**
400 °C	**Hexagonal**	**4.139**	**6.8576**	**13.2**	**57**	**82**	**1.88**
RT	***Cubic***	***5.4889***		***13.1***	***58***	***84***	***2.90***
200 °C	***Cubic***	***5.445***		***12.7***	***62***	***93***	***2.98***
250 °C	***Cubic***	***5.4463***		***13.9***	***53***	***80***	***2.87***
300 °C	***Cubic***	***5.5181***		***12.7***	***62***	***92***	***3.00***
350 °C	***Cubic***	***5.4637***		***8.8***	***128***	***275***	***4.28***
400 °C	***Cubic***	***5.5022***		***10.9***	***84***	***147***	***3.50***

Annealing effect on both the morphology and structure can be observed in the TEM images presented in Figure 4.7. As-deposited films present small crystallites with a high percentage of amorphous tissue. The SAED pattern of this film shows continuous and thick rings, while for the film annealed at 400 °C there are some bright spots surrounding the rings which correspond to bigger crystallites.

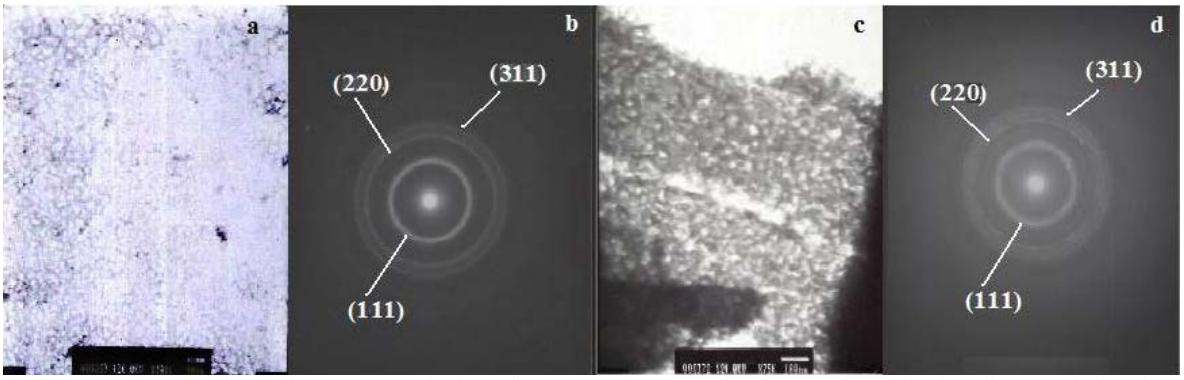

Figure 4.7 (a) and (c) show transmission electron micrographs for as-deposited and annealed CdS thin films at 400 °C, respectively. (b) and (d) show SAED patterns for as-deposited and annealed CdS thin films at 400 °C, respectively.

Figure 4.8 includes SEM micrographs of CdS films as-deposited and annealed at 200, 250, 300, 350 and 400 °C. These images show how the grains evolve as the annealing

temperature is increased. Besides the colloidal particles, it can be observed from Figure 4.8(f) that the grains adopted a 'rice and pyramidal' shape at an annealing temperature of 400 °C, which is very desirable for a window layer as this configuration allows lower reflection of the incident light [18].

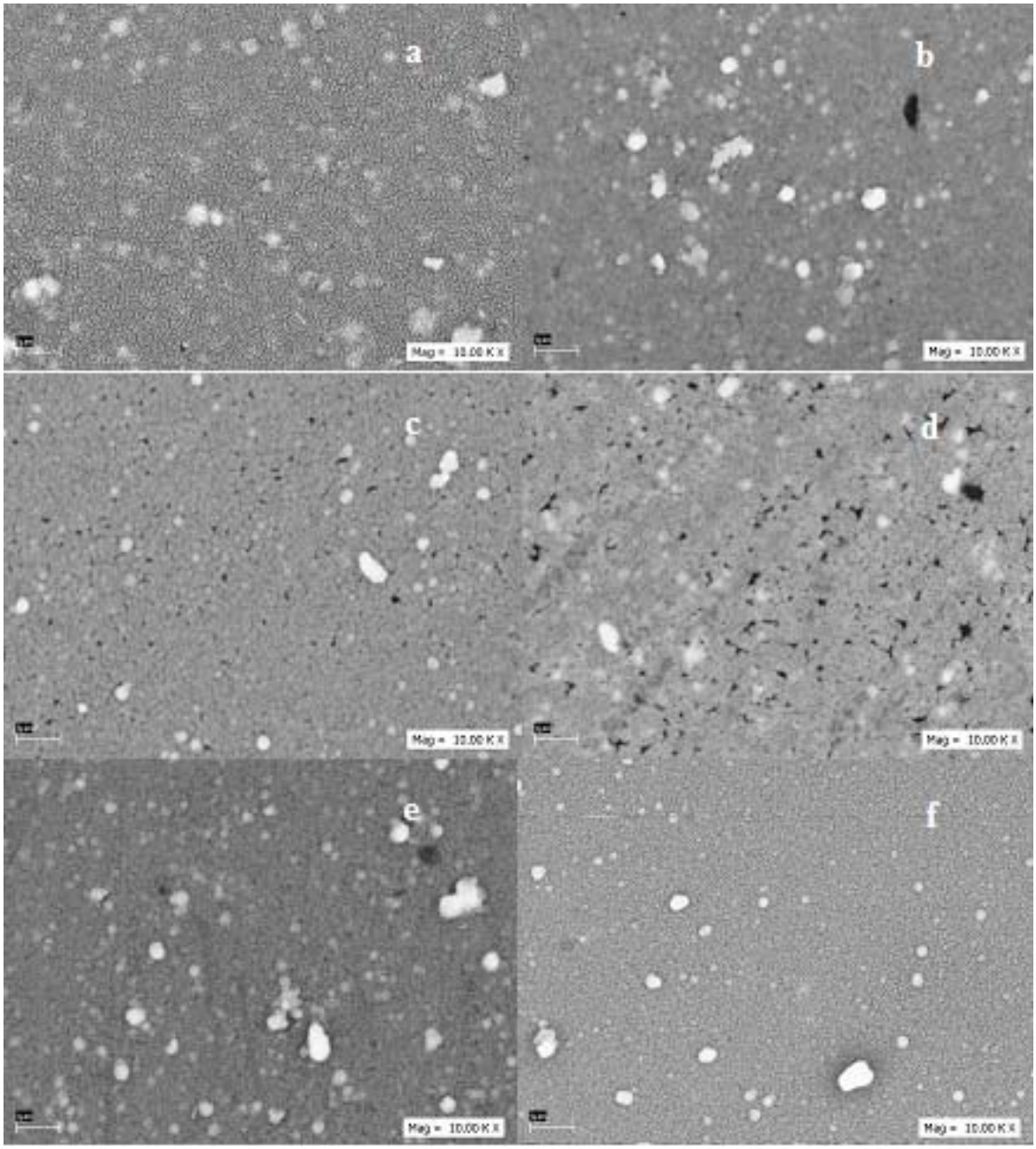

Figure 4.8 SEM micrographs of CdS thin films (a) as-deposited, (b) annealed at 200 °C, (c) at 250 °C, (d) at 300 °C, (e) at 350 °C and (f) at 400 °C.

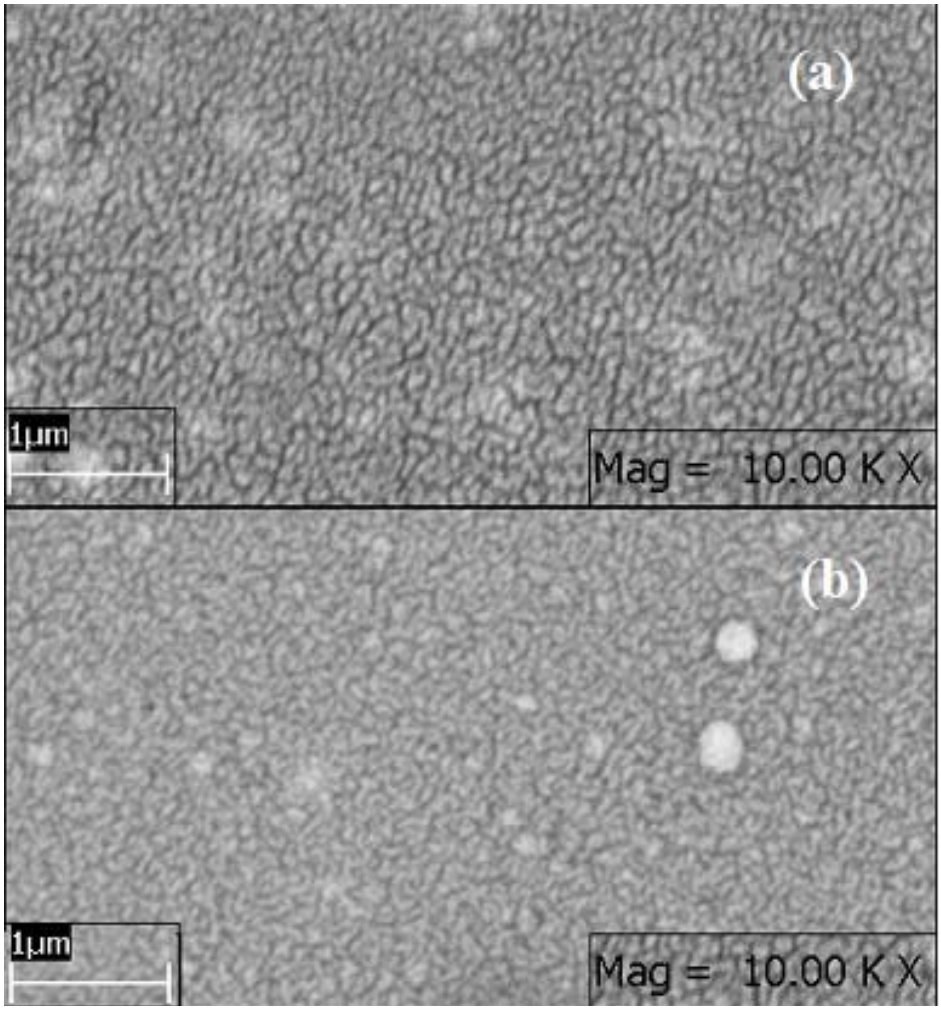

Figure 4.9 Morphology of CdS thin films with thickness 190 nm (a) as-deposited and (b) annealed at 400 °C.

The morphology of annealed CdS films was also investigated by AFM. Figure 4.10 shows 3D AFM images of the surface of films after exposing them to heat treatment. At 200 °C, the films present clusters with a globular surface morphology and as the temperature increases, the surface becomes smoother and bigger crystallites are formed.

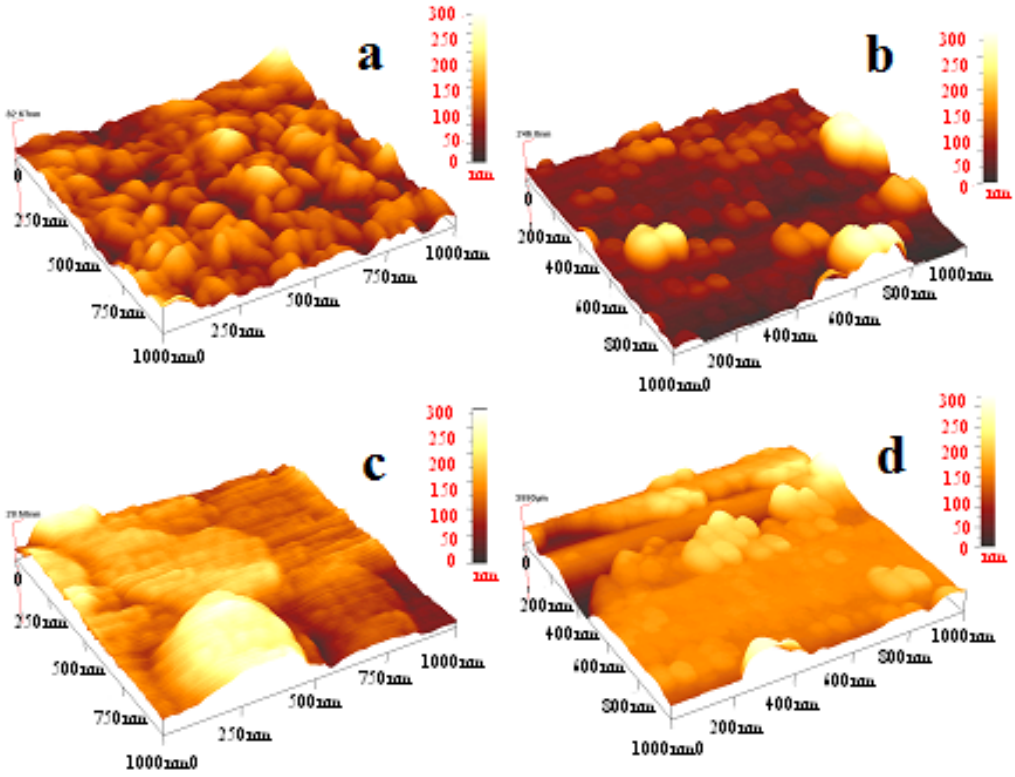

Figure 4.10 Three dimensional AFM images of CdS thin films annealed at (a) 200, (b) 250, (c) 350 and (d) 400 °C.

4.2.2 OPTICAL CHARACTERIZATION

4.2.2a EFFECT OF THICKNESS

A set of CBD-CdS films was produced. The spectral distribution of transmittance of the films with thickness values of 40, 53, 80, 105, 143 and 190 nm is shown in Fig. 4.11. The band gap values were obtained by plotting $(\alpha hv)^2$ versus $E(eV)$ and considering the slope of the graph at the band edge absorption as can be seen in the inset of Fig. 4.11.

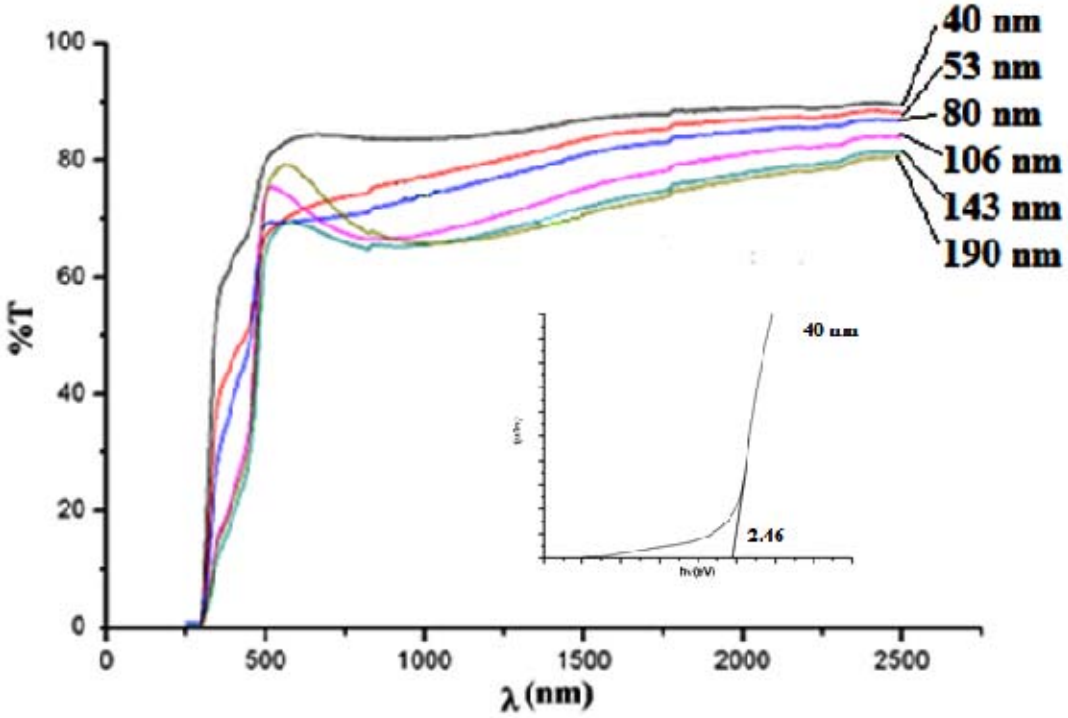

Figure 4.11 Spectral distribution of transmittance of the CdS films with different thicknesses. Inset shows the band gap calculation of the 400 Å film.

The band gap, refractive index and extinction coefficient values corresponding to different thicknesses of the CBD-CdS thin films are given in Table 4.3.

Table 4.3 Band gap, refractive index and extinction coefficient values of CdS thin films with different thicknesses.

Thickness	Band gap	*n* at 900 nm	*k* (10^{-2})
40 nm	2.46 eV	2.70	3.25
53 nm	2.40 eV	2.91	3.71
80 nm	2.50 eV	2.95	2.88
105 nm	2.53 eV	2.99	2.91
143 nm	2.57 eV	2.99	2.03
190 nm	2.54 eV	2.98	1.54

It can be noted from Table 4.3 that the maximum band gap energy value is obtained at the thickness of 143 nm, whereas the calculated values increase on increasing the film thickness. The refractive index starts increasing while increasing the thickness up to 143 nm after this thickness it decreases, similar to other reports [19].

4.2.2b EFFECT OF ANNEALING

The spectral distribution of transmittance of the films at different annealing temperatures is shown in Fig. 4.12. It can be noted here that the higher transmittance is obtained at an annealing temperature of 250 °C; except in the 500-1000 nm range, where the film annealed at 200 °C has a slightly higher transmittance.

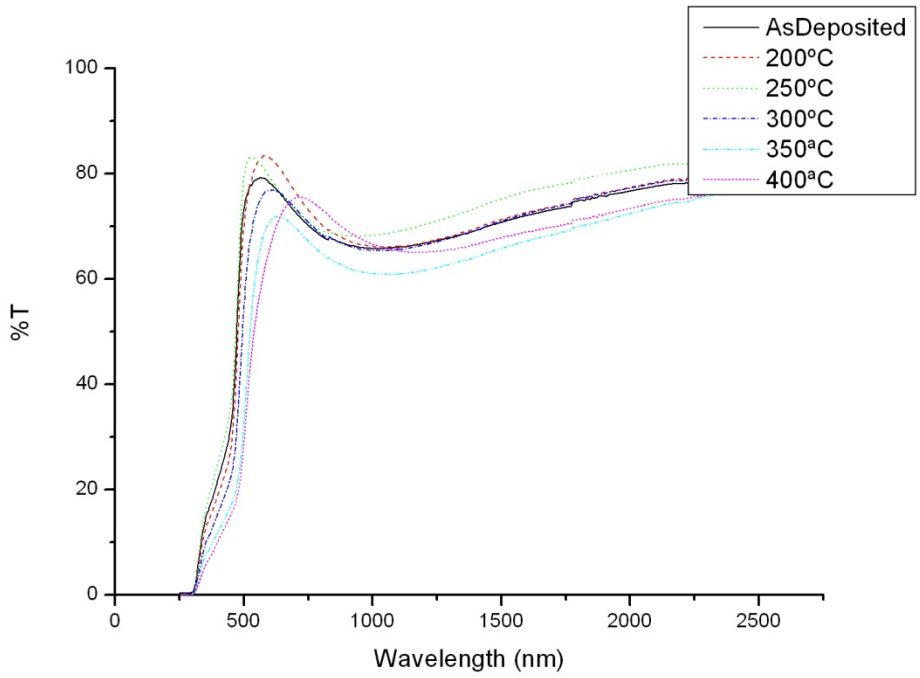

Figure 4.12 Spectral distribution of transmittance of the CdS films with different annealing temperatures.

The band gap, refractive index and extinction coefficient values corresponding to different annealing temperatures of the CBD-CdS thin films are given in Table 4.4. Similar to other reports, the optical energy gap decreases upon increasing the annealing temperature [20]. This is because at higher temperatures the grain size increases and bigger grain sizes approach to the bulk.

Table 4.4 Band gap, refractive index and extinction coefficient of CdS thin films annealed at different temperatures.

Temperature	Band gap	*n* at 900 nm	*k* (10^{-2})
RT	2.54 eV	2.98	1.54
200°C	2.52 eV	2.97	1.49
250°C	2.56 eV	2.99	1.44
300°C	2.45 eV	2.98	1.55
350°C	2.36 eV	2.97	1.79
400°C	2.34 eV	2.75	1.39

4.2.3 ELECTRICAL CHARACTERIZATION

Electrical resistivity of CdS films was measured at room temperature using the technique of the two points. For this purpose, silver electrodes 2 mm long 1with 2 mm distance of separation were painted in the samples in coplanar configuration. The currents in dark and light were measured using a pico-ammeter HP4140B with a source of direct current voltage, the applied voltage was 100V. Before making these measurements, the samples were placed in the dark for a day to vacate all the states of traps in the samples. For I-V measurements, the samples were illuminated with a tungsten-halogen lamp with a power of 600 Wm^{-2}.

4.2.3a PHOTO-RESPONSE

Figure 4.13 shows the photo-response of CdS films of different thickness grown by chemical bath. In each case, the background current (under dark, prior to the illumination) due to the applied bias was subtracted from the measured light current and hence the figure shows only the current due to the photo-generated carriers. For the films with lower thickness, current decay in the dark interval is fast and a probable reason can be the presence of less trapping centers as well as high emission rate from the traps. The Photosensitivity (S) of a semiconductor can be expressed as follows [10]:

$$S = \frac{I_{light} - I_{dark}}{I_{dark}} \qquad (5.1)$$

where I_{light} and I_{dark} are the current measures under lighting and dark respectively.

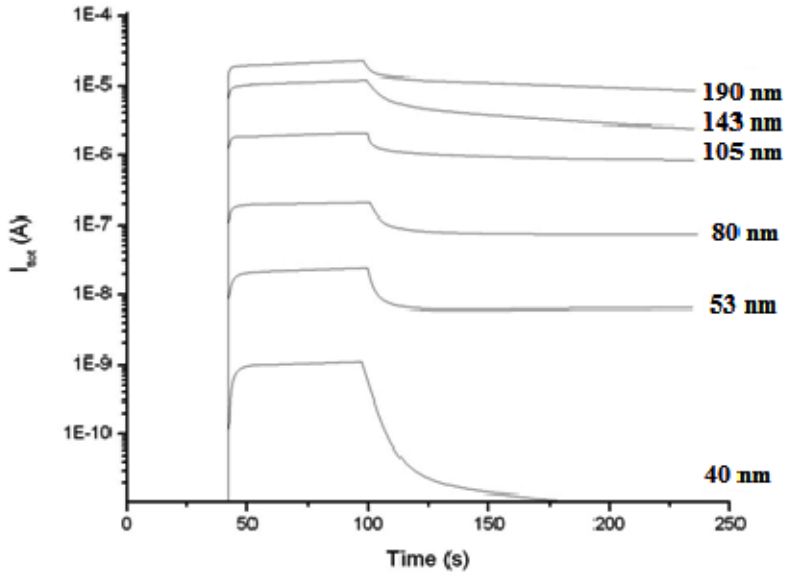

Figure 4.13 Photo-response of CdS films with different thicknesses.

The variation of photo-sensitivity depending on the thickness is shown in Figure 4.14. Decrease in S with the increase in thickness indicates that the photo-sensitivity is less for thicker films. The photo current $I_{ph}=(I_{light}-I_{dark})$ increases from 10^{-5} A to 10^{-10} A when the thickness increases from 40 to 1900 nm. This increase in photocurrent can be due to an increase in the mobility – lifetime product [11, 21, 22].

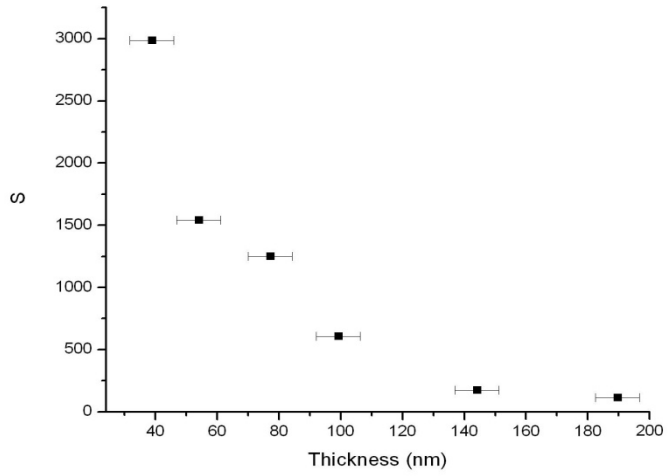

Figure 4.14 Variation of photo-sensitivity by effect of thickness.

4.2.3b RESISTIVITY

Figure 4.15 shows the results of measurement of resistivity of CdS films in dark and under illumination. As expected resistivity of the films decreases with thickness, but it can be noticed from Figure 4.15 that the dependence of resistivity on thickness is more pronounced under dark. This behavior (resistivity decreases with the thickness) can be explained as follows: when thickness increases, the grain size also increases, grain boundaries decrease and hence resistivity is less. Under photo excitation, the photogenerated carriers get trapped at the grain boundaries, this reduces the inter-grain barrier height and carriers can move with less resistance [23].

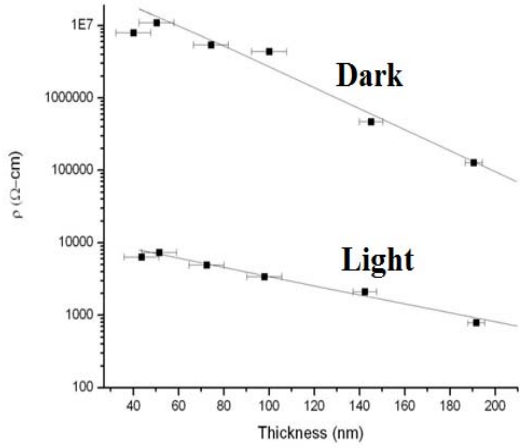

Figure 4.15 Variation of resistivity by effect of thickness.

4.2.4 DOPING

Although cadmium sulfide is a material with excellent optical properties to be used as window layer in photovoltaic cells, it has a very high resistivity that limits the transfer of carriers and thus the efficiency. For this reason the influence of doping impurity on the performance of the CdS films as window layers has been studied. Tanaka et al [22] have found that chlorine acts as a donor in $CuInSe_2$, alternatively Lee et al [24] found that boron doping of CdS from chemical bath improved the characteristics of CdTe/CdS solar cells. The influence of sodium on the electrical, photoelectrical and luminescence properties of CdS films was investigated by Bidadi et al [25].

With the intention to achieve these CdS doped thin films, the following precursors have been used: Boric Acid (H_3BO_3), sodium chloride (NaCl), Sodium Nitrate ($NaNO_3$) as boron, chlorine and sodium sources respectively. For the doped films we performed photoluminescence, Raman and SIMS analysis and reported below

4.2.4a PHOTOLUMINESCENCE

Fig. 4.16 shows PL spectra for CdS thin films doped with boron, chlorine and sodium when excited with 4579 Å Ar ion laser line. Band edge photoluminescence (BE-PL) is observed at 525 nm (2.36 eV) for boron doped, 501 and 523 nm (2.47 and 2.37 eV resp.) for chlorine doped and 530 nm (2.34 eV) for sodium doped CdS. There is no significant change in the BE-PL peak position on boron and sodium but there is a significant broadening in the chlorine BE-PL. It is also observed that the intensity of PL essentially decreases on increasing the concentration. Thus it can be concluded from the PL data that the doping with chlorine highly affects the optical properties which is not advantageous. This result is attributed to complex defects, including the cadmium vacancy [26].

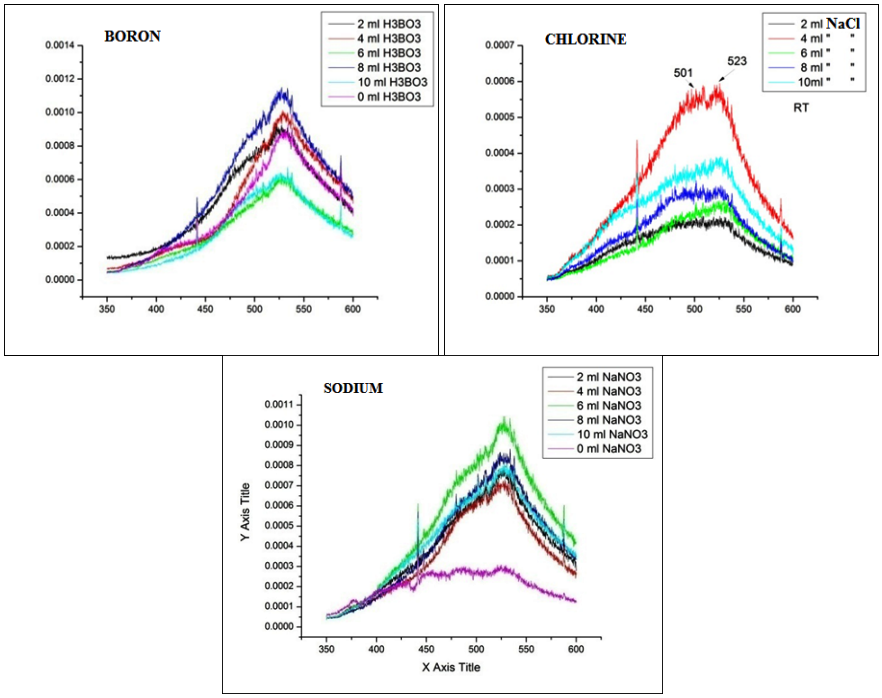

Figure 4.16 PL spectra for CdS thin films doped with boron, chlorine and sodium

4.2.4b RAMAN SPECTROSCOPY

The room temperature Raman spectra of the CdS films doped with boron and sodium are shown in Fig. 4.17. CdS films are transparent to the 633 nm He–Ne line and consequently, the glass substrate contributes to the Raman signal. In fact, the substrate contributes a large band in the 550–600 cm^{-1} spectral region and a Raman feature centered at approximately 450 cm^{-1}. The Raman spectra of the boron doped CdS films (4.17a) present a well-resolved line at approximately 300 cm^{-1}, corresponding to the first order scattering of the longitudinal optical (LO) phonon mode [27]. This peak has been most intense for the concentration of 10ml ($1x10^{-5}$ M). The second-order scattering of LO phonons is also visible at approximately 600 cm^{-1}, although this mode overlaps with the peak of the glass substrate. The Raman spectra of the chlorine doped CdS films (b) does not show the first order LO peak at 300 cm^{-1}. It can be inferred that the sodium impurity drastically affects the CdS structure. Therefore the sodium is rejected.

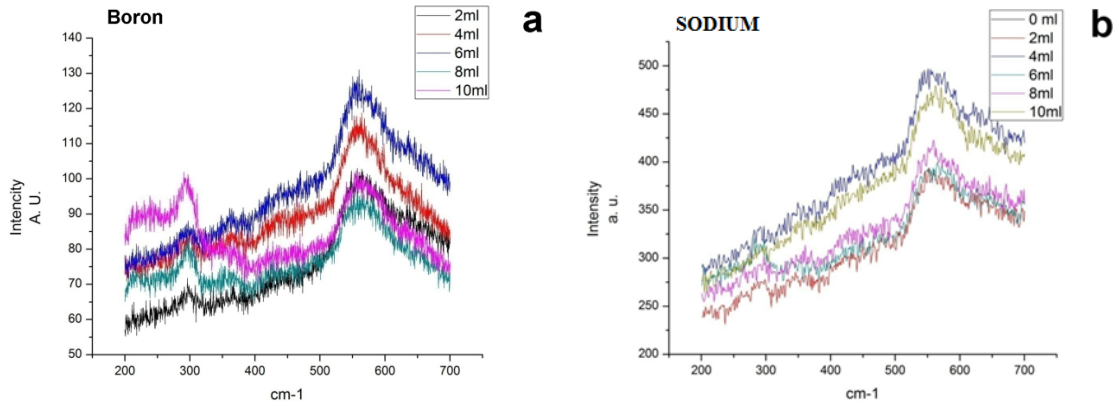

Figure 4.17 Raman spectra of CdS thin films doped with (a) Boron and (b) sodium.

4.2.4c SECOND ION MASS SPECTROSCOPY (SIMS)

A very important fact in doping films is to know how well the element is distributed throughout the film. CdS films doped with boron at different concentration were analyzed by SIMS to observe the homogeneity of films. In figure 4.18, it is shown that the film with concentration of 10 ml has more uniformity due to the B diffused along the thickness. All the films show higher concentrations near the substrate. This increase in concentration at

surface can be caused by the remnants of precursor on the surface at the time of drying [28].

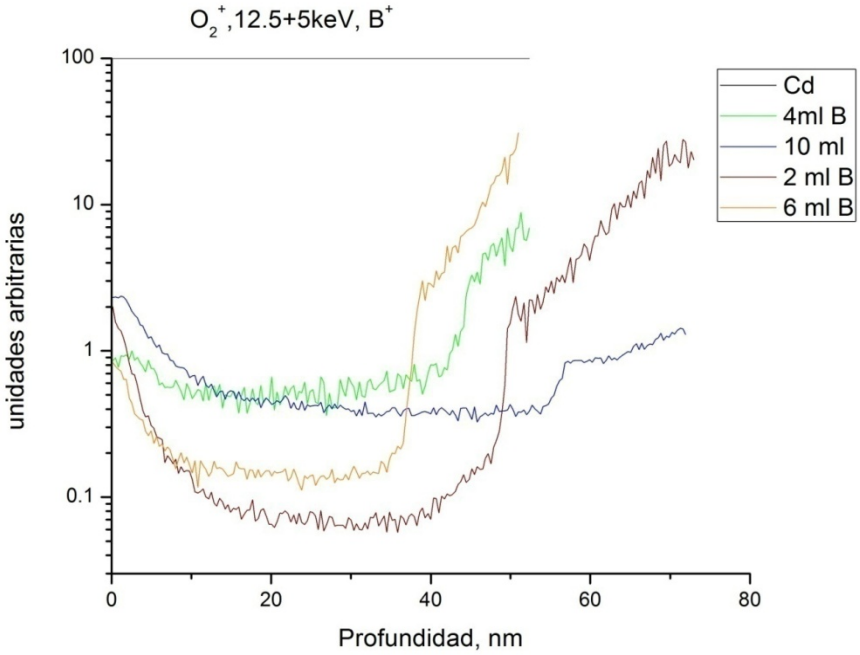

Figure 4.18 Concentration of boron along the thickness.

4.2.4d RESISTIVITY

As it can be seen in figure 4.19, resistivity of boron doped CdS is nearly three orders of magnitude lower than that of undoped films in the region of $1x10^{-5}$ dopant concentration in the bath. At higher dopant concentrations the resistivity of films slightly increases. This is attributed to the precipitation of boron impurity in the inter-grain spaces of CdS films. Similar results have been reported by Altosaar et al [29]. Dependence of electrical resistivity of deposited layers from the chemical nature of bath solution could be an evidence of different level of incorporation of impurities into CdS films.

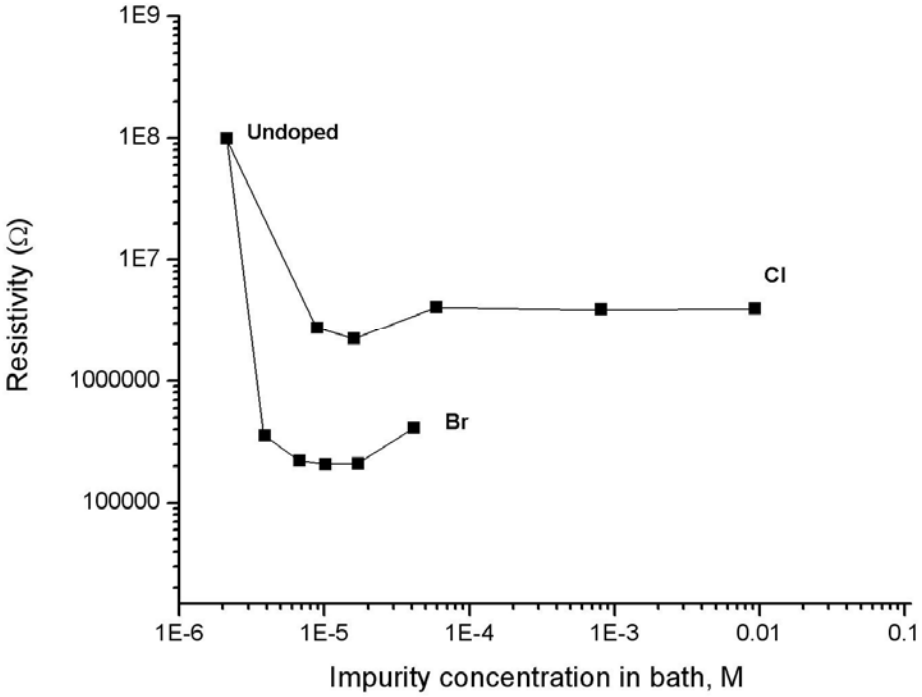

Figure 4.19 Resistivity of boron and chlorine doped CdS films

4.3 CONTACT LAYERS

Photovoltaic cells require proper contact layers for efficient delivery of the energy generated from light. Ohmic contacts play a critical role by allowing current to exhibit a linear relationship with respect to applied voltage.

4.3.1 INDIUM TIN OXIDE (FRONT CONTACT)

Owing to its high optical and thermal stability, indium tin oxide (ITO) layers are frequently used as front contact in thin film solar cells. ITO is an n-type semiconductor with a band gap between 3.5 and 4.3 eV and a maximum charge carrier concentration in the order of 10^{21} cm^{-3} [30]. In hetero-junction cells the very thin emitter layer exhibits a large sheet resistance; therefore ITO contact is necessary to improve the carrier collection in photovoltaic device. In the present work, ITO thin films were deposited on glass substrates using r.f. sputtering at different Power, thickness and substrate temperature. The substrate temperature varied from 50°C to 150°C, power from 40 to 120W and thickness varied from

250-1000 nm. For the ITO films optical transmittance, electrical properties and structural were estimated and presented in the following sections.

4.3.1a TRANSMITANCE

High transparency of ITO thin films in the visible region will have a good impact on their applications in the optoelectronic devices. Owing to this nature, transmittance is considered as one of the essential properties in evaluating the optical performance of ITO films. The transmission spectra of films deposited at various substrate temperatures are shown in Figure 4.20 a). It was found that the transmission increases with increasing heating temperature. It obtained a maximum value (93%) at 100°C, and then decreased. In figure 4.20 b) when the power increases from 40 to 80 W, the transmittance reduces and the absorption edge shifts to the right, on the other hand, from 80 to 120W, the transmittance increases and the absorption edge shifts to the left. Figure 4.20 c) shows that the transmittance reduces as the thickness increases as expected.

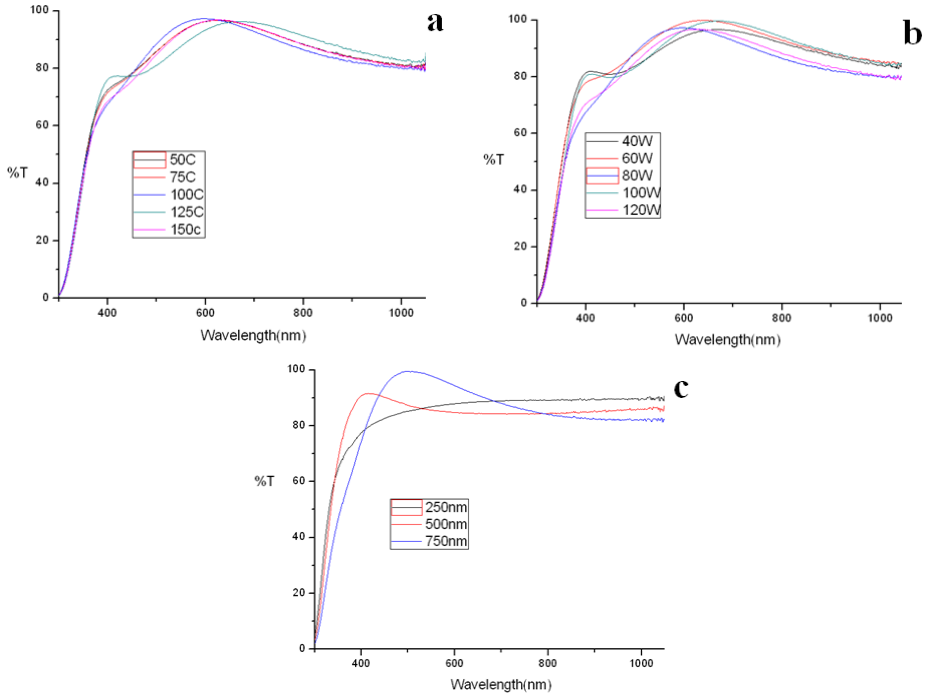

Figure 4.20 Spectral distribution of transmittance of the ITO films deposited at a) different temperature, b) power and c) different thickness.

4.3.1b RESISTIVITY

Resistivity of ITO films associated with the power and thickness are show in figure 4.21 a), as expected the resistivity of films decreases with the increase in thickness as well as power. Figure 4.21 b) shows the resistivity with different substrate temperature and thickness. It is evident that the resistivity decreased continuously with the increase in substrate temperature. Specifically, from 70 to 100°C the sheet resistance showed rapid decrease. This was associated with an increase in the carrier concentration.

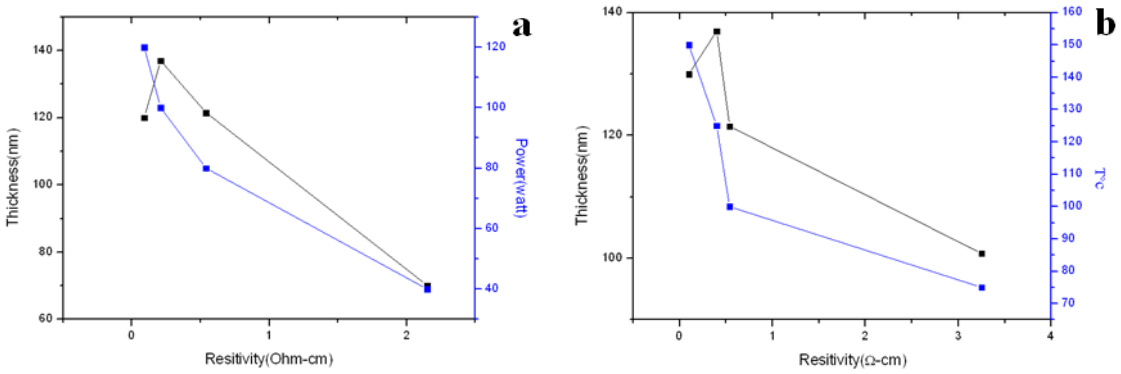

Figure 4.21 Resistivity of ITO films associated with thickness and a) power and b) substrate temperature.

4.3.1c MORPHOLOGY

To examine the possible correlation between the surface morphology and electrical properties of ITO films, the atomic force microscopy (AFM) surface views were acquired. Figure 4.22 shows the 3D AFM image of 100 nm thick ITO film deposited at 80W and with a substrate temperature of 100°C. AFM graph displays the presence of uniform and dense grains.

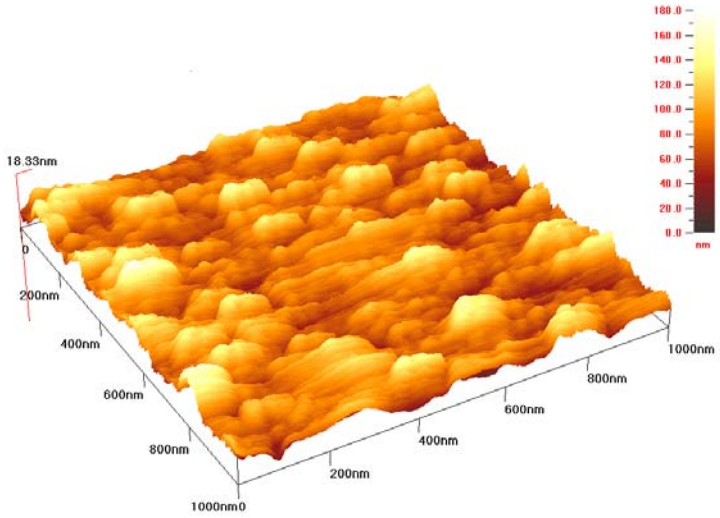

Figure 4.22 Three dimensional AFM images of 100 nm ITO film deposited at 80W and 100°C substrate temperature.

4.3.1d ITO thickness optimization

As the optical and electrical characteristics of ITO depend on the deposition temperature, power and thickness, an optimization of these parameters should be carried out. High-quality front contact must have maximum transmittance and minimum resistance. However as it is shown in figure 4.20 c) and figure 4.21; with the increase in thickness there is a decrease in resistance as well as transmittance. The ITO layer should have high transmittance and low resistance. Based on this aspect among the deposited films the ITO film of 100 nm deposited at 100°C substrate temperature and 80W is determined to possess a high transmittance value and low resistivity of 2.1×10^{-4} Ω cm. This result can be used as a criterion for homogeneity when the deposition of ITO is performed on large areas.

4.3.1e STRUCTURE

The diffractogram of the ITO film deposited at 100°C substrate temperature, power of 80W and 100 nm thickness is show in figure 4.23.

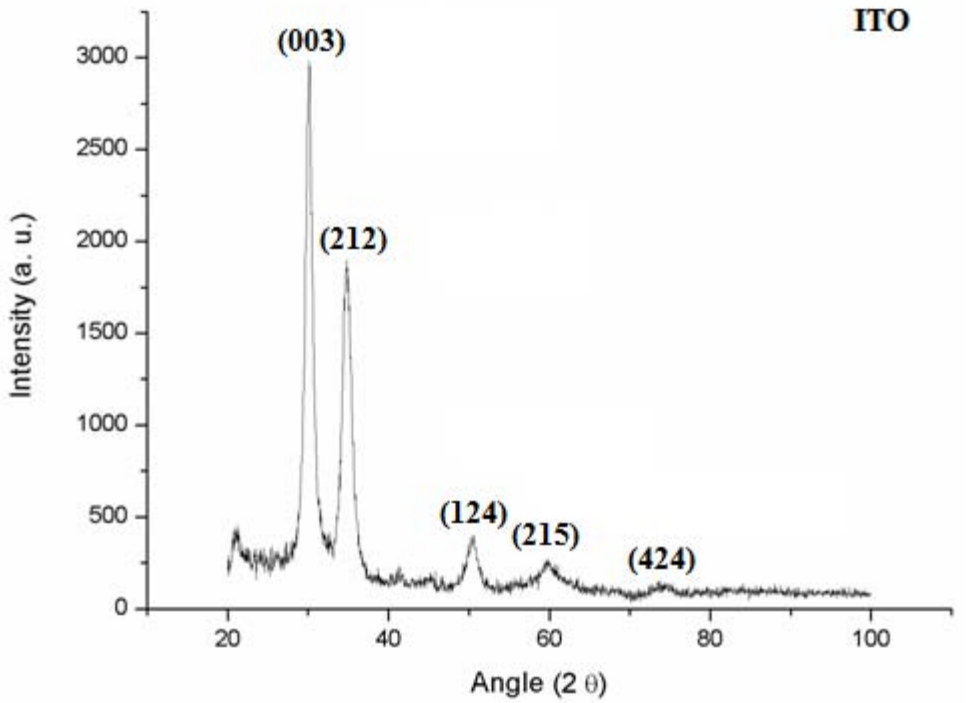

Figure 4.23 XRD diffractogram of the ITO film deposited at 100°C substrate temperature, power of 80W and 100 nm thickness

This film presents five peaks corresponding to (003) plane at 30° 14', (212) plane at 34° 55', (124) plane at 50° 24', (215) plane at 59° 47' and (424) plane at 74° 19' which are the characteristic of rhombohedral structure and are in good agreement with (ICDD) (88-0773). No phases corresponding to other tin compounds were detected showing that the film exhibit $In_4Sn_3O_{12}$ structure with a grain size of 5.51 nm.

4.3.2 MOLYBDENUM (BACK CONTACT)

Due to its outstanding material properties, such as mechanical hardness, high thermal stability and its electronic properties, Molybdenum (Mo) is a refractory metal, well established for protective coatings and high temperature applications [31]. It is used as back contact for advanced solar cell assemblies [32, 33].

Mo thin films are deposited by electron beam evaporation [34, 35] or by sputtering processes [36, 37], but unconventional techniques, such as laser ablation deposition are also reported in the literature [38]. Predominantly, the internal mechanical stress, impurity

concentration, texture, surface roughness and optical reflectance of sputtered thin films and their correlation among each other are investigated under the influence of varying deposition parameters, such as argon pressure, DC power or substrate temperature [39, 40].

The objective of the part of the thesis is to measure the electrical properties as a function of the substrate temperature and thickness. Mo thin films were deposited on glass substrates by DC sputtering varying the power from 20 to 40 W and substrate temperature from room temperature to 500°C.

4.3.2a RESISTIVITY

The resistivity of Mo thin films was determined by four probe method using Loresta GP MCP-T600 equipment. Figure 4.24 shows the resistivity of Mo films of different thicknesses deposited at room temperature.

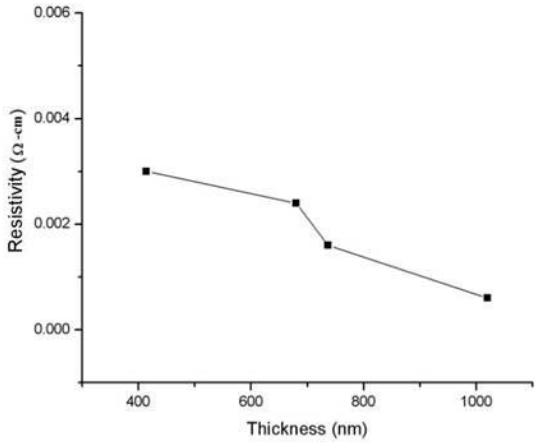

Figure 4.24 Molybdenum thin film resistivity varying thickness.

Decreasing values of resistivity as the thickness increases is expected. Figure 4.23 shows that among the deposited Mo thin films minimum resistance value of $6x10^{-4}$ Ω is found in the film of 1000 nm thickness. Therefore compared to the other films deposited the film of 1000nm is suitable to be used as electrical back contacts in CIS-based devices; this is in agreement with the reported results [34].

In order to study the effect of substrate temperature, the films were deposited at 400 and 500°C substrate temperature.

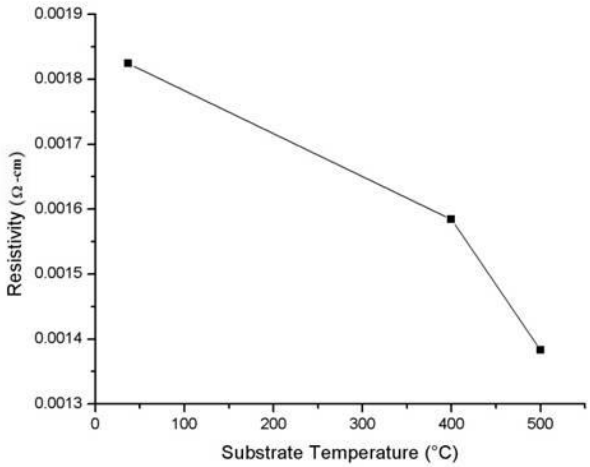

Figure 4.25 1000 nm thickness molybdenum thin film resistivity varying substrate temperature.

Figure 4.25 shows the resistivity values of Mo films deposited at room temperature, 400°C and 500°C. It can be seen that the resistance decreases with the increase in substrate temperature. An explanation of this is that temperature allows grains to grow allowing a better flow of electrons.

4.3.2b MORPHOLOGY

morphological investigations were performed using AFM. Figure 4.26 shows the AFM image corresponding to the 1000nm thickness Mo thin film deposited at 500°C.

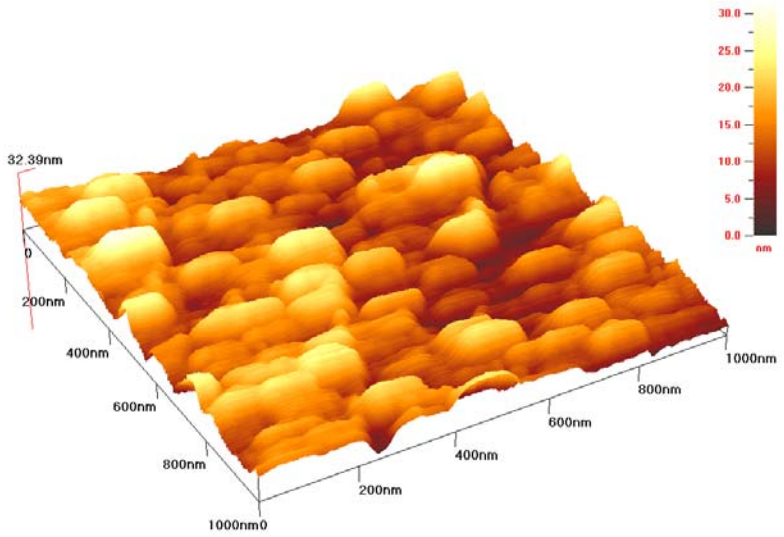

Figure 4.26 Three dimensional AFM images of 1000nm thickness Mo thin film deposited at 500°C.

A visual inspection showed that films presented gross stress and buckling, frequently in zigzag patterns. This behaviour has already been observed by Scofield et al [33].

4.3.2c STRUCTURAL

Fig. 4.27 shows the XRD pattern of the film deposited at a substrate temperature of 500°C and with a thickness of 1000 nm. There are three diffraction peaks corresponding to molybdenum (Mo) cubic phase and five peaks corresponding to molybdenum nitride (Mo_2N) cubic phase . The Mo peaks correspond to (110) plane at 40° 4', (200) plane at 43° 21' and (211) plane at 73° 37'. These peaks were compared to those given in ICDD (#040809). Broadening nature of the XRD peaks indicated that the crystallite sizes of the sample is in nanometer scale. The crystallite size is estimated to be 5.35 nm. The Mo_2N peaks correspond to (112) at 37° 30', (200) at 43° 21', (322) at 63° 17', (312) at 75° 58' and (224) at 80° 11'. These peaks were compared to those given in ICDD (#421120). The presence of Mo_2N could because of using Nitrogen for venting the chamber after deposition of Mo, which would have led to the adsorption of nitrogen on the film surface. No evidences of molybdenum oxides or other molybdenum nitrides is found in this XRD pattern.

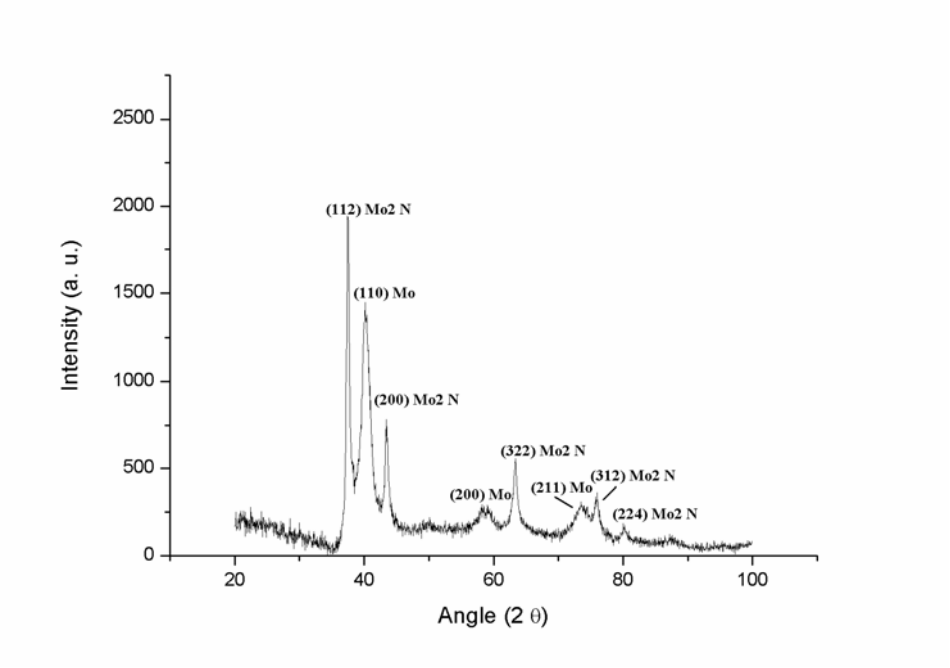

Figure 4.27 XRD diffractogram of the film deposited at a substrate temperature of 500°C and with a thickness of 1000 nm.

4.4 CONCLUSIONS

This chapter presented the results of the preparation and characterization of window and contact layers. The effects of thickness, doping and heat treatment over the properties of CdS window layer have been analyzed. CdS films were deposited by microwave assisted chemical bath. Optimization of deposition parameters for the Mo and ITO contact layers were made. Based on the analysis made in these materials, we can conclude the following:

The CdS films obtained by microwave assisted chemical bath are of good quality, uniformity, adherence and homogeneous. We studied the influence of thickness on structural, optical and electrical properties of CdS film. The films obtained here present hexagonal phase and (100) orientation. The variation of the energy gap with thickness was attributed to deformation of the films and increase in the concentration of carriers. On the other hand, the dependence of the resistivity depending upon the thickness of the films was discussed (mention which section). The resistivity decreases over two orders of magnitude by varying the thickness from 40 nm to 190 nm. The treatment of CdS films annealed at high temperature affects the electrical and optical properties. There is a shift of the

absorption edge toward longer wavelengths during treatment, thus increasing the Band gap, which can be associated with a decrease in the thickness of the CdS and a restructuring of its microstructure. It was found that CdS layers, prepared by CBD using the bath containing different types of donor dopants, have different electrical resistivities. The results confirm that the electrical resistivity of CdS films doped with boron and chlorine was dependent on doping level. Dependence of electrical resistivity of deposited layers on chemical nature of impurities and on their concentration in bath solution could be an evidence of different level of incorporation of impurities into CdS layer.

ITO films were successfully deposited onto quartz glass substrates by r. f. sputter deposition technique. Results showed that the sheet resistance decreased with increased substrate temperature. At the same time, the transmittance reached its maximum (93%) at 100°C, and then slightly decreased when the film was deposited above this temperature. The AFM image showed that the morphology of ITO film present uniform and dense grains. An optimization of the ITO thickness was performed and found to be 100 nm. The optical constants of each film were carefully evaluated. The optimal ITO values were obtained on 100 nm thickness ITO thin film deposited at 100°C substrate temperature and 80W power source. This film presented a resistivity of $2.1=10^{-4}$ Ω cm and a transmittance of 93%.

The influence of substrate temperature and thickness effects on the resistivity of molybdenum thin films was investigated. In order to study the effect of these parameters, Mo thin films were deposited on glass substrates using DC sputtering varying the power from 20 to 40 W and substrate temperature from room temperature to 500°C. These films reduced the resistivity by increasing thickness as well as substrate temperature. The Mo film that presented better electrical properties was the film deposited at a substrate temperature of 500°C and with a thickness of 1000 nm.

REFERENCES

[1] Abdalla A. Alnajjar, Maysoon F.A. Alias, Rasha A. Almatuk, Ala A.J. Al-Douri, Renewable Energy, 34 (2009) 2160-2163.

[2] Armin G. Aberle, Thin films solar cells, Thin solid films 517 (2009) 4706-4710.

[3] D. L. Bätzner, A. Romeo, H. Zogg, R. Wendt, A. N. Tiwari, Thin Solid Films 387 (2001) 151-154.

[4] D.L. Bätzner, R. Wendt, A. Romeo, H. Zogg, A.N. Tiwari, Thin Solid Films 361-362 (2000) 463-467.

[5] M. Rami , E. Benamar, M. Fahoume, F. Charabi, A. Ennaoui, Condens Matter 66 (2000) 3.

[6] J. Fritsche, D. Kraft, A. Thißen, T. Mayer, A. Klein, W. Jaegermann, Thin Solid Films 403–404 (2002) 252-257.

[7] T. Aramoto, F. Adurodija, Y. Nishiyama, T. Arita, A. Hanafusa, K. Omura, A. Morita, Solar Energy Material and Solar Cells 75 (2003) 211-217.

[8] A. I . Oliva, O. Solis Canto, R. Castro Rodriguez and P. Quintana, Thin Solid Films, 391 (2000) 28

[9] R. Castro Rodriguez et al, Applied Surface Science, 161 (2000) 340

[10] P. J. George, A. Sánchez Juarez and P. K. Nair, Seicond Sc. Te chnol., 11 (1996) 1

[11] A. E. Rakhshani and A. S Al-Azab, J Phy. Condens. Matter, 12 (2000) 8745

[12] P. J. Sebastian and Hailin Hu, Advance materials for optic and electronic, 4 (1994) 407

[13] N. Lejmi, O. Savadogo, Solar Energy Material and Solar Cells, 70 (2001) 71

[14] S. A. Al Kuhaimi, Vacuum, 51 (1998) 349

[15] Jae-Hyeong Lee, Thin Solid Films, 515(2007) 6089-6093

[16] P.K. Ghosh, S. Jana, U.N. Maity and K.K. Chattopadhyay, Physica E: Low-dimensional Systems and Nanostructures, 35 (2006) 178-182

[17] Jun Chen, Xinbo Wang and Zhicheng Zhang, Materials Letters, 62 (2008) 787-790

[18] Hsiao-Yen Chung, Chiun-Hsun Chen, and Hsin-Sen Chu, International Journal of Photoenergy 2008 (2008) 6.

[19] Joel Pantoja Enríquez, Xavier Mathew, Solar Energy Materials and Solar Cells 76 (2003) 313-322.

[20] H. Metin, R. Esen, J. crystal Growth 258 (2003) 141-148.

[21] K. L. Chopra, Thin film phenomena, Mc Graw Hill, New York, 1969

[22] T. Tanaka, T. Yamaguchi, T. Ohshima, H. Itoh, A. Wakahara, A. Yoshida, Sol. Energy Mater. Sol. Cells 75 (2003) 109.

[23] S. Kolhe, S. K. Kulkarni, M. G. Takwale, V. G. Bhide, Solar Energy Material, 13 (1986) 203.

[24] J.-H. Lee, J.-S. Yi, K.-J. Yang, J.-H. Park, R.-D. Oh, Thin Solid Films 431/432 (2003) 344.

[25] H. Bidadi, M. Kalafi, H. Tajalli, A. I. Bairamov, T. D. Dzhafarov, Optical Materials 6 (1996) 27-33.

[26] P. K. Nair, MTS Nair, J. Campos and L. E. Sansores, Solar Cells 22 (1987) 221.

[27] Jaehyeong Lee, Thin Solid Films 451-452(2004)170-174.

[28] G. Sasikala, P. Thilakan and C. Subramaniam, Solar Energy Materials and Solar Cells, 62 (2000) 275-293

[29] M. Altosaar, K. Ernits, J. Krustok, T. Varema, J. Raudoja, E. Mellikov, Thin Solid Films 480–481 (2005) 147– 150

[30] Jiaxiang Liu, Da Wu, Shengnan Zeng, materials processing technology 209 (2009) 3943–3948

[31] U. Schmid, H. Seidel, Thin Solid Films 489 (2005) 310 – 319.

[32] C. Guillén, J. Herrero, J. Mater. Process. Technol. 143– 144 (2003) 144.

[33] J.H. Scofield, A. Duda, D. Albin, B.L. Ballard, P.K. Predecki, Thin Solid Films 260 (1995) 26.

[34] K. Uda, Y. Matsushita, S.-I. Takasu, J. Appl. Phys. 51 (1980) 1039.

[35] R.A. Hoffman, J.C. Lin, J.P. Chambers, Thin Solid Films 206 (1991) 230.

[36] M.A. Martínez, C. Guillén, Surface Coating Technology 110 (1998) 62.

[37] Y.G. Shen, Material Science Engineering A 359 (2003) 158.

[38] I.V. Malikov, G.M. Mikhailov, Applied Physics 82 (1997) 5555.

[39] T.J. Vink, M.A.J. Somers, J.L.C. Daames, A.G. Dirks, Applied Physics 70 (1991) 4301.

[40] L.P. Kending, Z.U. Rek, S.M. Yalisove, J.C. Bilello, Surface Coating Technology 132 (2000) 124.

SUMMARY AND CONCLUSIONS

Thin films of $CuInSe_2$ (CIS) were deposited by RF-sputtering of a CIS single ceramic target in argon atmosphere substrate temperature of 400°C. Subsequently copper granules has been evaporated on to the films and followed by thermal annealing to improve the crystallinity and provide adequate stoichiometry. The effects of substrate to target distance, power and thickness were analyzed. The optimum parameters that produce high quality CIS thin films were: substrate to target distance of 6.5 cm, power of 80 W, 2000 nm thickness 13 seconds of copper evaporation at a rate of 35 Å/s and annealing of 500°C for 15 minutes. These conditions produce chalcopyrite films with a preferred orientation to the (112) plane with a grain size of 198 nm. EDAX measurements revealed a near stoichiometric composition of $\Delta m = 0.21$ and $\Delta s = -0.31$ indicating that 82.28% of the films have stoichiometric composition. Optical analysis revealed optical band gap of 1.03 eV. Absorption coefficient α greater than 10^4 cm^{-1} were observed. Conductivity measurements revealed a resistivity in the dark of 2.07 Ω-cm and under illumination of 1.49 Ω-cm which is adequate for high quality photovoltaic devices.

CdS films were deposited by MA-CBD at 70°C without stirring. The films presented good optical properties and polycrystalline structure. The effect of thickness, annealing at different temperatures and doping were studied. X-ray diffraction patterns of these films indicated that they contain both cubic (zincblende) and hexagonal (wurtzite) structures as a mixture. These percentages of hexagonal structured crystallites in the films were seen to increase by annealing. The optical analysis demonstrated that the thickness of 143 nm possessed optical band gap of 2.57 eV. This band gap value allows the entire range of visible light intensity pass to the absorber layer and contributes to energy conversion. Notwithstanding that the optical properties were optimal, CdS is known to be a material highly resistive, in fact from the electrical point of view its behavior is more like an insulator than a semiconductor. Thus, to improve its electrical properties, the effects of annealing and doping were analyzed.

MA-CDB CdS films were annealed at 200, 250, 300, 350 and 400°C different temperatures. An important aspect of the as deposited films that we want to preserve is the existence of nano-particles distributed along the film. From the morphology analysis we found that above 350°C the nano-particles were assimilated into the film. Also it was found that optical energy gap decreases upon increasing the annealing temperature. The film annealed at 250°C showed an improvement in electrical conduction and a just 0.01 eV reduction in the energy gap, therefore it was conclude that the appropriate temperature to improve the electrical properties without affecting the optical properties was 250°C.

The CdS films were doped with boron, chlorine and sodium by 5 different concentrations. Photoluminescence showed that chlorine highly influences the behavior of band edge. Since we did not want to modify the optical properties, this element was discarded. From the Raman spectra it was inferred that the sodium impurity drastically affected the CdS structure, consequently the element that best suit the doping of CdS was boron. CdS films doped with boron at different concentration were analyzed by SIMS in order to know which concentration was the most appropriate for doping. It was shown that the film with concentration of 10 ml had more uniformity along the thickness and the electrical analysis proved that the boron doped was three orders of magnitude lower the undoped film.

ITO used as top contact was deposited by r.f. sputtering. The optimizations of substrate temperature, power and thickness were realized. ITO films with adequate optical transmittance of 93% and electrical resistivity of 2.1×10^{-4} Ω cm were assured by substrate temperature of 100°C, 80 W and 100 nm thickness.

Mo thin films were deposited by c.d. sputtering in order to achieve high conductive films to use as back contact layer. Substrate temperature and thickness were optimized. Films deposited at 500°C and thickness of 2000 nm presented suitable resistivity less than 1.4×10^{-3} Ω-cm.

FUTURE WORK

Notwithstanding the progress made in optimizing the parameters in preparation and improvement of optical and electrical properties of thin film materials for photovoltaic systems, it should continue further work in this direction for obtaining more efficient devices. Among the future directions for work necessary to obtain more efficient devices are:

- Formation and characterization of the interface Mo / CIS / CdS / ITO
- Investigate the influence in conductivity and structural properties of Mo_2N and oxygen in the interface Mo/CIS
- Optimization of thin films that make up the p-n junction with varying the composition
- Further optimizing of the electrical properties of ITO